Pattern formation, photonic spin-orbit coupling and topological states in semiconductor microcavities and micropillar lattices

Charles Ernest Whittaker

Department of Physics & Astronomy

University of Sheffield

Submitted for the degree of

Doctor of Philosophy

July 2018

To my grandfather, *Ernest Washington.* (1926–2014)

Acknowledgements

It has been a great privilege to work in the Low Dimensional Structures and Devices (LDSD) group in the Department of Physics and Astronomy at the University of Sheffield. I am highly grateful to my supervisors Dimitrii Krizhanovskii and Maurice Skolnick for their continued supervision and direction throughout my PhD studies, as well as for giving me the opportunity to embark on a PhD in their group in the first place. I would like to thank both the present members of the group who have offered me so much support and guidance with research as well as the past members whose hard work laid the foundations for all projects in which I have been involved. In particular, I am grateful to Paul Walker, who not only provided immeasurable help with lab work and data analysis, but extensive knowledge and keen insights which have contributed substantially to all my research. I would also like to thank Max Sich and Branislav Dzurnak, both of whom I have also had the pleasure to work with on edifying and fruitful projects; Emiliano Cancellieri, whose constructive input and enduring patience have taught me lots; and all the people whose hard work behind the scenes made this thesis possible: Ed Clarke, Ben Royall and Deivis Vaitiekus for growth and fabrication of samples and Chris Vickers and Phil Taylor for supplying the lab with helium. Finally, I would like to thank my family and friends for their continued support.

Abstract

Microcavity polaritons are mixed light-matter quasiparticles arising from the hybridization between confined cavity photons and quantum well excitons. Since their first observation over a quarter of a century ago, they have been extensively researched for the unusual and attractive properties imparted by the combination of light and matter components, including their unique dispersion relation, small effective mass and strong repulsive interactions, leading to rich phenomena in both linear and nonlinear regimes. More recently, advanced post-growth fabrication techniques have allowed for sophisticated tailoring of the potential landscape of polaritons, opening up a new avenue of research into polaritonic lattices which show great promise towards quantum simulation and photonic topological states. In this thesis both planar and laterally-patterned microcavities are studied, addressing fundamental concepts in polariton physics.

In Chapter 3 planar microcavities are studied under conventional plane wave excitation, and the spontaneous generation of vorticity and super-Poissonian photon statistics are demonstrated.

In Chapter 4, single, coupled and zigzag chains of etched micropillars are studied under low-power incoherent excitation and the polarization degree of freedom is investigated. In the latter case, different localization lengths are found for orthogonally-polarized topological edge states of the system.

In Chapter 5, two-dimensional Lieb lattices of micropillars are studied in low-power and high-power non-resonant and quasi-resonant regimes, where multi-mode condensation, nonlinear fragmentation and pseudospin (polarization) textures are reported.

Table of contents

List of figures

List of publications

Journal publications

Polariton Pattern Formation and Photon Statistics of the Associated Emission

C. E. Whittaker, B. Dzurnak, O. A. Egorov, G. Buonaiuto, P. M. Walker, E. Cancellieri, D. M. Whittaker, E. Clarke, S. S. Gavrilov, M. S. Skolnick and D. N. Krizhanovskii

Phys. Rev. X **7**, 031033 (2017)

DOI: https://doi.org/10.1103/PhysRevX.7.031033

Exciton Polaritons in a Two-Dimensional Lieb Lattice with Spin-Orbit Coupling

C. E. Whittaker, E. Cancellieri, P. M. Walker, D. R. Gulevich, H. Schomerus, D. Vaitiekus, B. Royall, D. M. Whittaker, E. Clarke, I.V. Iorsh, I. A. Shelykh, M. S. Skolnick, and D. N. Krizhanovskii

Phys. Rev. Lett. **120**, 097401 (2018)

DOI: https://doi.org/10.1103/PhysRevLett.120.097401

Spatiotemporal Continuum Generation in Polariton Waveguides

P. M. Walker, C. E. Whittaker, D. V. Skryabin, E. Cancellieri, B. Royall, M. Sich, I. Farrer, D. A. Ritchie, M. S. Skolnick, D. N. Krizhanovskii

In preparation (2018)

Polarization effects in topological zigzag chains for photons

C. E. Whittaker, E. Cancellieri, P. M. Walker, B. Royall, L. E. Tapia Rodriguez, E. Clarke, H. Schomerus, M. S. Skolnick, and D. N. Krizhanovskii

In preparation (2018)

Conference presentations

Exciton-polaritons in a two-dimensional Lieb lattice with spin-orbit coupling

C. E. Whittaker, E. Cancellieri, P. M. Walker, D. R. Gulevich, H. Schomerus, D. Vaitiekus, B. Royall, D. M. Whittaker, E. Clarke, I. V. Iorsh, I. A. Shelykh, M. S. Skolnick, and D. N. Krizhanovskii

Upgraded contributed oral presentation at EP2DS-22/MSS-18 2017, Pennsylvania, USA

Contributed oral presentation at OECS 2017, Bath, UK

Contributed oral presentation at UK Semiconductors 2017, Sheffield, UK

Poster presentation at QFLM 2017, Cargèse, Corsica

Transverse spatial pattern formation in a semiconductor microcavity

C. E. Whittaker, B. Dzurnak, P. M. Walker, E. Cancellieri, D. N. Krizhanovskii, O. A. Egorov and M. S. Skolnick

Contributed oral presentation at UK Semiconductors 2016, Sheffield, UK

Poster presentation at ICSCE8 2016, Edinburgh, Scotland

Poster presentation at ICPS 2016, Beijing, China (presented by P. M. Walker)

Optical Spin Hall Effect and Pattern Formation in Semiconductor Microcavities

C. E. Whittaker, B. Dzurnak, P. M. Walker, D. N. Krizhanovskii and M. S. Skolnick

Poster presentation at ISNP 2015, Cefalù, Sicily

Chapter 1

Background

1.1 Introduction

The astounding potential of microcavity polaritons has been revealed by over a quarter of a century's worth of creative and fruitful experimentation. These quasi-particles, representing a superposition of both light and matter, have so far provided access to an incredible wealth of rich physics such as Bose-Einstein condensation, superfluidity, quantized vortices and ultra-efficient parametric scattering, to name but a few associated phenomena. And yet, despite the maturity of the polariton field, the keen interest surrounding polariton systems refuses to subside, and it instead appears that the extensive research and development applied to polariton systems leading up until this point is now heralding a new era. At the heart is a desire to understand the intimate interaction between light and matter, which has fascinated scientists going back to antiquity, and the tantalizing prospect of the new applied and fundamental physics which might develop as a consequence. The initial interest in polariton systems as integrated sources of ultra-low-threshold coherent light emission endures, whilst year after year new capabilities and avenues of research continue to open up, enabled by both academic ingenuity and technological prowess. Indeed, polaritons look set to continue revealing new secrets and inspiring physicists for years to come, and a new generation of high-quality samples promises to finally deliver the crucial application.

1.2 Microcavity polaritons

1.2.1 Semiconductor materials

The samples used throughout this thesis are all microcavities based around the III-V compound semiconductor GaAs and ternary alloys InGaAs and AlGaAs. GaAs is a zinc-blende material, which refers to crystals comprising two types of atoms arranged in interpenetrating face-centered cubic lattices, and features a direct band gap, unlike silicon, which makes it favourable for optoelectronic research. The extensive research into GaAs-based heterostructures and mature epitaxial growth is one reason why GaAs is the most popular choice of material for polariton research, along with the II-VI binary compound CdTe. However, there is also a growing body of research into other materials, such as wide band gap semiconductors (e.g. GaN and ZnO) and more recently organic polymers [1]. Ease of growth, sample quality, temperature of operation and optoelectronic properties are all important criteria which determine the relative advantages and disadvantages of different semiconductor materials [2].

1.2.2 Excitons

In direct band gap semiconductors, the promotion of an electron from the valence band to the conduction band occurs upon absorption of a photon with energy greater than the band gap E_G, leaving a vacancy referred to as a hole. The electrostatic Coulomb interaction between the negatively charged electron and positively charged hole favours the formation of a bound state known as an exciton, whose energy is less than that of an unbound electron-hole pair by its binding energy E_B. The two types of excitons, known as Wannier-Mott and Frenkel excitons refer to the cases when the size of the exciton is greater than or less than the lattice spacing respectively. In the former case, which applies to the GaAs excitons studied here, the hydrogenic wavefunction can be found by solving the Schrödinger equation

$$\left[-\frac{\hbar^2}{2\mu}\nabla^2 - \frac{e^2}{4\pi\varepsilon\varepsilon_0 r}\right]\psi(r) = E\psi(r), \tag{1.1}$$

where $\mu = m_e m_h/(m_e + m_h)$ is the reduced mass of the bound electron (with mass m_e) and hole (with mass m_h) and r is their separation. This leads to a $1s$ exciton wavefunction given by

$$\psi_{1s}(r) = \frac{1}{\sqrt{\pi a_B^3}} e^{-r/a_B} \tag{1.2}$$

where $a_B = 4\pi\hbar^2\varepsilon\varepsilon_0/\mu e^2$ is the Bohr radius. The binding energy is then

$$E_B = \frac{\hbar^2}{2\mu a_B^2}. \tag{1.3}$$

In GaAs, the large dielectric constant ε [3] means the Coulomb force between carriers is highly screened, leading to a large Bohr radius exceeding 10 nm and corresponding small binding energy of a few meV. Since the characteristic thermal energy k_BT of the system at room temperature is 25 meV, which exceeds E_B, GaAs excitons are only stable at cryogenic temperatures. In contrast, in materials such as GaN and ZnO ε is smaller meaning E_B exceeds 25 meV and excitons do not dissociate at room temperature.

Optical excitation is the simplest method to create and study excitons, and it has long been understood that coupling an excitonic resonance to light modifies the physical properties of the excitons. Early theoretical works by Pekar [4] and Hopfield [5] studied the modified exciton dispersion in bulk semiconductors. Low-dimensional confinement of excitons allows enhanced coupling to light since the density of states is strongly altered which affects the exciton oscillator strength f [6, 7]. Indeed, layering a semiconductor between two semiconductors with a larger band gap creates a potential well in which carriers are confined, with the outer layers acting as barriers. When the thickness of the well is reduced to a length scale comparable to the de Broglie wavelength of carriers ($\sim$15 nm or less in GaAs) there is quantum confinement of the excitons in the effectively 2D plane of the material layer, termed a quantum well (QW). The binding energy of excitons is enhanced in QWs compared to the unconfined case (correspondingly the Bohr radius decreases). From the expression for the integrated absorption intensity of QWs per unit length,

$$A = \frac{4\pi^2 e^2 \hbar f}{n m_0 c L}, \tag{1.4}$$

where n is the material refractive index and L the QW width, one can see how confinement increases optical absorption, as verified by detailed measurements [8]. For maximum light-matter coupling, one needs also to confine photons, since the dimensionality mismatch between unconfined photons and 2D excitons means the excitons couple to a continuum of photon modes (only in-plane momentum conservation is required). Thus, irreversible radiative decay of the exciton occurs, and the system exists in the so-called weak coupling regime [9]. In contrast, when the coupling rate between excitons and photons exceeds the damping, the regime of strong coupling is reached, and new mixed light-matter eigenmodes appear: *polaritons*.

1.2.3 Microcavities

Dating back to the first demonstrations of the semiconductor laser diode in 1962 [10, 11], decades of extensive research and technological advances in fabrication have led to wide use of both optical microresonators and QWs in light-emitting devices [12]. An example of such a device is the vertical-cavity surface-emitting laser (VCSEL) developed throughout the 1980s and widely used for technological applications. The highly reflective planar mirrors in VCSELs strongly modify the spontaneous emission rate of the excited electron-hole pairs in the QW layer and concentrate the emission into a tight cone. It was these advances which allowed the first demonstration of strong exciton-photon coupling (in 2D) to form microcavity polaritons by Weisbuch and co-workers in 1992 [13].

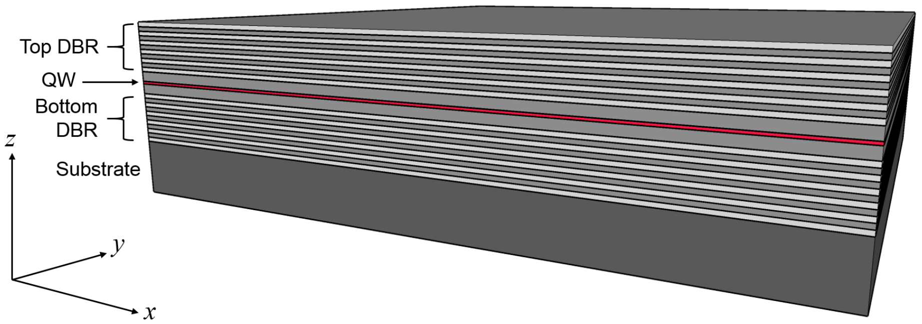

Fig. 1.1 Schematic of a typical semiconductor microcavity.

The highly-reflective mirrors used in microcavities consist of epitaxially grown stacks of alternating layers of two semiconductors with different refractive indices, known as distributed Bragg reflectors (DBRs). The thickness of individual layers ensures optimal reflection via constructive interference of reflected light, mediated by the Bragg condition $d = \lambda/4n$. Increasing the number of DBR layers allows reflectivities approaching unity to be attained within a spectral window (known as the stop-band) around a central wavelength $\bar{\lambda}$. Using this knowledge high quality microresonators can be engineered by placing a defect layer (which serves as the optical cavity) between two DBRs, all of which can be grown with atomic precision onto a suitable substrate using molecular beam epitaxy (MBE). Modern semiconductor microcavities used for polariton research typically feature 20–30 DBR pairs in the top and bottom stacks, although state-of-the-art cavities can have up to 40 pairs in a single stack [14]. The samples used in this thesis feature the commonly used choice of GaAs/AlGaAs DBRs, enclosing a GaAs cavity with InGaAs QWs, on a GaAs substrate [15].

The dispersion of microcavity photons in a cavity of length L_C and refractive index n_C can be expressed as

$$E_C(k_{\|}) \approx E_C(k_{\|} = 0) + \frac{\hbar^2 k_{\|}^2}{2m_C} \tag{1.5}$$

where the in-plane wave vector is given by $k_{\|} = \sqrt{k_x^2 + k_y^2}$ and $m_C = hn_C/cL_C$ is the cavity photon effective mass ($\sim 10^{-5}m_0$). The cavity loss rate γ_C gives the cavity resonance a finite width in energy, which is inversely proportional to and limited by the cavity lifetime (homogeneously broadened). It can be used to define the quality or Q factor of the cavity, $Q = E_C/\gamma_C$.

Placing a QW at one of the antinodes of a microcavity introduces an excitonic resonance E_X into the system, whose dispersion is essentially flat due to its large effective mass $m_X \sim 10^{4-5}m_C$. If the exciton oscillator strength and cavity Q factor are sufficiently large, normal mode splitting between the QW exciton and cavity photon occurs when their energies are close to resonance. Energy is transferred back and forth at the so-called Rabi frequency Ω and an upper polariton (UP) and lower polariton (LP) branch are formed. Their energies are given by

$$E_{\mathrm{UP,LP}}(k_{\|}) = \frac{1}{2}\Big[E_X + E_C - i(\gamma_X + \gamma_C)\Big] \pm \frac{1}{2}\sqrt{(\hbar\Omega)^2 + \Big[E_C - E_X - i(\gamma_C - \gamma_X)\Big]^2} \tag{1.6}$$

where γ_X is the exciton linewidth, which is determined largely by thickness fluctuations and alloy disorder, i.e. it is broadened inhomogeneously. $\hbar\Omega$ defines the vacuum

Rabi splitting in analogy with atomic physics, and has typical values of 4–15 meV in contemporary GaAs-based microcavities [7]. Physically it represents a dipole interaction strength which is proportional to

$$\Omega \propto \sqrt{\frac{f N_{\mathrm{QW}}}{L_C}} \tag{1.7}$$

where N_{QW} represents the number of QWs in the cavity [16]. In order for strong coupling to exist, the condition that $\hbar\Omega > \gamma_X, \gamma_C$ must be met. The signature of this regime is the avoided crossing of UP and LP branches, whose splitting is $\hbar\Omega$ when the cavity-exciton detuning $\Delta = E_C - E_X$ is zero.

As represented using colours in Fig. 1.2, the polariton branches have a mixed light-matter content which varies smoothly with Δ. The so-called Hopfield coefficients [5] give the respective exciton and photon fractions of LP and UP states as

$$|X(k_{\parallel})|^2 = \frac{1}{2}\left[1 + \frac{\Delta(k_{\parallel})}{\sqrt{\Delta(k_{\parallel})^2 + (\hbar\Omega)^2}}\right] \tag{1.8}$$

and

$$|C(k_{\parallel})|^2 = \frac{1}{2}\left[1 - \frac{\Delta(k_{\parallel})}{\sqrt{\Delta(k_{\parallel})^2 + (\hbar\Omega)^2}}\right], \tag{1.9}$$

which satisfy $|X(k_{\parallel})|^2+|C(k_{\parallel})|^2 = 1$. Since the polariton states are linear superpositions of exciton and photon states, their lifetimes are given by the weighted exciton and photon lifetimes $\gamma_{\mathrm{UP}} = |C|^2\gamma_X + |X|^2\gamma_C$ and $\gamma_{\mathrm{LP}} = |X|^2\gamma_X + |C|^2\gamma_C$. It should be noted that the inhomogeneously broadened exciton peak is typically highly asymmetric,

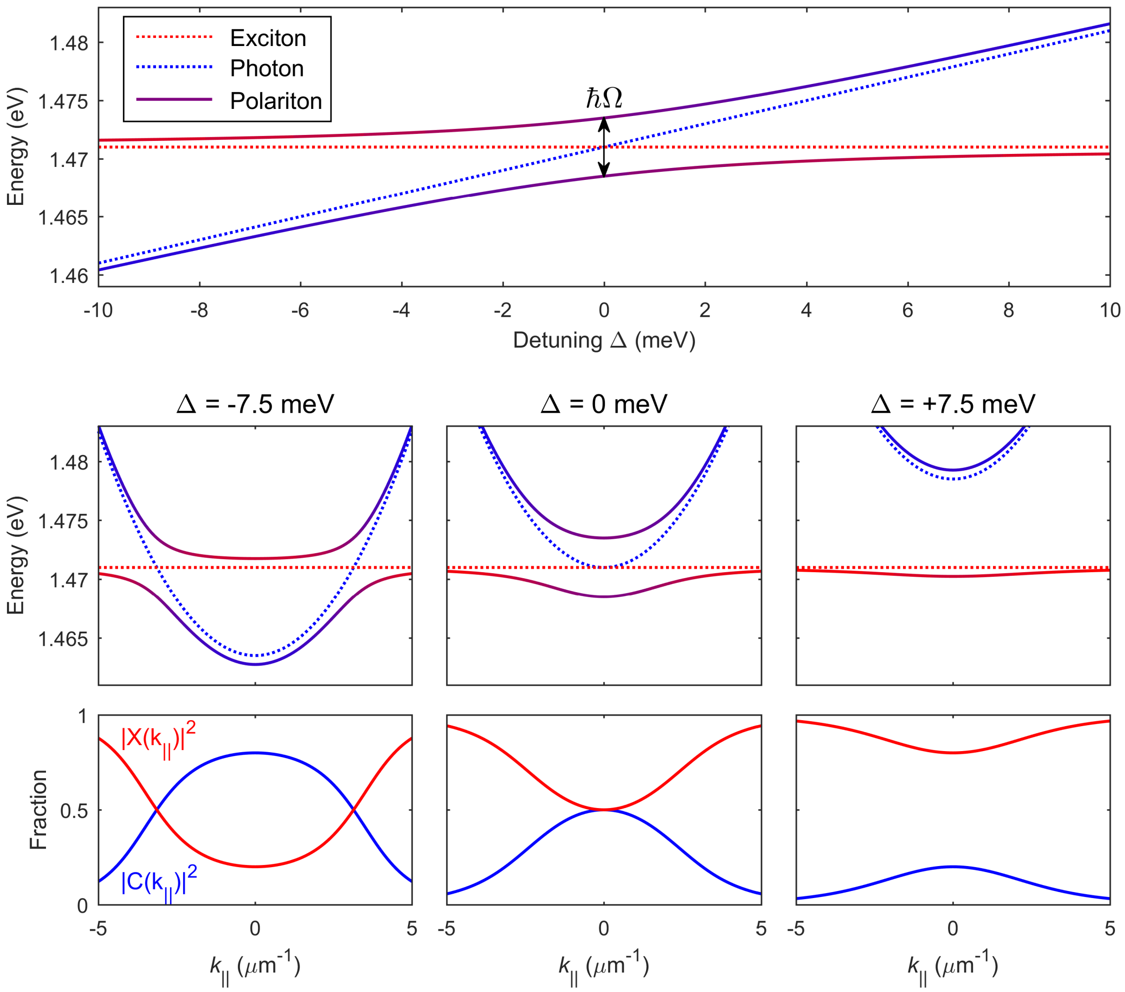

Fig. 1.2 Anti-crossing of upper and lower polariton branches as E_C is tuned across E_X. The middle panel shows the polariton dispersion at negative (left), zero (centre) and positive (right) cavity-exciton detuning. The bottom panel shows the corresponding Hopfield coefficients.

such that at resonance ($|X|^2 = |C|^2 = 0.5$) the LP resonance is typically much narrower than that of the UP [17]. The polariton effective masses are given by $1/m_{\mathrm{UP}} = |C|^2/m_X + |X|^2/m_C$ and $1/m_{\mathrm{LP}} = |X|^2/m_X + |C|^2/m_C$. One can see from Fig. 1.2 that the polariton dispersion is approximately parabolic at small k, and as such can be described by the quadratic relation

$$E_{\mathrm{UP,LP}}(k_{\parallel}) \approx E_{\mathrm{UP,LP}}(k_{\parallel}=0) + \frac{\hbar^2 k_{\parallel}^2}{2m_{\mathrm{UP,LP}}}. \tag{1.10}$$

This is simply an approximation however. It has been suggested recently that this part of the dispersion may actually be better described by a non-parabolic model with *fractional* kinetic energy [18].

1.3 Collective coherence phenomena

1.3.1 Relaxation processes

Typically, microcavity polaritons are excited by non-resonant optical excitation, where the laser is blue-detuned several hundreds of meV from the LP branch. Free electron-hole pairs are generated by laser excitation, rapidly thermalizing on picosecond time scales. It is thought that high-k bound exciton states are then populated by the emission of longitudinal optical (LO) phonons, which interact strongly with carriers to carry off large amounts of energy rapidly [19, 7]. These initial steps of relaxation via phonon scattering wash out any coherence of the electron-hole pairs. Excitons continue to relax down the dispersion through further scattering with acoustic phonons, eventually reaching the optically active zone after 100-200 ps where they can couple to photons to form polaritons. Outside of this region of momentum space, excitons have a wave vector larger than light in vacuum and hence do not recombine radiatively. The cone is defined by $\sqrt{k_x^2 + k_y^2} = \omega/c$. Inside the optically active region, polariton relaxation reaches a so-called bottleneck in the vicinity of the inflection point, where polaritons tend to accumulate. This behaviour arises due to the steepness of the dispersion beyond this point, where fewer phonons are available to carry away large amounts of energy with a small reduction in k. In thin GaAs QWs, where the width $L \sim a_B$ (the exciton Bohr radius), the exchanged momentum is limited to $a_B^{-1} = (100\text{Å})^{-1}$ which gives an energy of around 1 meV [20]. Simultaneously, the polariton states inside the radiative region also have an increased photon content which reduces their lifetime, which can limit further cooling depending on how the polariton lifetime compares to the acoustic phonon scattering time (∼10 ps). This effect, first studied in detail in Ref. [20], can lead to a strongly non-equilibrium polariton distribution function which peaks at finite k, and is more pronounced in negatively-detuned cavities.

In the bottleneck region, polariton-polariton scattering offers another mechanism through which LPs can relax provided the density is sufficiently high. It is an elastic dipole-dipole interaction which can exchange a few meV on a time scale of a few ps, providing the main mechanism to populate the parabolic part of the LP dispersion [7]. The optical pumping also creates free carriers, which induce efficient polariton-free-carrier interactions on sub-picosecond time scales, where the steeper electron dispersion allows a larger energy exchange than that provided by acoustic phonons.

1.3.2 Polariton condensation

As composite bosons, polaritons are expected to undergo a phase transition of the type seen in Bose-Einstein condensates (BECs) at sufficiently high densities, triggering

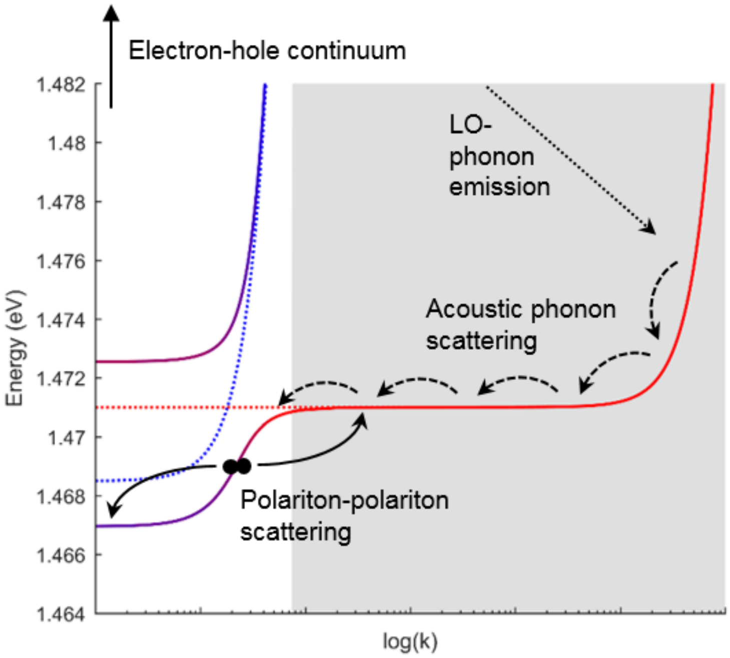

Fig. 1.3 Schematic of relaxation processes in a microcavity under non-resonant excitation, showing the initial LO-phonon emission (dotted arrow), scattering with acoustic phonons (dashed arrows) and polariton-polariton scattering (solid arrows). The grey area corresponds to the optically inactive states outside of the light cone.

macroscopic occupancy of the ground state. As discussed in the last section, polaritons have a distribution function governed by the balance between pumping, which continuously replenishes a reservoir of high-energy excitons, relaxation processes which transfer particles towards lower energy states and push the distribution function closer to an equilibrium one, and the finite lifetime through which particles are lost. Microcavities are therefore driven-dissipative systems with an intrinsically non-equilibrium dynamics, and depending on how close the system is to equilibrium one can classify two different regimes:

Thermodynamic condensation.– When the polariton lifetime is long enough to allow particles to reach a quasi-thermal distribution function, the system can be approximately described in terms of an equilibrium BEC function $N_{\mathrm{BE}}(E) = 1/(e^{(E-\mu)/k_BT} - 1)$ where μ and T are the chemical potential and temperature of the system respectively.

Kinetic condensation.– When the polariton lifetime is insufficiently long to allow thermalization, rather than accumulating in the state that minimizes the system energy polaritons accumulate in the state with the optimal balance between scattering processes and lifetime.

In both cases the resulting microcavity emission consists of a coherent beam of light which has led to popular use of the term "polariton laser" dating back to early polariton works [21]. However, in contrast to conventional lasers, in polariton systems no population inversion is required for the emission of coherent light, and optical gain can be achieved whenever the net scattering rate towards a mode compensates the radiative losses. This implies the potential for ultra-low-threshold coherent light emission, an aspect of polariton systems which has attracted keen interest over the years [22]. When increasing the excitation of the sample more electrons and holes are injected into the valence and conduction bands, which fill up offering fewer and fewer states to form excitons. This phenomenon is known as phase space filling [23, 24] and decreases the exciton oscillator strength and thus the Rabi splitting [25]. Gradually the coupling strength between the exciton and photons diminishes at high pumping powers. Finally, when the conduction and valence bands are completely filled, no excitons can exist in the system anymore, and further polariton formation is prohibited. This transition takes place at the so-called Mott density, occurring in GaAs- based QWs for injected densities of electron hole pairs around 10^{11} cm^{-2} [26]. Beyond the

Mott transition strong coupling is no longer possible, and conventional photon lasing takes place due to the carrier population inversion in the QW(s).

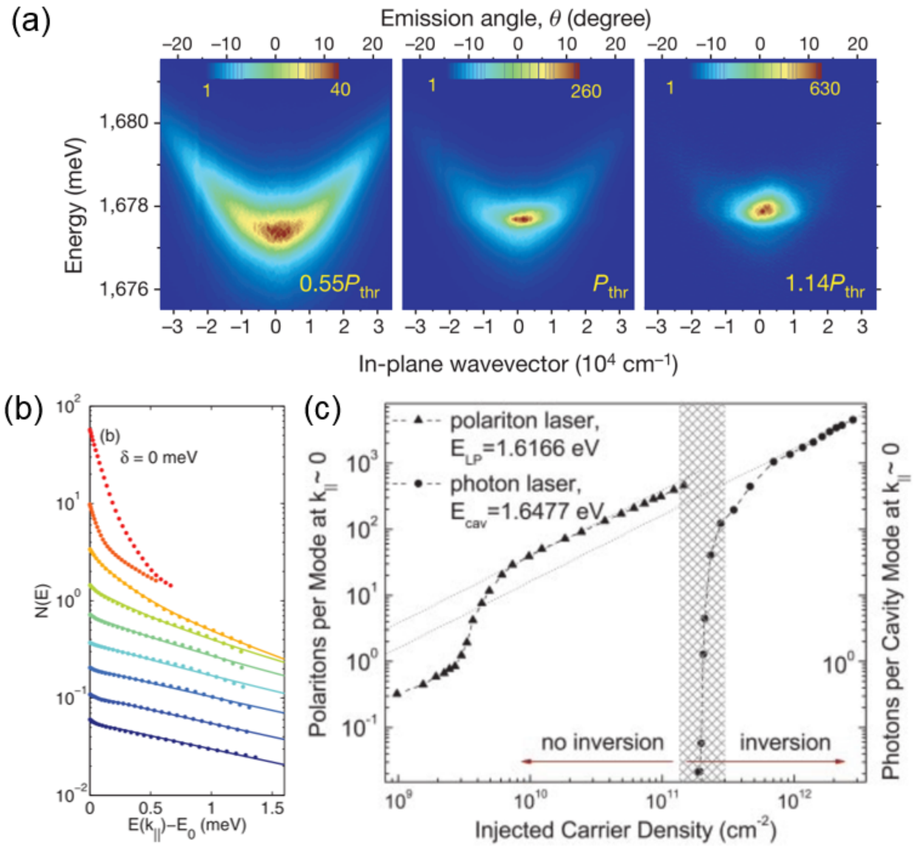

Fig. 1.4 (a) Experimental dispersion relations across the polariton condensation threshold from Ref. [27]. Below threshold polaritons have a broad distribution in momentum and energy. At and above threshold polaritons macroscopically occupy the $k = 0$ (ground) state. (b) Energy distributions of an optically trapped thermalized BEC in a high Q microcavity from Ref. [14] showing fits to the equilibrium Bose-Einstein distribution. The power values from low to high are 0.12, 0.24, 0.45, 0.71, 0.93, 1.07, 1.10, 1.12, and 1.14 times the threshold value, which is 443 mW. (c) Number of LPs and cavity photons per mode against injected carrier density for a polariton laser (triangles) and photon laser (circles) taken from Ref. [28].

The wave function $\Psi(r, t)$ of a macroscopically occupied polariton state can be described by

$$\Psi(r,t) = \sqrt{n(r,t)}e^{i\theta(r,t)} \tag{1.11}$$

where $\Psi(r,t)$ has non-zero mean value and acts as the order parameter for the phase transition. It is a complex number with an amplitude ($|\Psi|^2$ gives the condensate density) and a phase. The system Hamiltonian initially has global gauge invariance, meaning it is invariant under an arbitrary phase change of $\Psi(r,t)$. However, at the phase transition there is a spontaneous symmetry breaking as the whole condensate assumes a specific phase [7]. In order to describe the dynamics of a polariton system with long-range phase coherence, pumping and decay, the standard treatmeant is the generalized Gross-Pitaevskii equation (GPE), sometimes called the Ginzburg-Landau equation. Generally the LP branch is described by a parabolic dispersion, and the condensate can be pumped either resonantly or nonresonantly through the presence of an exciton reservoir (representing the bottleneck effect). The UP states are ignored since they play little role and are not highly populated. In the case of non-resonant pumping the widely-used complex GPE describing the macroscopic wave function Ψ of the condensate with gain and loss is

$$i\hbar\frac{\partial\Psi(r,t)}{\partial t} = \left\{-\frac{\hbar^2\nabla^2}{2m_{\mathrm{LP}}}+V_{\mathrm{ext}}(r,t)+\frac{i}{2}\Big[R(n_R(r,t))-\gamma\Big]+g|\Psi(r,t)|^2+g_R n_R(r,t)\right\}\Psi(r,t), \tag{1.12}$$

where $V_{\mathrm{ext}}(r,t)$ accounts for any external potentials created by e.g. photonic disorder or post-growth patterning of the microcavity, g and g_R give the strength of polariton self-interactions and interactions with reservoir excitons, respectively. There are also terms to represent dissipation of polaritons at a rate γ and creation of polaritons at a rate $R(n_R)$ via scattering from the exciton reservoir. The reservoir density n_R, is described by the equation

$$\frac{\partial n_R(r,t)}{\partial t} = P_R(r,t) - \gamma_R n_R(r,t) - R(n_R)|\Psi(r,t)|^2, \tag{1.13}$$

where P_R is the pumping rate, γ_R represents dissipation and the third term describes stimulated scattering into the condensate.

Alternatively, in the case of resonant pumping, the GPE is usually written as

$$i\hbar\frac{\partial \Psi(r,t)}{\partial t} = \left\{ -\frac{\hbar^2\nabla^2}{2m_{\text{LP}}} + V_{\text{ext}}(r,t) - \frac{i\gamma}{2} + g|\Psi(r,t)|^2 \right\}\Psi(r,t) + Fe^{i(\omega_P t - k_P r)}, \tag{1.14}$$

where F is a function describing the amplitude and spatial distribution of the driving laser which has frequency ω_P and wave vector k_P. In contrast to the case of non-resonant pumping, here the phase of the excitation beam is imprinted into the polariton condensate. The majority of theoretical models of polariton systems (at the mean-field level) are based around these two complex GPEs. There may also be modifications in the form of, for example, a density-dependent (saturable) optical gain [29]. The importance of the GPE is its wide applicability and various phenomena which are then expected to occur as a result, i.e. known solutions [30].

With regards to the exact value of the polariton-polariton interaction strength g, it remains a topic of debate. Theoretically, the pure exciton-exciton interaction energy per unit density is expected to be given by $g_X \sim 3E_B a_B^2$ which for typical GaAs QW excitons yields $g_X \sim 3\mu\text{eV}\mu\text{m}^2$ [31]. However, several experiments designed to measure g_X based on the blueshift ΔE of polaritons have yielded inconsistent values spanning over three orders of magnitude between roughly 2 – 2000 $\mu\text{eV}\mu\text{m}^2$ [32–38]. This partly reflects the difficulty of determining the precise density of coupled and uncoupled excitons in the system, and also the fact that there are two contributions to the polariton blueshift: Coulomb interactions of excitons and a phase-space filling which reduces the exciton oscillator strength and hence Rabi splitting. It has also been suggested that even under resonant excitation where polariton-exciton scattering is suppressed, large populations of incoherent excitons (populated through disorder scattering for example) can build up and contribute to the measured blueshift, depending on the timescale of excitation and sample properties [39].

1.3.3 Superfluidity and vortices

Another striking macroscopic quantum phenomenon in condensed matter physics is superfluidity. Following early experimental observations of superfluid behaviour in the liquid helium isotope ^{4}He [40, 41] it was soon suggested by London [42, 43] that superfluids are intimately related with BECs. Meanwhile, Landau was able to highly successfully describe superfluidity (without mention of BECs) using simple postulates still in use today [44]. Specifically, superfluidity occurs because of the linear dispersion of excitations in a system, and leads to flow without friction due to the irrotational nature of the fluid; it is now widely agreed that these postulates are a natural consequence of condensation [see Equation 1.15 below]. As such, both superfluids [45, 46] and atomic BECs [47, 48] exhibit the associated nucleation of quantized vortices under rotation. In the case of polariton systems, fork-like dislocations were observed in the interferograms of early non-resonantly pumped condensates [49] which arise due to the flow of the dissipative polariton condensate around the disorder landscape in the sample. The authors noted that this observation alone was insufficient to establish superfluidity, although it shares similarities. Superfluidity and the Čerenkov regime of polaritons were reported the following year by Amo *et al.* [50] under resonant pumping. This was followed by the observation of oblique solitons [51], which are nonlinear excitations of a perturbed polariton superfluid. Also using coherent excitation, Nardin *et al.* [52] studied the nucleation of vortices and vortex–anti-vortex pairs.

An important relation that follows on from Equation 1.11, allowing one to see the link between superfluidity and BEC, is that linking the condensate flow $\mathbf{v}(\mathbf{r})$ at position $\mathbf{r}$ to the gradient of the phase θ of the wave function:

$$\mathbf{v}(\mathbf{r}) = \frac{\hbar}{m_{\mathrm{LP}}} \nabla\theta(\mathbf{r}). \tag{1.15}$$

which implies that the superfluid is irrotational since $\nabla \times \mathbf{v}(\mathbf{r}) = 0$. In reality it turns out rotation is suppressed by the flow only below some critical velocity, whilst above

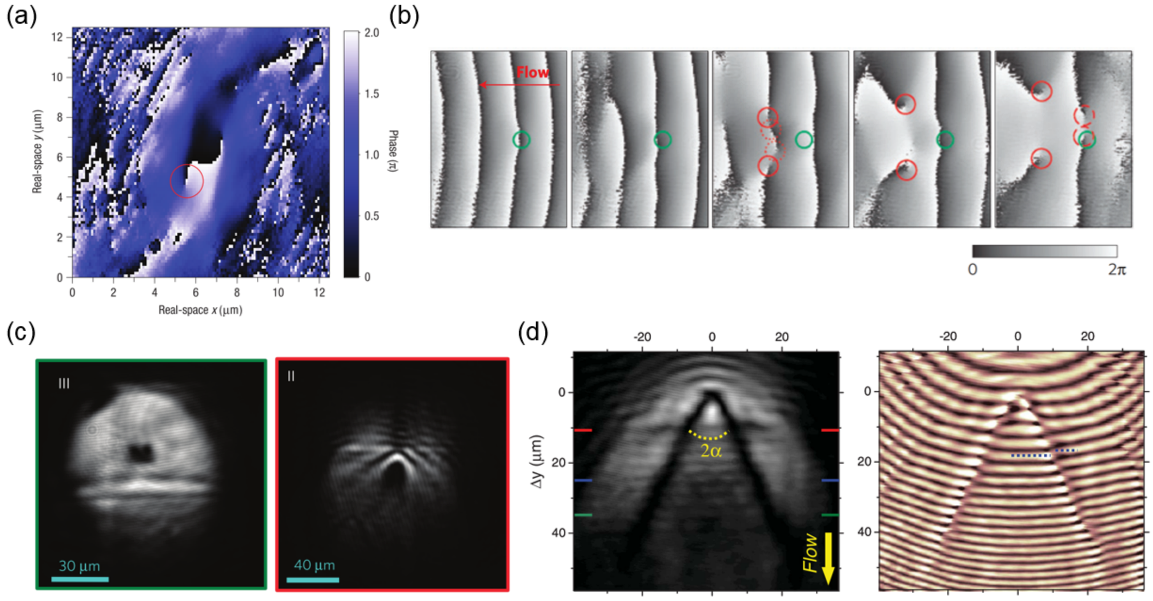

Fig. 1.5 (a) Phase map of a single quantized vortex created under non-resonant excitation in Ref. [49]. (b) Hydrodynamic nucleation of a pair of quantized vortices observed under resonant excitation in Ref. [52]. (c) Superfluid (left) and Čerenkov (right) regimes of polariton flow reported in Ref. [50]. (d) Hydrodynamic nucleation of a pair of oblique solitons and phase map from Ref. [51].

this velocity the phase θ can only change by a multiple of 2π around a closed path in order that Ψ remains single-valued:

$$\oint \nabla\theta(\mathbf{r},t) = 2\pi l. \tag{1.16}$$

The case where $l = 0$ describes a uniform condensate. If one considers the case $l = 1$ with a phase change of 2π, then there must be at least one point inside this path where θ takes any value between 0 and 2π, i.e. a phase singularity. Thus the amplitude of Ψ vanishes at this point, constituting a quantized vortex with the unit of circulation

$$\oint \mathbf{v}.d\mathbf{l} = \frac{\hbar}{m_{\mathrm{LP}}} \oint \nabla\theta(\mathbf{r},t)\cdot d\mathbf{l} = l\frac{h}{m_{\mathrm{LP}}}. \tag{1.17}$$

The velocity around the vortex core is given by

$$\mathbf{v} = l\frac{\hbar}{m_{\mathrm{LP}}}\hat{\mathbf{e}}_\theta. \tag{1.18}$$

This quantization of the velocity field indeed confirms that vortices appear in a condensate in the superfluid regime above some critical velocity, below which imposed rotation is suppressed.

Besides the pinned vortices created under non-resonant excitation [49] and hydrodynamic vortices observed under resonant excitation [52], vortices may also be imprinted optically using Laguerre-Gauss beams [53, 54] or other non-Gaussian excitation geometries [55, 56] or by perturbing a polariton fluid with a Gaussian probe at finite angle [57]. These vortices are single vortices with $l = 1$; it is well known that higher-order vortices are thermodynamically unstable, with both optical [58] and atomic [59] vortices having been observed to break down into arrays of $l = 1$ vortices. However, a recent polariton work demonstrated the possibility of generating higher-order vortices using multiple incoherent pumping spots [60]. The spontaneous emergence of higher-order vortices will also be discussed in this thesis in Chapter 4.

1.3.4 Pattern formation

The spontaneous emergence of spatio-temporal order, or pattern formation, is one of the key mechanisms of self-organization observed in non-equilibrium systems in nature. Many different open physical systems (in biology [61], chemistry [62], physics [63], etc.)

are described by a familiar set of order parameter equations [64, 65] and thus share similar pattern forming properties. Several features of polariton systems make them favourable for pattern forming behaviour. Polaritons exist in non-equilibrium fluids in which particles undergo nonlinear scattering processes, whilst spreading spatially in time (diffracting) which are two key ingredients for pattern formation. The order parameter can be varied by optical pumping, taking the system far from equilibrium across some threshold where spatial instabilities grow and form patterns. The non-trivial polariton dispersion with its point of inflection means that coherently pumped condensates can exhibit nonlinear states which result from a dynamical interplay between dispersion, dissipation and nonlinear interactions [66].

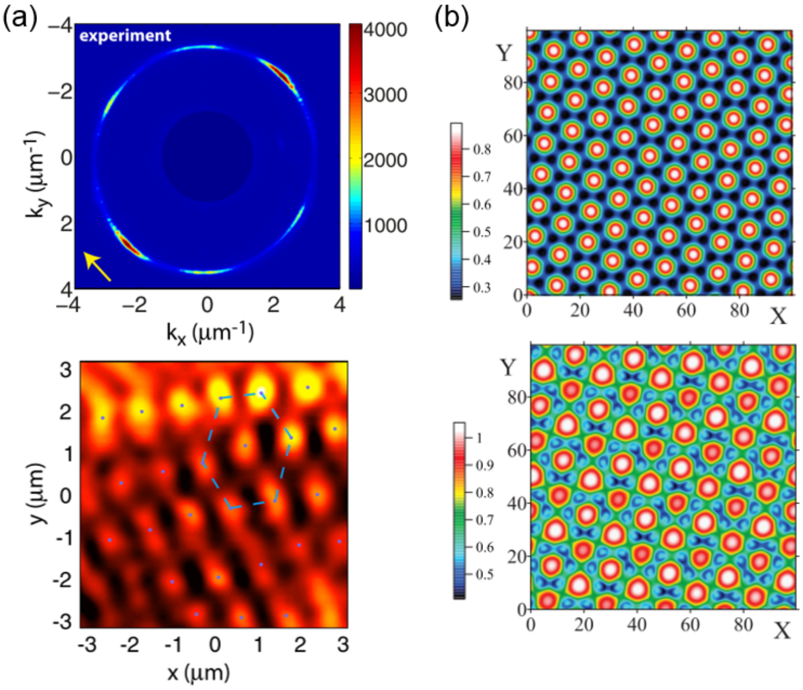

Fig. 1.6 (a) Hexagon patterns observed in a double microcavity structure in Ref. [67]. (b) Theoretical patterns in a homogeneously pumped microcavity from Ref. [68].

Spatial pattern formation can be expressed in terms of the complex Ginzburg-Landau equation which universally describes systems in the vicinity of a symmetry-breaking instability [69, 70]. It takes the form

$$i\frac{\partial \Psi}{\partial t} = c_1 \nabla^2 \Psi + c_2 |\Psi|^2 \Psi + c_3 \Psi, \tag{1.19}$$

where c_1, c_2 and c_3 are complex parameters representing pumping and dissipation in the case of polariton systems, from which one retrieves the GPEs described above. One highly favourable property of patterns formed in polariton systems is the ultrafast response time, with which it has been suggested various applications could be found for non-equilibrium polariton patterns [71].

1.4 Polarization degree of freedom

1.4.1 Pseudospin

So far we have considered the strong coupling between photons and excitons in semiconductor microcavities without regards to the spin degree of freedom. To account for this, one must first consider the underlying spins of the electrons and holes in the QW layer(s). In GaAs and other zinc-blende semiconductors, the valence band splits into two branches (degenerate at $k = 0$) with different effective masses, known as heavy hole and light hole bands. These have respective total angular momenta along the growth axis of $j = \pm\frac{3}{2}$ and $j = \pm\frac{1}{2}$. In GaAs QWs the lowest energy level of a heavy hole is typically lower than any light-hole energy level due to their different confinement energies [7], so excitons are formed by an electron and a heavy hole. As a result, when heavy holes are bound to electrons, which have $j = \pm\frac{1}{2}$, ground state QW excitons may have spin projections of either ±1 or ±2. Since photons carry a spin angular momentum $s = \pm 1$ corresponding to the two circular polarization states, conservation of total angular momentum dictates that $j = \pm 2$ exciton states cannot couple to light to form polariton states, and are hence called dark excitons, while $j = \pm 1$ exciton states are known as bright excitons since they couple to light. This means that right- and left-circularly polarized light couples to $j = +1$ and $j = -1$ exciton states respectively, whilst linearly polarized light excites a linear combination of the two. Polaritons thus have two possible spin projections on the growth axis of a microcavity.

It is convenient to characterize the polarization properties of polaritons using the pseudospin formalism. Pseudospin is a 3D vector which describes both the exciton spin and its dipole moment orientation, which can be measured by calculating the Stokes parameters of the emitted light. The Stokes vector is given by

$$S = \begin{pmatrix} S_0 \\ S_1 \\ S_2 \\ S_3 \end{pmatrix} \tag{1.20}$$

where S_0 is the total intensity. The first Stokes parameter is the degree of linear polarization in the vertical and horizontal polarization basis:

$$S_1 = \frac{I_{\mathrm{H}} - I_{\mathrm{V}}}{I_{\mathrm{H}} + I_{\mathrm{V}}}, \tag{1.21}$$

where I_{H} and I_{V} are the intensities of horizontally and vertically polarized light respectively. The second Stokes parameter is the degree of linear polarization in the diagonal and anti-diagonal polarization basis:

$$S_2 = \frac{I_{\mathrm{D}} - I_{\mathrm{A}}}{I_{\mathrm{D}} + I_{\mathrm{A}}}, \tag{1.22}$$

where I_{D} and I_{A} are the intensities of diagonally and anti-diagonally polarized light respectively. Finally, the third Stokes parameter is the degree of linear polarization in the circular polarization basis:

$$S_3 = \frac{I_{\sigma^+} - I_{\sigma^-}}{I_{\sigma^+} + I_{\sigma^-}}, \tag{1.23}$$

where I_{σ^+} and I_{σ^-} are the intensities of right- and left-circularly polarized light respectively. The overall polarization of an ensemble of polaritons can be any superposition of the individual polarization states and represented as an arrow in the so-called Poincaré sphere, which is shown in Fig. 1.7. The length of the Stokes vector is between 0 and 1, going from completely unpolarized to polarized light.

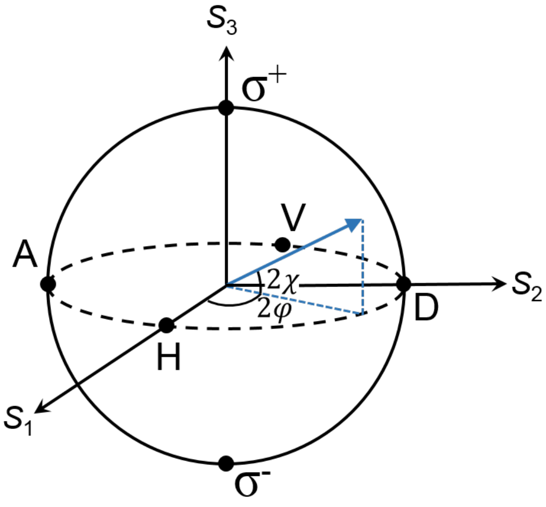

Fig. 1.7 Poincaré sphere.

1.4.2 TE-TM splitting

TE-TM splitting, also known as longitudinal-transverse splitting, refers to an energy splitting between transverse-electric (TE) and transverse-magnetic (TM) polarized polaritons which is seen in the dispersion for oblique angles. The different curvature of the two polarization branches gives TE and TM polaritons different effective masses, i.e. $m_{\mathrm{TM}} < m_{\mathrm{TE}}$. It has two origins: an intrinsic splitting of the cavity mode caused by an angle- and polarization-dependent phase delay upon reflection from the DBRs [72], $\Delta\varphi_{\mathrm{TM}} = \Delta\varphi_{\mathrm{TE}} n_1^2/n_2^2$, and the wave vector dependence of the long-range exciton exchange interaction [73]. Since the former effect is much larger we will neglect the latter effect. The magnitude of TE-TM splitting depends on the deviation of the cavity mode λ_C from the central frequency of the stopband $\bar{\lambda}$ (which can be enhanced by structure asymmetry) and it increases quadratically with angle, reaching a maximum at the angle corresponding to the point of inflection of the LPB [see Fig. 1.8].

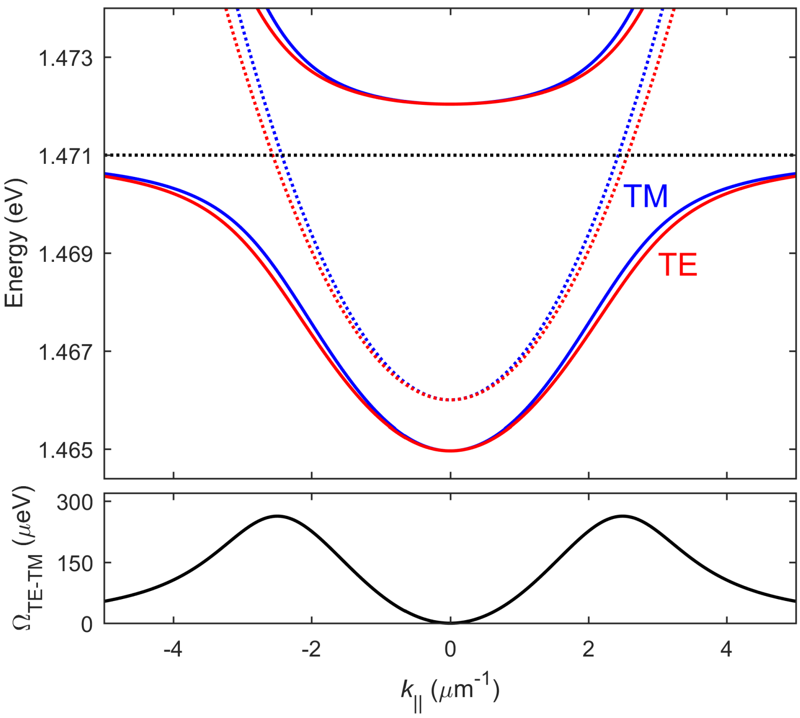

Fig. 1.8 Upper panel: typical polariton dispersion relation in the presence of large TE-TM splitting in a negatively-detuned cavity. Lower panel: dependence of TE-TM splitting on in-plane wave vector.

The Hamiltonian describing TE-TM splitting in a circular polarization basis is given by

$$H_{\mathrm{TE-TM}} = \begin{pmatrix} H_0(\mathbf{k}) & \Omega_{\mathrm{TE-TM}}(k)e^{-2i\varphi} \\ \Omega_{\mathrm{TE-TM}}(k)e^{2i\varphi} & H_0(\mathbf{k}) \end{pmatrix} = H_0(\mathbf{k})I + \boldsymbol{\Omega}_{\mathrm{TE-TM}} \cdot \sigma \qquad (1.24)$$

where $\mathbf{k}$ is the 2D in-plane wave vector and φ is the in-plane angle [see Fig. 1.7]. I is the identity matrix and σ is the Pauli matrix vector whose components are the Pauli spin matrices $(\sigma_x, \sigma_y, \sigma_z)$. $\boldsymbol{\Omega}_{\mathrm{TE-TM}}(k)$ then represents an effective magnetic field

$$\mathbf{\Omega}_{\mathrm{TE-TM}}(k) = \Omega_{\mathrm{TE-TM}}(k) \begin{pmatrix} \cos 2\varphi \\ \sin 2\varphi \\ 0 \end{pmatrix} \tag{1.25}$$

where $\Omega_{\mathrm{TE-TM}}(k)$ is the energy splitting between TE and TM modes. Since the z component is zero, the field is in-plane. The coupling of polariton pseudospin to wave vector $\mathbf{k}$ has strong analogy with spin-orbit coupling, where an effective magnetic field in the reference frame of electrons couples to their dipole moment giving rise to a spin splitting. It can be described by a scalar product between the magnetic field and Pauli matrix vector [74], which is also seen in Equation 1.24. As such, TE-TM splitting is sometimes referred to as photonic spin-orbit coupling.

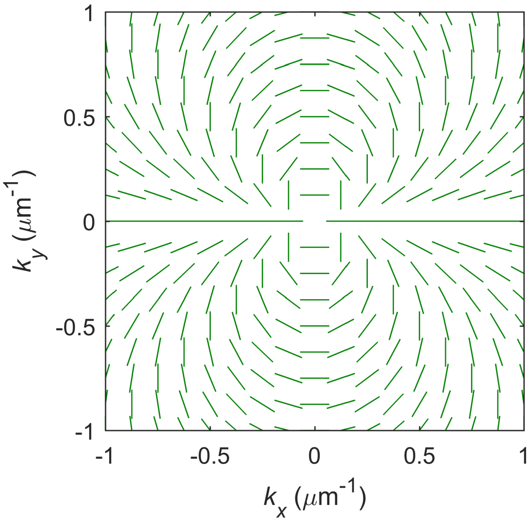

Fig. 1.9 Texture of the effective magnetic field induced by TE-TM splitting in momentum space.

The wave function of a TE-polarized mode with its pseudospin aligned with $\mathbf{\Omega}_{\mathrm{TE-TM}}(k)$ is given by

$$\psi(\mathbf{k}) = \psi(k) \begin{pmatrix} e^{-i\varphi} \\ \\ e^{i\varphi} \end{pmatrix}. \tag{1.26}$$

The relative phase between the two circular polarization components must be 2φ for the mode to remain TE-polarized. If one considers a rotation of the TE mode around the in-plane angle φ in momentum space, between $\varphi = 0$ and $\varphi = \pi$ the relative phase changes by 2π, so the polarization at these two angles is the same. At the intermediate angle $\varphi = \pi/2$, the relative phase between the two polarization components is π and hence the mode is orthogonally polarized with respect to the first case. One can now see that the linear polarization winds doubly during a full rotation around the point $(k_x, k_y) = (0, 0)$ [see Fig. 1.9].

1.4.3 Optical spin Hall effect

For a polariton with pseudospin vector $\mathbf{S}(\mathbf{k})$ its temporal evolution is given by

$$\frac{\partial \mathbf{S}(\mathbf{k})}{\partial t} = \mathbf{S}(\mathbf{k}) \times \mathbf{\Omega}_{\mathrm{TE-TM}}(\mathbf{k}) \tag{1.27}$$

which gives rise to a well-known precession dynamics around the effective field. The texture of this field is best visualized through the optical spin Hall effect (OSHE). In the original proposal by Kavokin and co-workers [75], a wave packet of polaritons with well-defined $\mathbf{k}$ is injected resonantly on the LP branch. Resonant Rayleigh scattering of polaritons from disorder leads to a redistribution around an isoenergetic circle (with fixed $|\mathbf{k}|$) in momentum space, which leads to the appearance of spin domains in the emission [76]. A more recent scheme [77] involves resonant excitation of a microcavity at normal incidence with a tightly focused linearly polarized pump, which is sufficiently large in momentum space to directly excite an isoenergetic ring of states at energy $\hbar\omega_P$. As polaritons radially flow from the pump spot, their pseudospin precesses about $\mathbf{\Omega}_{\mathrm{TE-TM}}(\mathbf{k})$ according to Equation 1.27, which can be written as a function of their radial velocity v_r and radial distance r in the form

$$v_r \frac{\partial \mathbf{S}(\mathbf{r})}{\partial r} = \mathbf{S}(\mathbf{r}) \times \mathbf{\Omega}_{\mathrm{TE-TM}}(\mathbf{k}) \tag{1.28}$$

where the velocity is given by $v_r(k) = \hbar^{-1}\partial E(k)/\partial k$. An analytical solution provided by Flayac *et al.* [77] for the components of the resulting stationary wave function in the circular polarization basis $\mathbf{\Psi}(r,\varphi) = (\Psi_+, \Psi_-)^{\mathsf{T}}$ is given by

$$\Psi_+ = \sqrt{\frac{2N_0}{\pi k_0 r}} e^{-i\varphi}[\cos\varphi e^{ik_{\mathrm{TM}}r} + i\sin\varphi e^{ik_{\mathrm{TE}}r}]e^{-r/r_0}, \tag{1.29}$$

$$\Psi_- = \sqrt{\frac{2N_0}{\pi k_0 r}} e^{+i\varphi}[\cos\varphi e^{ik_{\mathrm{TM}}r} - i\sin\varphi e^{ik_{\mathrm{TE}}r}]e^{-r/r_0}, \tag{1.30}$$

where N_0 is the population of polaritons injected at $r = 0$ and $r_0 = \hbar k_o \tau_{\mathrm{LP}}/m_{\mathrm{LP}}$ gives a mean decay length where τ_{LP} and m_{LP} are the polariton life time and effective mass and k_0 is the mean excitation wave vector, $k_0 = (k_{\mathrm{TE}} + k_{\mathrm{TM}})/2$, with $k_{\mathrm{TE,TM}} = \sqrt{2m_{\mathrm{TE,TM}}\omega_P/\hbar}$. The total population is given by $n = n_+ + n_- = |\Psi_+|^2 + |\Psi_-|^2$. One can clearly see that there are periodic oscillations of the wave functions in both azimuthal and radial directions, creating polarization patterns in analogy with the electronic spin Hall effect in doped QWs where spin textures are created by Dresselhaus and Rashba fields [78].

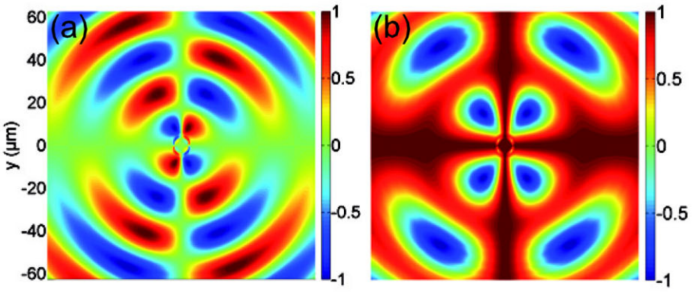

Fig. 1.10 Calculated spin textures generated by the optical spin Hall effect showing the degree of circular polarization (a) and corresponding degree of linear polarization (b) from Ref. [77].

In addition to the TE-TM field, there may be additional effective fields in microcavity systems which are visualized through the OSHE. For example, there may be a field $\mathbf{\Omega}_{\mathrm{an}}(\mathbf{k})$ associated with intrinsic optical anisotropy in the microcavity, such that there is a k-independent energy splitting between linear polarization components, i.e. birefringence, which affects the angular distribution of the OSHE emission pattern [79, 80]. Whilst both this effect and TE-TM splitting create in-plane effective magnetic fields, a nonlinear out-of-plane field $\mathbf{\Omega}_{\mathrm{NL}}(\mathbf{k})$ can be generated by a density imbalance between interacting σ^+ and σ^- polaritons, i.e. $\mathbf{\Omega}_{\mathrm{NL}}(\mathbf{k}) = -(\alpha_1 - \alpha_2)(n_+ - n_-)\hat{\mathbf{e}}_z/2$ where α_1 and α_2 are the interaction constants of polaritons with parallel and antiparallel spins respectively [77].

1.5 Nonlinear optical effects

1.5.1 Parametric scattering

Optical nonlinearities in semiconductor microcavities arise from the repulsive interactions between QW excitons. Indeed, in pure QWs the creation of excitons changes the absorption spectrum by scattering processes [81–83]. However, different states are not distinguishable simply by changing the excitation wave vector, since the dispersion is essentially flat and hence obscured by inhomogeneous broadening. As a result, indirect methods must be used to probe the exciton-exciton scattering. In contrast, in polariton systems the cavity photon component not only significantly reduces the effective mass of particles leading to a much steeper dispersion, it also appreciably reduces the linewidth. Thus, resonant nonlinear optical effects can easily be probed, wherein different states are easily distinguished.

Pioneering experiments reported by Savvidis *et al.* [84] studied the huge optical gain that could be achieved in semiconductor microcavities pumped at finite angle, demonstrating a *stimulated* scattering of particles towards the ground state whose population N_{final} was seeded with a probe. This is a manifestation of the bosonic nature of polaritons, with the scattering proceeding at a rate proportional to $(1 + N_{\text{final}})$. The polariton-polariton scattering (already introduced as a means of polariton relaxation in Section 1.3.1 and enhanced here by final state stimulation) can also be interpreted in the framework of nonlinear optics as a *parametric scattering* process, specifically four-wave mixing (FWM), wherein two pump polaritons elastically scatter into two different directions: the so-called signal and idler states. Energy and momentum conservation are satisfied due to the peculiar shape of the polariton dispersion, such that

$$2k_{\text{pump}} = k_{\text{signal}} + k_{\text{idler}}. \tag{1.31}$$

The behaviour reported by Savvidis *et al.* is typically referred to as optical parametric amplification. Alternatively, when no probe is present similar behaviour can be observed and the system is in the optical parametric oscillator (OPO) regime as first reported by Stevenson *et al.* [85]. The parametrically generated signal polaritons then show increased temporal coherence [53] and long-range order similar to BECs [86, 87], and since no phase is imposed without a probe, there is a spontaneous symmetry-breaking. Intriguingly, it has recently been shown theoretically that the outgoing polariton pairs generated in the parametric process may carry non-zero orbital angular momentum (OAM) [88], such that one can replace the translational momentum k in Equation 1.31 with winding number l and vorticity can spontaneously arise.

1.5.2 Bistability

In OPO experiments, the pump is typically positively detuned by some amount from the lower polariton branch (LPB) to maximize efficiency [89]. This leads to a renormalization of the dispersion relation (blueshift behaviour) via FWM [90]. Given a pump frequency ω_p and corresponding frequency of the LPB at the pump wave vector $\omega(k_p)$, optical bistability occurs when

$$\omega_p - \omega(k_p) > \sqrt{3}\gamma_p, \tag{1.32}$$

where γ_p corresponds to the linewidth of the pump mode. Under these conditions, the pump mode follows a characteristic S-shaped curve with two turning points as a function of driving intensity, where the negative slope corresponds to unstable states. Under forward driving (increasing power), there is a sharp jump at the lower right turning point of the curve, whilst under backwards driving (decreasing power) the population falls back down at the upper left turning point. Hence between these turning points two intra-cavity populations are possible depending on the driving direction. The sharpness of the threshold and size of the bistable interval increase as a function of detuning [91]. The first experimental observation by Baas *et al.* [92] was achieved with excitation at normal incidence, but subsequent theoretical [93, 90] and experimental [94] works considered the rich interplay between bistability and the OPO behaviour.

The case where $\omega_p - \omega(k_p) < \sqrt{3}\gamma_p$ corresponds to the so-called optical limiter regime, where a single sharp transition exists without bistability.

1.5.3 Photon statistics

It is well known that the interaction between light and matter strongly affects the statistical properties of photons. In polariton systems, several theoretical [95, 96]

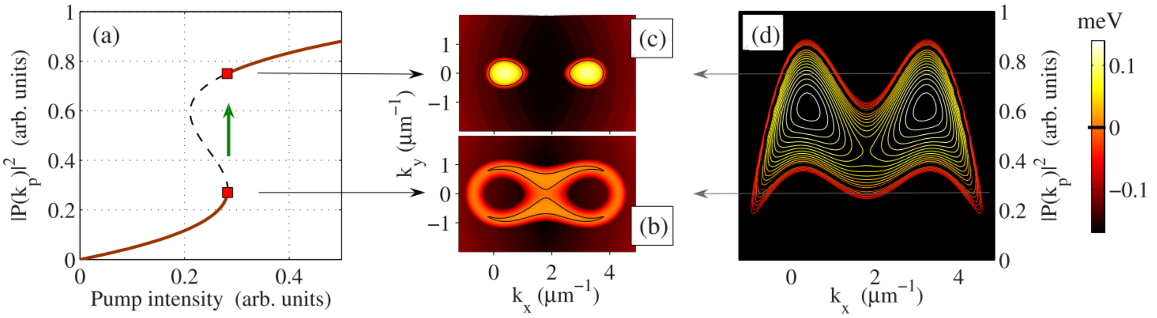

Fig. 1.11 (a) Calculated pump population against driving power. The contour maps in (b) and (c) show the corresponding polariton decay rates below and above threshold respectively. The decay rates are also shown as a function of pump population in (d). Gain and loss correspond to positive and negative values on the colour bar (see right). Taken from Ref. [94].

and experimental [97–99] works have treated the build-up of coherence across the BEC threshold (under non-resonant excitation) considering the second-order coherence function $g^{(2)}$ which passes from ∼2 (thermal state) to 1 (coherent state). More recently, statistical properties of polariton emission have also been studied in the cases of coupled condensates [100] and across the bistability threshold [101], where mode confinement was used in both cases to increase the nonlinearity, and strong bunching behaviour ($g^{(2)} > 1$) was observed. Whilst such photon bunching can in certain cases imply non-classical effects such as squeezing, the other limit where photons are anti-bunched ($g^{(2)} < 1$) has long been sought after and would unambiguously demonstrate a quantum regime. The most direct approach, the so-called polariton blockade [102] necessitates a nonlinearity so strong as to take effect in the single-particle regime, imposing severe requirements on the mode volumes of polaritons given the estimated strength of the self-interaction [37, 39].

1.6 Polaritons in periodic potentials

1.6.1 Confinement methods

So far we have considered the physics of polaritons in planar microcavities, where energy is quantized along the vertical (growth) direction but particles are free to move in the plane of the cavity. It is also possible to engineer *in-plane* potentials for polaritons, by modulating either the excitonic or photonic energy landscape to provide lateral confinement. Examples of methods to create such polariton lattices include metal deposition [103], surface acoustic waves (SAWs) [104], etch-and-overgrowth of the cavity layer (mesa traps) [105] and post-growth etching [106]. Here we will focus on this latter technique, which involves etching cylindrical or square micropillars to induce deep confinement of polaritons on the order of tens of meV, which is not feasible with other methods. This technique has been employed to great success to create 0D trapping potentials [107], arrays of coupled micropillars [108, 109], 1D [110, 111] and 2D [106] lattice potentials, and most recently quasicrystals [112] demonstrating a flexibility which allows tuneable geometries not accessible with the other confinement techniques (SAWs for example).

1.6.2 Band structure formation

In the case of lattice potentials, the polariton energy spectrum critically depends on the depth of confinement U_0, the periodicity a and the recoil energy $E_R = \hbar^2 k_0^2/2m_{\mathrm{LP}}$

where $k_0 = \pi/a$. Considering the simplest case of a 1D lattice as studied in Ref. [110], forbidden energy gaps exist at

$$k = \pm\frac{1}{2}G = \pm\frac{n\pi}{a}, \tag{1.33}$$

where $G = 2nk_0$ defines the reciprocal lattice vector and n is an integer. These energy gaps arise since waves at these values of k satisfy the Bragg condition, creating equal superpositions of left and right travelling waves, i.e. standing waves. The two possible stationary wave solutions (sine and cosine solutions) are distributed differently in real space such that they feel a different potential energy, and hence have different frequencies. The size of the gap is therefore determined by U_0. In reality, the finite polariton linewidth γ_{LP} must also be taken into account, since it ultimately limits the observable band gaps as in early periodic potentials for polaritons [113]. The region between $k = \pm k_0$ defines the first Brillouin zone (BZ) of the lattice, representing the elementary cell of reciprocal space. Since the energy relation $E(k)$ oscillates with a periodicity given by the size of the BZ, it is a highly useful construct which gives information about the energy at any arbitrary value of k.

The same arguments apply in higher dimensions, and periodic lattices of any geometry, formulated through the Bloch theorem

$$\Psi_{\mathbf{k}}(\mathbf{r}) = u_{\mathbf{r}}(\mathbf{r}) \exp(i\mathbf{k} \cdot \mathbf{r}), \tag{1.34}$$

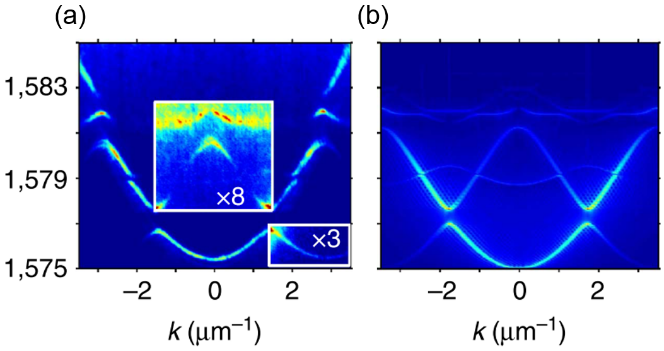

Fig. 1.12 Experimental (a) and theoretical (b) dispersion relations of a 1D periodic potential for polaritons showing forbidden energy gaps, taken from Ref. [110].

which describes the wave function $\Psi_{\mathbf{k}}$ of any particle at position $\mathbf{r}$ under the imposed periodicity of a lattice potential, described by the periodic function $u_{\mathbf{r}}$. This can be used to calculate the photonic bands in a laterally modulated microcavity, and then the energy of the n^{th} lower polariton band $E_{\text{LP},n}$ can be found as

$$E_{\text{LP},n}(k_{\|}) = \frac{1}{2}\Big[E_X + E_{C,n}\Big] - \frac{1}{2}\sqrt{(\hbar\Omega)^2 + \Big[E_{C,n} - E_X\Big]^2}, \tag{1.35}$$

where $E_{C,n}$ is the corresponding photonic band. Since the in-plane motion of particles is small in microcavities, the tight binding model provides a valid (and often analytical) approximation of the system provided U_0 is sufficiently larger than E_R, and is hence frequently used in polariton lattice works [106, 114, 115].

1.7 Polaritonic devices

Now progress towards utilizing the physics of microcavity polaritons to engineer opto-electronic devices will be briefly reviewed. The GPE which typcally describes

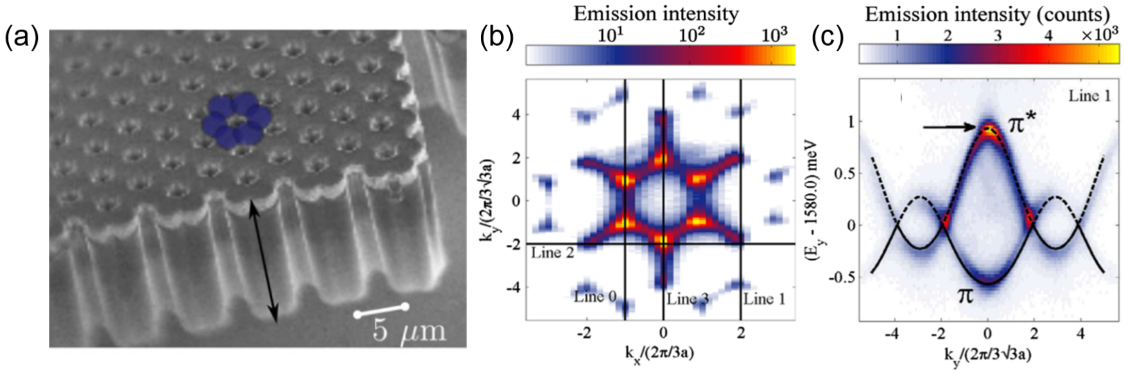

Fig. 1.13 (a) Scanning electron microscope (SEM) image of a honeycomb lattice for polaritons. (b) Reciprocal space image showing the hexagonal shape of the first BZ. (c) Dispersion relation showing the excellent fit (black lines) provided by the tight binding approximation. Figures taken from Ref. [106].

polariton systems allows both bistable and optical limiter behaviour, which provide clear thresholds useful for all-optical logic operations since controllable "on" and "off" states can be created. It has been shown that the spin degree of freedom can be utilized to create spin switches based on different thresholds for spin-up and spin-down polaritons [116]. A variation of the pump-probe scheme in the optical limiter regime may act as a polariton transistor capable of AND and OR operation [117]. Other works have made use of polariton-exciton interactions using a nonresonant pump field, realizing polariton amplifiers [118], tunnelling diodes [119], routers [120], interferometers [121] and condensate switches [122, 123] in various geometries. Beyond all-optical schemes, electrical injection of carriers can be used such as in the spin switch reported in Ref. [124] or to realize coherent light-emitting devices such as the polariton lasers reported for GaAs [125] and GaN [126] cavities, the latter at room temperature. Alternative directions for research into polariton-based devices include the realization of THz emission sources [127, 128] and polariton-mediated superconductivity [129, 130].

The main challenges that remain for future polariton devices are principly related to material properties and device engineering. Practical devices should be stable at room temperature, which immediately rules out the GaAs-based microcavities which have been discussed in detail so far. Currently, it appears that for many of the other material choices where progress has been made, such as GaN [126], ZnO [131], organic polymers [132], and transition-metal dichalcolgenide monolayers [133, 134] the growth and fabrication can be difficult.

Chapter 2

Methods

2.1 Samples

2.1.1 Monolithic cavities

The microcavity samples which form the basis of all work in this thesis were grown using molecular beam epitaxy (MBE) by Dr. Ed Clarke at the EPSRC National Epitaxy Facility based on designs provided by Dr. Paul Walker. They are GaAs $n\lambda/2$ cavities, featuring three or six 10 nm $\mathrm{In}_{0.04}\mathrm{Ga}_{0.96}\mathrm{As}$ QWs embedded at one or two antinodes of the cavity, and all three samples studied feature 23 (27) top (bottom) $\mathrm{Al}_{0.85}\mathrm{Ga}_{0.15}\mathrm{As}$/GaAs DBR layers. The heterostructure designs are based on past optimization of growth parameters as summarized in Ref. [15]. One advantage of introducing a low indium content into the QWs is that the emission wavelength is shifted from that of the GaAs substrate (which is at 1.519 eV [135]), allowing samples to be studied in resonant transmission. A downside is the limit imposed on the number of QWs by the indium lattice mismatch, where strain relaxation leads to highly undesirable crosshatch disorder [15]. This means the Rabi splitting of such samples is typically much less than can be achieved in AlAs cavities with GaAs QWs [136] where the lattice mismatch is minimal.

2.1.2 Etched micropillar arrays

The etched micropillar samples developed and studied in this thesis were fabricated by Dr. Ben Royall of the University of Sheffield Growth Facility, and are inspired by previous works dating back over two decades [137, 107]. Both partially and fully etched samples have been studied. With partial etching, only layers from the top DBR are removed so the QW layers remain unexposed and there is no broadening of the exciton resonance. However, the confinement depth is shallow in this case and there may even still be a weak co-existing unmodulated dispersion if the etching is not sufficiently deep. With fully etched micropillars, the cavity layer is etched all the way through which gives deeper confinement potentials at the expense of some degradation of the exciton linewidth [138].

The main steps of the etching procedure used to process monolithic cavities are as follows:

- Hard mask deposited
- Resist spin-coated
- Exposed to electron beam lithography

- Developed to remove resist in certain areas, revealing desired etch patterns
- Hard mask etched away
- Remaining resist removed with plasma ashing
- Inductively coupled plasma etch
- Passivation

An example of a post-growth etched honeycomb lattice can be seen in Fig. 2.1.

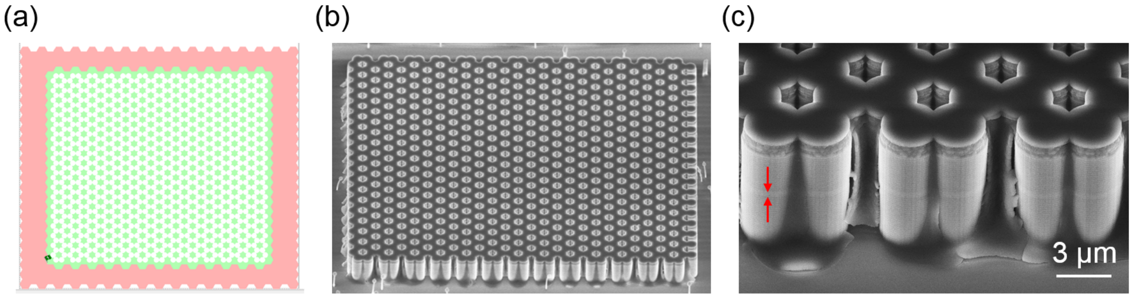

Fig. 2.1 Example of a fully etched micropillar lattice, showing the design used for the fabrication procedure (a), an SEM image of the final etched structure (b) and a close-up of the pillars, where the red arrows show the position of the cavity layer (c).

A summary of all samples used for the work in this thesis can be found in the table below, and details about the layer structures can be found in Appendix A:

Sample	QWs	Notes
1	3	Studied in Chapter 3 at a detuning of ∼-2.5 meV
2	6	Studied in Chapters 4 and 5 at detuning of ∼-20 meV, etched into micropillar arrays and "photonic" Lieb lattice sample
3	3	Studied in Chapter 5 at detuning of -7.5 meV, etched into "excitonic" Lieb lattice sample

2.2 Experimental setups

2.2.1 Sample cooling

All measurements were performed at cryogenic temperatures using a LHe-based continuous flow cryostat attached to a LHe dewar in "pull" operation. Sample temperatures were kept at or below 10 K (monitored using a factory-fitted sensor) by mounting them onto small copper plates which were attached to the cold finger. The parallel facing windows either side of the sample provide wide angular access for both reflection and transmission experiments. The cryostat used features ultra low sample drift and vibration, providing necessary stability for the high-resolution microphotoluminescence spectroscopy scans reported in Chapters 4 and 5. The sample space maintained excellent vacuum during extended periods of operation (below 10^{-6} mbar), meaning the vacuum pump could be turned off during measurements to minimize external vibrations.

2.2.2 Reflection and transmission configurations

As previously discussed, the material composition of semiconductor microcavities determines whether or not optical properties are accessible only by the reflected light or can also be studied by the transmitted light. Since the latter feature is possible for the samples used here, all setups were designed to allow optical experiments in both geometries. At the front side of the cryostat (corresponding to the top DBR side of the sample) a 20× magnification microscope objective (MO) with a focal length

(f) of 10 mm and numerical aperture (NA) of 0.42 was placed. This MO was used for both excitation and collection during non-resonant measurements in the reflection configuration. At the rear side of the cryostat, two lenses were used: another N=0.42 MO with f = 10 mm for the measurements in Chapter 3 and an f = 50 mm camera objective for the measurements in Chapter 5.

2.2.3 Sample excitation

For non-resonant photoluminescence (PL) measurements, which were used in all chapters of this thesis for sample characterization, and exclusively in Chapter 4 to measure the sample in a linear regime, a continuous wave (CW) red diode laser operating at 637 nm was employed. All such measurements were performed in the reflection configuration, with the attenuated laser beam joining the optical axis via a 50:50 beam splitter (BS) to be focused down to the sample surface by the MO. The reflected PL was collected by the same MO and imaged onto the spectrometer. For some measurements it was desirable to excite larger regions of the sample surface, such as for the characterization of the etched structures in Chapters 4 and 5 which in some cases extend over tens of microns. For those measurements an additional lens could be placed in the excitation path before the BS (approximately one focal length from the back focal plane of the MO) to create a larger beam on the sample surface. In order to remove the reflected and scattered laser light from the signal measured on the spectrometer, long pass filters operating at 700 nm or 850 nm were used.

For resonant excitation of samples, which was employed in Chapters 3 and 5 a tuneable mode-locked Ti:Sapphire laser with an 80 MHz repetition rate and 100 ps pulse length was used. A birefringent filter and Gires-Tournois interferometer inside the folded cavity allow for coarse and fine tuning of the emission wavelength between approximately 700 – 1080 nm. An optical isolator was used outside the output aperture of the laser, to prevent potentially damaging back-reflections into the cavity. A half-wave plate (HWP) and polarizing BS were then used in conjunction: a small fraction of the laser signal was siphoned off for the pulses to be analyzed by a photodiode attached to an oscilloscope and an auto-correlator. A graduated rotational ND filter was placed to set a maximum output power (to avoid thermal damage or dielectric breakdown of any optics) and subsequently another rotational filter on a motorized stage for precise and automated control of excitation power. This filter was displaced a small amount (to reduce irradiance) from the focal plane of a 1:1 Keplerian telescope which served to shrink the physical beam size incident on the filter, lessening the influence of the attenuation gradient. Subsequently, a Glan-Thompson prism was used to ensure highly horizontally polarized excitation, which could then be manipulated using either a quarter-wave plate (QWP) or HWP for circular/elliptical or linear polarizations respectively. Whilst most experiments used normal-incidence excitation of samples, resonant excitation at finite angle could be performed using a mirror on a motorized translation stage which allowed control over the lateral position of the beam incident on the large camera objective, which varied the excitation angle. For the large excitation angle used in Section 5.3.1, the angle of the camera objective itself was adjusted and a beam block was used on the front side of the cryostat to filter out the transmitted laser.

2.2.4 PL collection

After being collected by the MO, the PL emission was imaged via a series of confocal lenses onto the entrance slit of a HORIBA TRIAX 550 series spectrometer equipped with a 1200 gr/mm grating, affording a resolution of 0.03 nm ($\sim$50 μeV). Attached to one of the exit ports was a Princeton Instruments PIXIS 1024$\times$1024 pixel charge-coupled device (CCD) with a pixel size of 13 μm.

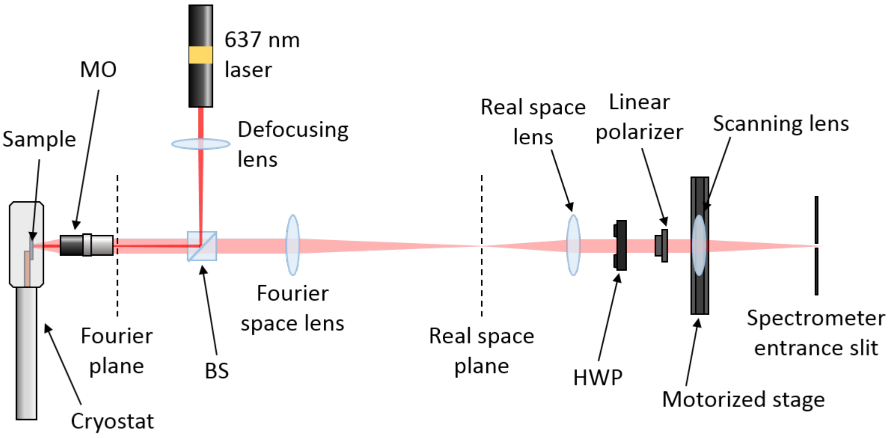

Fig. 2.2 Schematic of the basic PL reflection setup used for sample characterization.

In the collection path, flip mounts were used for the lenses between the MO and final lens. In the simplest possible configuration, intermediate lenses were flipped out of the way to form a real space (near-field) image of the sample emission on the CCD. In order to image the Fourier space (far-field) emission, the next lens after the MO, which was placed one focal length away from its back focal plane, could be flipped into place to project the Fourier components of the PL emission onto the spectrometer.

One focal length away from the Fourier space lens was another real space lens which allowed imaging the near-field emission with a different magnification. An adjustable filter could be used in the real space plane to spatially filter the emission from a selected region in the sample (useful for both real and Fourier space imaging of small structures). Finally, a HWP and linear polarizer were placed in the excitation path to resolve the emission in different linear polarization bases, required to estimate the TE-TM splitting in the sample and for the polarization measurements in e.g. Chapter 4.

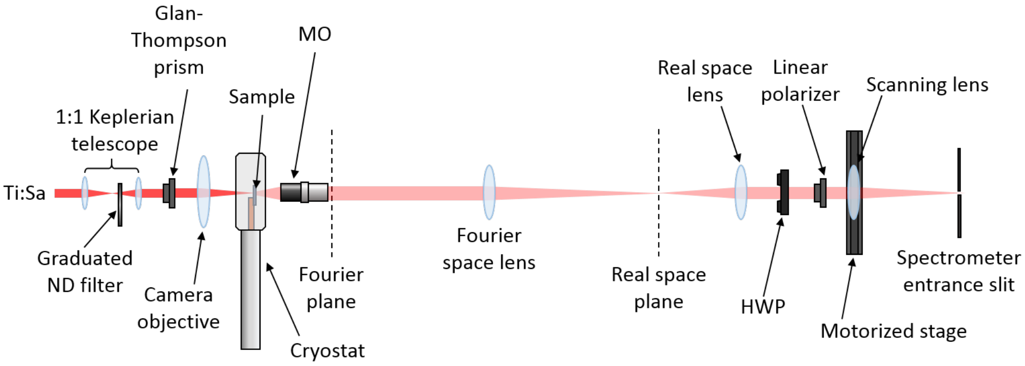

Fig. 2.3 Schematic of the setup used for normal-incidence transmission measurements reported in Chapter 5.

In Chapter 3, photon counting measurements were performed using standard Hanbury Brown and Twiss (HBT) interferometry [97]. This involved using a 50:50 BS to send the microcavity PL emission to two identical avalanche photodiodes (APDs) with a time resolution of 250 ps. Signals from the detectors were recorded as a histogram of coincidences at different time delays, using a timing card with a 24 ps time-bin width. Thus the time resolution of the setup was limited by the APDs, which was longer than the pulse width of 100 ps, but much shorter than the laser repetition period of 12.5 ns, allowing correlations between successive emission events to be recorded. No spectral filtering was required for the experiments owing to the energy-degenerate emission, but spatial filtering of the near- and far-field emission could be achieved using pinholes in the real space or Fourier space planes.

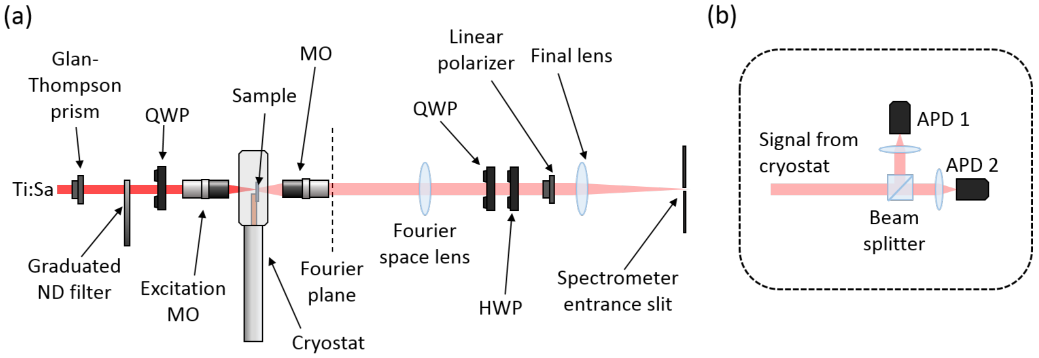

Fig. 2.4 Schematic of the setup used for normal-incidence transmission measurements (a) and photon counting (b) reported in Chapter 3.

2.3 Sample characterization

2.3.1 Fitting the dispersion relation

Samples were characterized by aligning the centre of the k-space PL emission (under low-power non-resonant excitation) to the spectrometer slit in order to record the dispersion at zero in-plane angle. The smooth variation in cavity length across samples induced by halting rotation during MBE growth meant there was generally a broad range of cavity-exciton detunings accessible, so measurements were taken at various positions. The recorded CCD data were loaded into MATLAB, where peak positions corresponding to the upper and lower polariton branches $E_{\mathrm{UP,LP}}$ were extracted for each pixel, corresponding to a different wave vector given by $k_{\|} = \frac{2\pi}{\lambda}\sin\theta$. Recalling and rearranging Equation 1.6 (ignoring loss) the Rabi splitting and exciton energy can be given as

$$E_{\mathrm{LP}}E_{\mathrm{UP}} = E_X\Big(E_{\mathrm{LP}} + E_{\mathrm{UP}}\Big) - \Big[E_X^2 + \frac{1}{2}(\hbar\Omega)^2\Big]. \tag{2.1}$$

which can be solved to find E_X and $\hbar\Omega$ by least squares fitting.

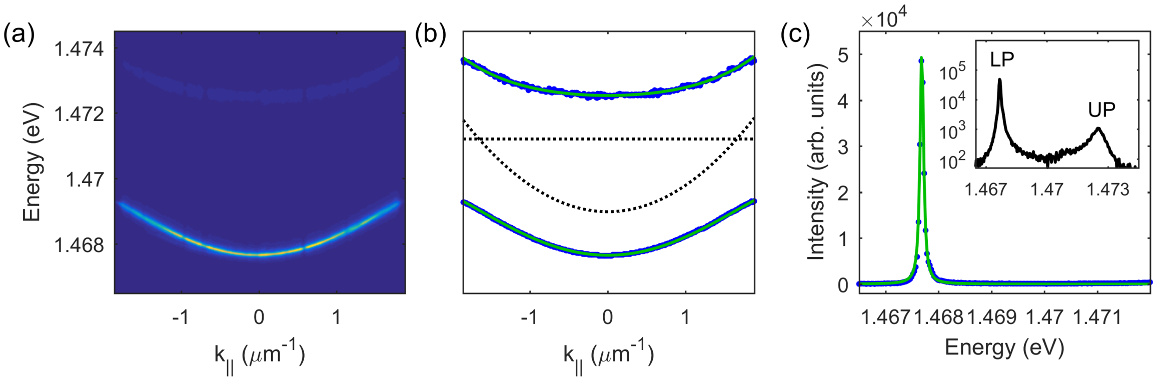

Fig. 2.5 (a) Example of an experimentally measured dispersion relation from Sample 1. (b) Experimental positions of LP and UP energies (blue dots) and fitted curves (green lines). The black dotted lines show the extracted energies of the uncoupled exciton and photon modes. (c) Experimental intensity profile of LP resonance along $k_{\|} = 0$ (blue dots) and fitted Lorentzian peak (green line). The inset shows the intensity profile plotted on a logarithmic scale across a broader energy range, showing clear LP and UP peaks. The fitting gives a cavity-exciton detuning of -2.2 meV, Rabi splitting of 4.3 meV and linewidth of 78 μeV corresponding to a Q factor of 19,000.

The linewidth is given by the full-width at half-maximum (FWHM) of a fitted Lorentzian peak at $k_{\|} = 0$. Acquiring an accurate theoretical fit to the polariton dispersion provides highly useful information for future experiments as it allows the Hopfield coefficients, effective masses and decay rates of polariton states in a sample to be characterized. Access to these details also facilitates theoretical modelling and understanding.

2.3.2 TE-TM splitting

The magnitude of TE-TM splitting [see Section 1.4.2] in a sample can be extracted simply by measuring the microcavity emission in two orthogonal polarization bases, i.e. horizontal and vertical. An example is shown in Fig. 2.6 where curves were fitted to the measured dispersion in these two polarization bases, which in this case point in the sample x and y directions. Separate TE and TM polariton branches can clearly be resolved, with an energy splitting that increases up to the point of inflection and different effective masses.

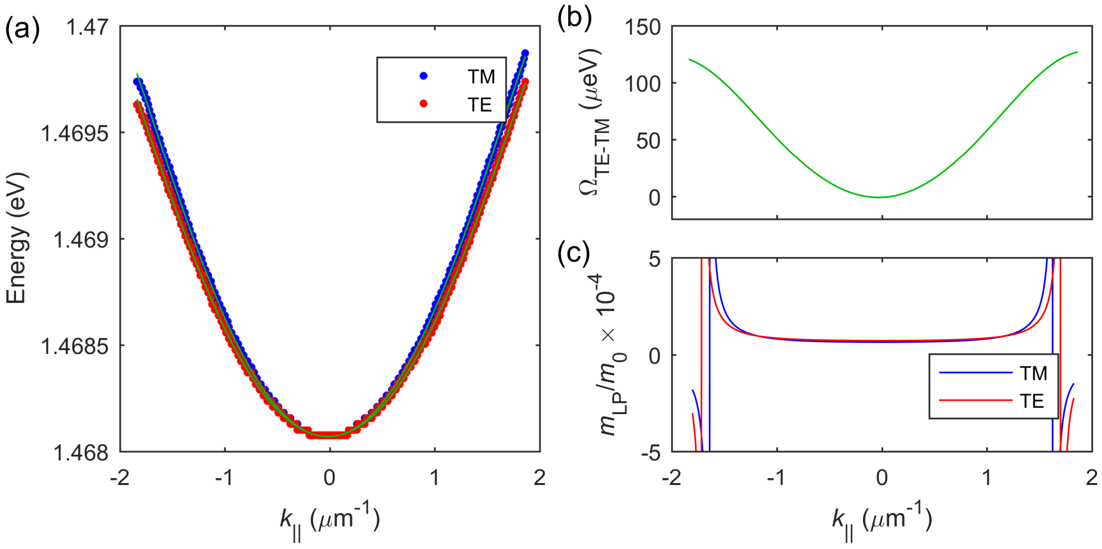

Fig. 2.6 (a) Experimental data from Sample 1 measured in two polarization bases (red and blue dots) with fitted curves (solid green lines). (b) Dependence of the TE-TM splitting on $k_{\|}$. (c) Extracted effective masses for TE- and TM- polarized polaritons. The fits give $m_{\text{TM}} = 0.9m_{\text{TE}}$ and a β factor of 0.06 meV μm^2.

The size of this polarization splitting can be quantified with the TE-TM splitting factor $\beta = \hbar^2/4(1/m_{\text{TM}} - 1/m_{\text{TE}})$ [77].

2.3.3 Optical tomography

In order to gain rich information about the spatial and spectral properties of a polariton system, an optical tomography procedure [139] can be performed in which the scanning lens [see Figs. 2.2] is shifted sideways in increments. At each lateral position of the final lens, a different slice of the near- or far-field emission is aligned with the spectrometer slit, meaning CCD data from successive measurements can be stacked together to produce a dataset with four dimensions corresponding to energy, PL intensity and the two real/k space dimensions.

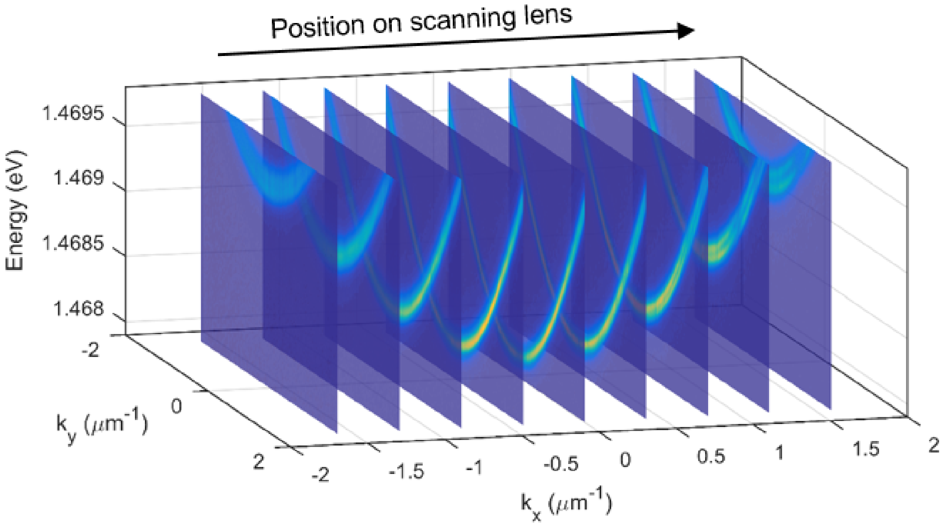

Fig. 2.7 Schematic of the scanning process used to acquire tomographic data.

In Fig. 2.8, it is demonstrated how the tomography process allows the emission to be viewed along three different dimensions in the (E, k_x, k_y) parameter space. It is highly useful in, for example, etched micropillar lattice samples where it enables a full picture of the spatial and spectral structure of the polariton modes to be built up.

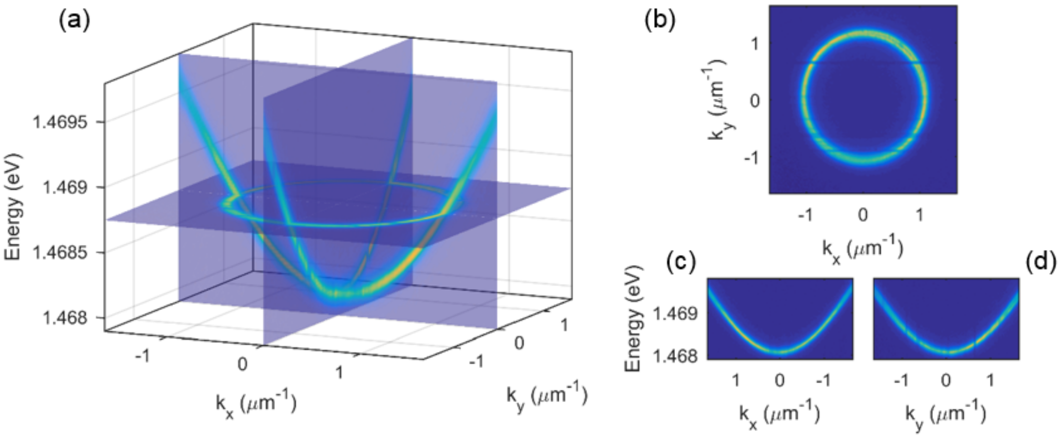

Fig. 2.8 (a) Experimentally measured tomographic PL maps from Sample 1. (b) $k_x - k_y$ map. (c) $E - k_x$ relation. (d) $E - k_y$ relation.

2.3.4 Stokes polarimetry

As described above, HWPs and QWPs were used to resolve the collected PL emission in different linear and circular polarizations. Using Equations 1.21 and 1.22 from the previous chapter, maps showing the Stokes polarization degrees could be constructed by linearly combining images recorded in different bases. In Fig. 2.9 an example of polarization-resolved data is shown. The first two panels correspond to the Stokes parameters S_1 and S_2. The third panel shows the degree of linear polarization (DLP), given by $\sqrt{S_1^2 + S_2^2}$. Two rings can clearly be seen, corresponding to the TE and TM polariton branches. The final panel shows the linear polarization angle (LPA) given by $\varphi = \arctan(S_2/S_1)$. The double winding of the LPA around $k_{x,y} = 0$ shows the influence of the TE-TM field described in Section 1.4.2.

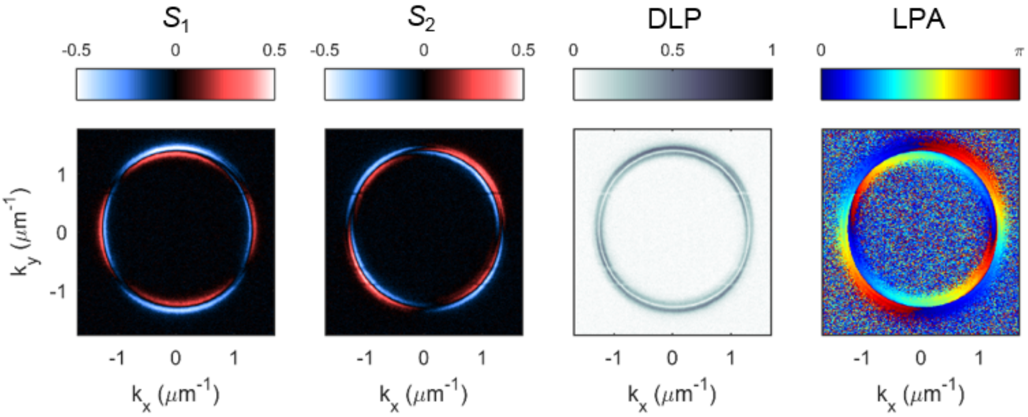

Fig. 2.9 $k_x - k_y$ maps from Sample 1 showing the first two Stokes parameters S_1 and S_2, and the corresponding degree of linear polarization (DLP) and linear polarization angle (LPA).

In practice polarization measurements are typically influenced by terms other than TE-TM splitting, such as localized or extended polarization anisotropy which can arise from sample disorder or strain fields [79].

Chapter 3

Polariton pattern formation and photon statistics of the associated emission

3.1 Background

The phenomenon of spontaneous pattern formation occurs ubiquitously in science in a diverse range of nonlinear extended media [61–65]. The universal mechanism by which stationary patterns emerge from an initially symmetric state has fundamental conceptual significance, combining a cross-talk mechanism acting on different points in space and local nonlinear interactions [140]. As the system is taken out of equilibrium by varying some control parameter, the spontaneous growth of new components via interactions allows localized structures balanced by propagation and nonlinearity to form. In optics, diffraction and nonlinear mixing of electromagnetic waves allows transverse localized structures in various nonlinear media [64, 65].

On the other hand, topological entities such as quantized vortices characterized by a phase winding around a core [see Section 1.3.3] also play an important role in pattern formation in many areas of science, including superconductors and stirred atomic Bose-Einstein condensates (BECs), where patterns formed by vortices with a single winding $m = 1$ have been addressed [45, 46, 141, 47, 48], whereas higher order vortices are unstable. Similarly, in optical systems, high order vortex beams have long been known to be less stable than single vortices [142–144], and the experimental preparation of such beams and nonlinear conversion between them is challenging [145, 146], remaining an obstacle towards realizing many useful applications in optical information processing [147] and quantum entanglement [148]. One intriguing question is whether the nonlinear wave mixing processes which cause generation of new translational momentum components and drive pattern formation in optical systems [64, 65], may lead to the efficient nonlinear generation of vortex beams with sizable orbital angular momentum (OAM). In this chapter such instabilities and the new class of spontaneous patterns that result will be addressed. The main results are published in Ref. [149].

A significant consequence of polariton condensation is quantized vorticity, which emerges from certain solutions of the GPE. So far single vortices have been observed in polariton BECs, resonant and OPO superfluids [49, 55, 54, 57]. However, *spontaneous* patterns driven by higher order vortex modes have not been investigated. Theoretical studies of pattern formation in polariton systems have demonstrated the possibility of

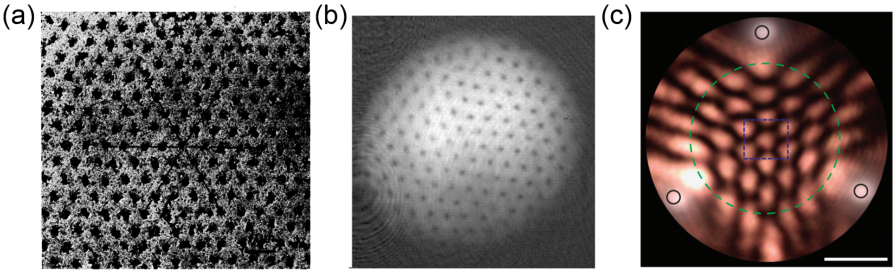

Fig. 3.1 Vortex lattices observed in a type-II superconductor from Ref. [46] (a), a stirred Bose-Einstein condensate from Ref. [48] (b) and interfering polariton condensates from Ref. [150] (c).

roll, labyrinthine and honeycomb patterns [68]. Experimentally, standing wave patterns have been reported using annular pumping geometries in nonresonantly pumped BECs [151, 152] and an extended triangular pattern was observed in a double cavity structure [67].

3.2 Pattern formation

3.2.1 Pumping scheme

For the results reported in this chapter Sample 1 was used [see Section 2.1], and the cavity-exciton detuning was approximately -2.5 meV. The Ti:Sa laser was focused to a 2.5 μm Gaussian spot (the beam size was varied somewhat to produce different patterns) using the N=0.42 MO, and the emission was recorded on the CCD attached to the spectrometer. The pump beam was right-circularly polarized and blue-detuned by between 0.5 and 1 meV from the bottom of the lower polariton branch. A schematic of the excitation scheme can be seen in Fig. 3.2. In this configuration the pump excites polariton plane waves on a ring in momentum space with fixed magnitude of the in-plane wave vector, $|\boldsymbol{k}|$, since the tight focusing of the beam in real space leads to a broad profile in Fourier space where the Gaussian wings directly excite the polariton dispersion [see Fig. 3.2].

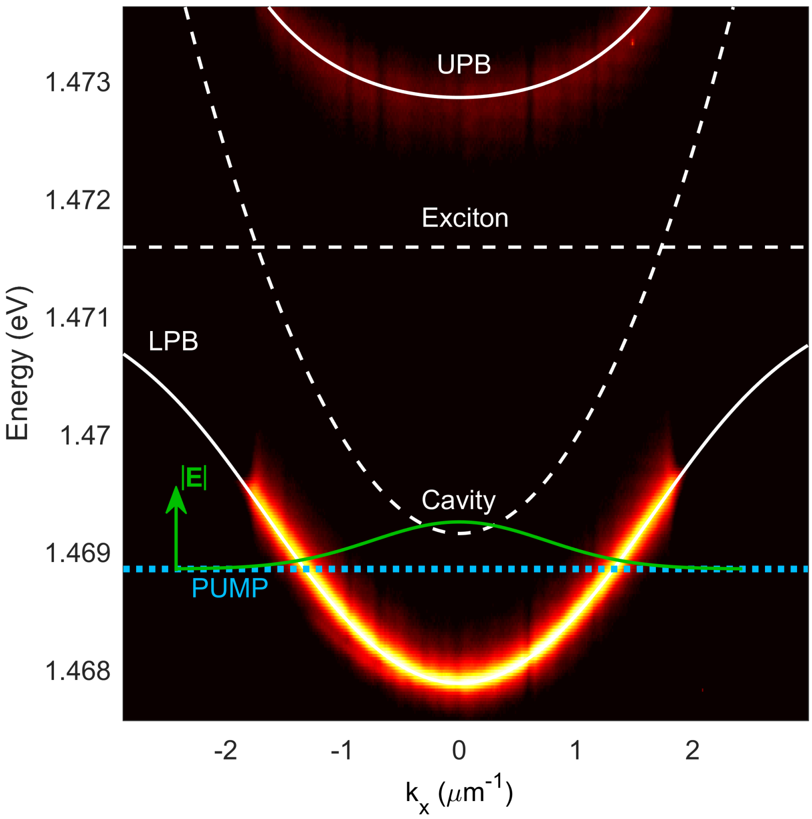

Fig. 3.2 Experimentally measured angle-resolved photoluminescence spectrum with fitted curves (white lines) showing both the uncoupled (dashed) and coupled (solid) modes of the system. The blue dotted line shows the energy of the pump laser and the green solid line shows its Gaussian intensity profile and accompanying axis. $|E|$ is the electric field amplitude.

3.2.2 Power dependence

At low pumping powers the real space polariton density distribution is well approximated by a zeroth order Bessel function of the first kind as can be seen in Fig. 3.3(b) [153], which is the Fourier transform of a ring. Thus the separation of the Bessel rings is determined by the radius of the ring in momentum space. Note that some weak modulation of the low power polariton density distribution is observed in Fig. 3.3(b). The origin of this structure is most likely anisotropy along the crystallographic axes which weakly modulates the cavity transmission, leading to a directionally dependent transmission intensity.

In Fig. 3.3(a) the intracavity population (i.e. the total intensity of the light emitted by the microcavity) is plotted against pumping power. In the low power regime, the system behaves linearly with pumping power. At around 3.5 mW (quoted powers are time-averaged and measured immediately before the excitation objective) a threshold can be observed which is denoted as P_1. At this point there is a change in the slope of the curve, which corresponds physically to the dynamical instability point where the azimuthal symmetry of the intracavity field is spontaneously broken and nontrivial patterns become possible. A selection of the clearest patterns is shown in Fig. 3.3(c)–(g), the first of which is a dipole state with two bright lobes on the innermost ring surrounding the central spot. As the pumping power is increased, the structure evolves to accommodate four lobes on the innermost ring, replacing the dipole state, as observed in Fig. 3.3(d). Beyond this pumping power there is a second threshold denoted as P_2, where there is an abrupt discontinuity in the emission intensity as the intracavity field jumps to a new stable branch [see Fig. 3.3(a)]. In this regime one can see the enlarged central spot with more azimuthal polygon patterns observed at longer radii. Here we see hexagon, heptagon and octagon pattern states (Fig. 3.3(e),

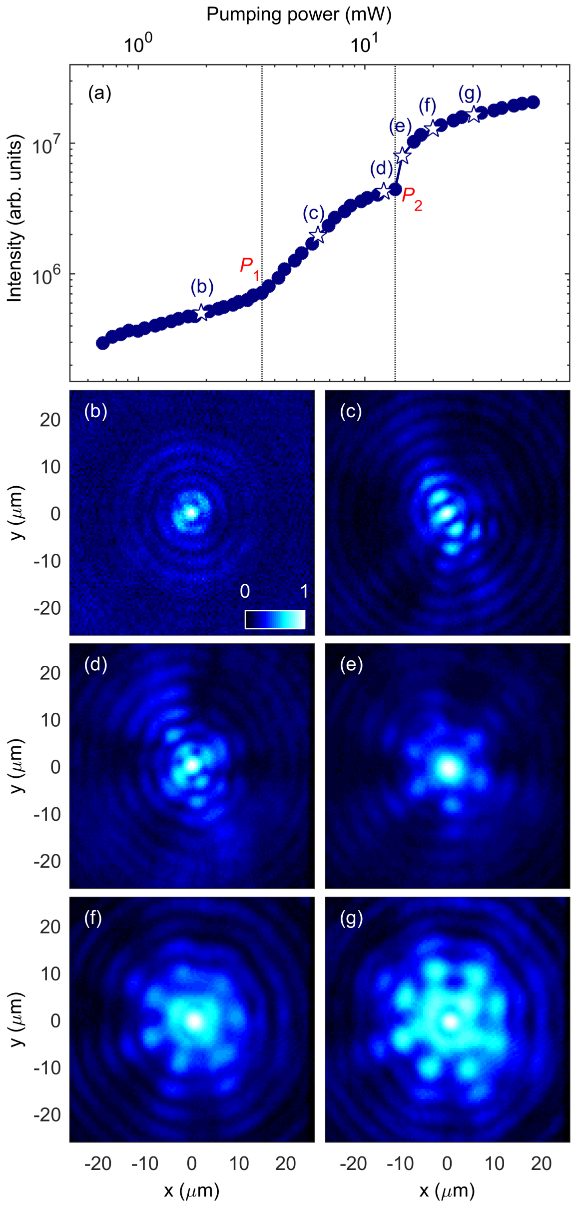

Fig. 3.3 (a) Integrated emission intensity as a function of pump power. The unfilled stars are pumping powers corresponding to the real-space density distributions shown in (b)-(g). P_1 and P_2 mark the onset of parametric scattering and bistability respectively. (b) At low pumping powers we observe a Bessel distribution of polaritons. Above P_1 we form patterns with two (c) and four (d) bright lobes. Above P_2 patterns with six (e), seven (f) and eight (g) bright lobes emerge. The data are plotted on a log scale and normalized.

(f) and (g) respectively). At even higher pumping powers the system enters a turbulent regime where the coexistence of a large number of modes signals the onset of spatial turbulence (not shown).

3.2.3 Mechanism

The mechanisms responsible for pattern formation will now be discussed. With increasing pump power polariton-polariton scattering starts playing an important role and above the P_1 threshold the system becomes unstable against the growth of small perturbations in the form of noise fluctuations, as certain transverse modes begin to experience a gain that overcomes losses. The polariton repulsive nonlinearity also blueshifts the LPB upwards in energy (an effect occurring most strongly at the centre of the pump spot) and scattering channels to new transverse modes open up. This allows macroscopic populations of particles to accumulate in nontrivial pattern states, spontaneously breaking azimuthal symmetry, as pumped polaritons elastically scatter to signal and idler modes at the same frequency and the system enters what can be described as an OPO regime. This energy-degenerate parametric scattering can be seen in Fig. 3.4. Both the blueshift of LPB upwards and parametric scattering results in the change of slope of the power dependence curve above threshold P_1 seen in Fig. 3.3(a) because (i) the excitation of polaritons on a ring in momentum space, which decreases with pump power, becomes more efficiently pumped by the Gaussian pump and (ii) the transfer of polaritons into signal and idler modes increases the energy of the total polariton field inside the cavity.

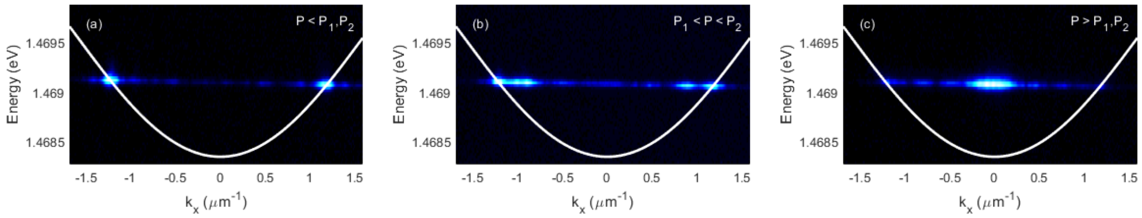

Fig. 3.4 Angle-resolved photoluminescence spectra along $k_y = 0$ for driving intensities in the three distinct regimes. The white lines show the unperturbed LPB.

In contrast to conventional polariton OPOs [154, 85, 155, 94], where pump, signal and idler modes are plane waves with well defined $\boldsymbol{k}$ and different frequencies, the pump state in our case is a coherent superposition of polariton plane waves on a ring, and parametrically generated signal and idler states consist of a coherent superposition of harmonics carrying OAM of opposite sign and residing on the same ring in Fourier space [see Fig. 3.5 and Section 3.4 for experimental and theoretical Fourier space images of patterns]. Signal and idler states with non-zero OAM have been observed in both theory [156, 157] and experiment in conventional OPOs using an external seed carrying OAM [53], and quantized OAM has been shown to be conserved during four wave mixing (FWM) processes [158, 159]. The dynamics of vortex/antivortex pairs which form in OPO condensates perturbed resonantly with a Gaussian probe beam have also been investigated [57]. In our system, these vortex states arise spontaneously without external seeding, and the interference between these vortex/antivortex pairs creates a standing wave with $2m$ lobes, where m represents the winding number of signal and idler modes, which must be equal and opposite. It is then the coherent superposition of this standing wave with the pump field with constant phase which gives rise to stable patterns with m lobes, since alternating lobes experience either constructive or destructive interference with the pump. Such an interference effect is pronounced because of the comparable populations of signal and idler states with the pump, due to highly efficient polariton-polariton scattering. This mechanism is validated by the theoretical model used in Section 3.4, and explains how patterns with arbitrary (even or odd) numbers of lobes can arise without violating any conservation laws.

The allowed structures in a pattern forming system are determined by the nonlinear dynamical instabilities present. Generally, instabilities in fluid dynamics, nonlinear optics, chemical reactions, excitable biological media etc. favour patterns such as rolls, stripes, spots and spirals which have been studied extensively [64, 65]. However, the instabilities driving pattern formation are azimuthal in our polariton system which explains pattern geometries (odd polygons) which have not to the best of our knowledge been observed elsewhere.

In our system, parametric gain is maximized at local maxima of the pump field intensity distribution, i.e. in the centre and on the first and second Bessel rings, where the pump intensity is the highest. In this case the winding number $\pm m$ of vortex/antivortex pairs (and hence the number of bright lobes in the final pattern) is strictly defined by the phase-matching condition for quantization of OAM $2m\pi = 2\pi r k_\phi$, where r is the radius of the Bessel rings, which is given by the magnitude of the wave vector $|\boldsymbol{k}|$ of resonantly injected polaritons (whose wave vector is purely radial), and k_ϕ corresponds to the azimuthal component of the wave vector of signal and idler polaritons acquired during scattering processes. Since the LPB blueshifts as a function of the driving intensity of the pump field, the wave vector $|\boldsymbol{k}|$ of injected polaritons and hence the radii of Bessel rings depends on the pump power. In addition there is a radial dependence of the LPB blueshift created by the inhomogeneous Gaussian profile of the pump, providing the necessary conditions for the formation of various patterns, governed by the pump detuning and polariton dispersion and independent of the system size, characterized by different winding numbers m, and with different values of r which correspond to the value of $|\boldsymbol{k}|$ of the patterns. In accordance with this mechanism, we see that m and r increase with pump power due to blueshift of the polariton dispersion and the decreasing $|\boldsymbol{k}|$ of pattern states [see Figs. 3.3 and 3.5 and Section 3.4 for experimental and theoretical verification]. Also qualitatively the increase in the number of lobes with driving intensity can be explained by increased scattering at higher particle densities, such that more of the radial momentum of injected polaritons is converted to OAM.

The second threshold in the system results from bistability of the coherently driven intracavity field, which is characterized by an S-shaped curve connecting a lower and upper stable branch. The positive feedback between the field intensity and the blueshift energy means that the pumping efficiency rapidly increases as the LPB ground state approaches the pump energy, leading to a superlinear increase in the emission intensity as the intracavity field jumps to the upper bistable branch at the P_2 threshold as seen in Fig. 3.3(a). It is shown in Section 3.3 that this is accompanied by the generation of super-Poissonian light and a huge increase in the signal noise in the window of pumping powers where more than one stable solution exists.

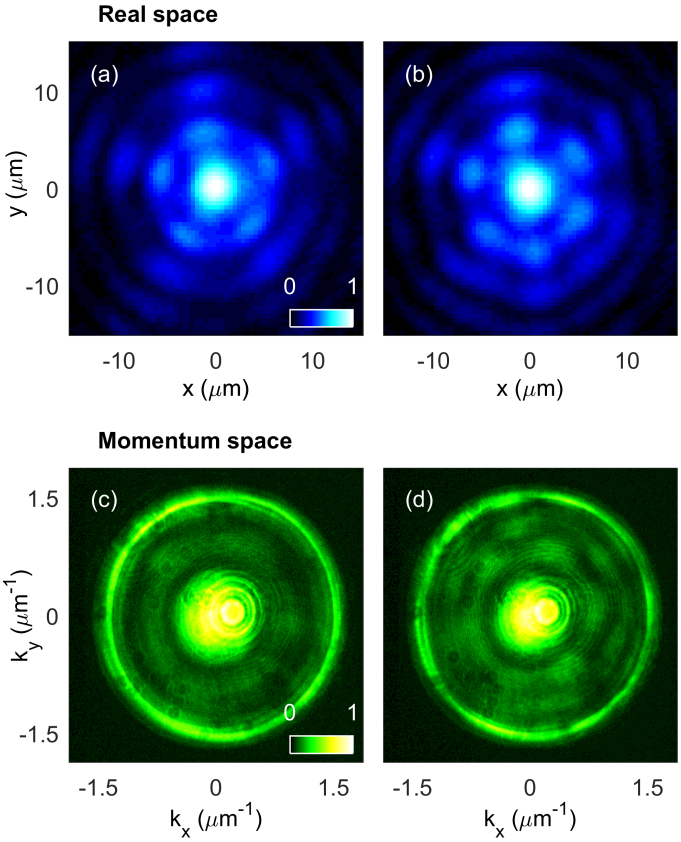

Fig. 3.5 Moving the beam waist position relative to the sample surface by adjusting the focus of the excitation objective allows the transformation from a pentagon (a),(c) to a hexagon (b),(d). Bright lobes can be seen in both real space (upper) and momentum space (lower).

By varying the beam profile under fixed driving intensity, it is possible to switch between different stable patterns, achieving a transition between states with different numbers of lobes. An example of this is shown in Fig. 3.5, where adjusting the size of the pump beam by translating the excitation objective changes the incident power density. This enables the transition from a pentagon to a hexagon, indicating how the most favourable pattern state is highly sensitive to pumping conditions. In addition to the stationary patterns observed in the real space density distribution in Figs. 3.5(a) and (b), accompanying Fourier space images also reveal polygon-type multi-lobed patterns as in Figs. 3.5(c) and (d). Here we see a large emission from $k = 0$, reflecting the fact that the pumping power is above the P_2 threshold and hence the ground state has blueshifted into resonance with the pump. The larger ring simply corresponds to lower density regions of space, i.e. away from the pump spot, where the LPB is unperturbed. It is in between the outer ring and central spot that we see polygon patterns, arising from the directional instabilities (polaritons gain an azimuthal component of polariton wave vector through parametric scattering) experienced during radial propagation from high to low density regions of space.

3.2.4 Pattern rotation

Now the question of what determines the orientation of the patterns will be addressed. In the absence of spatial inhomogeneity, noise fluctuations induce some asymmetry into the initial field distribution created under pulsed excitation. The unstable mode then grows exponentially from this noise, pinning the locations of the polygon maxima. The resulting patterns would be expected to form with random spatial orientation from shot to shot, as they only depend on the relative phase of signal and idler vortex/antivortex states, which is free to evolve from the phase of the pump. Since our measurements are made on macroscopic time scales, averaged over millions of pulses, there must be an additional mechanism stabilizing the patterns and pinning the signal/idler phases. In reality sample disorder [160] provides spatial inhomogeneity which induces weak anisotropy, which can stabilize the spatial orientation of the patterns from shot to shot in experiment. In addition, in experiment it was also found that for some positions on the sample a rotation of the pattern orientation is observed when changing from left to right circularly polarized pumping [see Fig. 3.6]. In other sample positions the rotation was not observed. The weak localized birefringence naturally present in the system will convert circularly polarized light into elliptically polarized light inside the sample, with the direction of ellipticity depending on the circular polarization. Along with TE-TM splitting and spin-dependent polariton-polariton scattering [161–164] this birefringence effect may break azimuthal symmetry and hence define the position of polygon maxima in real space for some positions across the sample where the photonic disorder is weak.

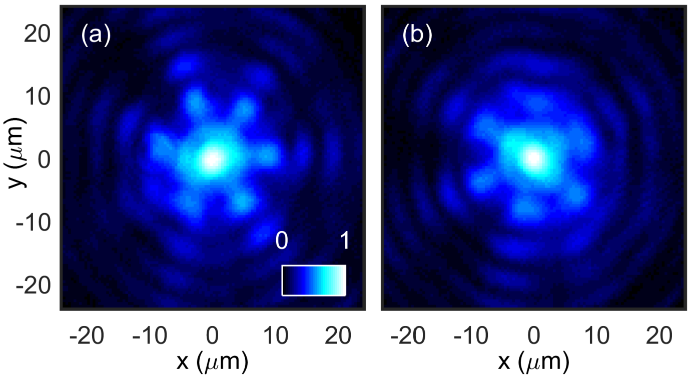

Fig. 3.6 Real space images of stable hexagon patterns. Under a transition from left (a) to right (b) circularly polarized pumping the patterns are seen to rotate. The rotation angle α [see Section 3.4.2] is approximately 30°.

3.3 Photon bunching

The effect of the parametric instability responsible for pattern formation was also investigated via the statistical properties of light emitted by the microcavity under coherent driving. For this the second order correlation function $g^{(2)}$ was measured using a HBT interferometer setup with two APDs with a time resolution of 100 ps [See Section 2.2.4]. Signals from the detectors were recorded as a histogram of coincidences at different time delays, using a timing card with a 24 ps time bin width. The expression for number of coincidences $G^{(2)}$ is given by

$$G^{(2)}(\tau) = \langle n_1(t) n_2(t+\tau) \rangle \tag{3.1}$$

where n_1 and n_2 are the numbers of photons registered on the first and second detectors respectively at time t and $t+\tau$ and the angle brackets represent averaging over time t.

In the pulsed excitation scheme, the raw data corresponding to photon coincidences consists of multiple peaks separated by a delay T=12.5 ns, which is the repetition rate of the driving laser [see inset of Fig. 3.7]. The number of coincidences $G^{(2)}(j)$ between photons in pulses separated by a time jT (where j is an integer) can be obtained by integrating $G^{(2)}(\tau + jT)$ over a range of τ to obtain the pulse areas [97]. Assuming that there is no correlation between intensities of consecutive pulses, $G^{(2)}(j)$ may be normalized to the average area of the uncorrelated peaks at $j \neq 0$. The normalized $g^{(2)}(j)$ is then given explicitly by the formula:

$$g^{(2)}(j) = \frac{\int_{-\Delta t/2}^{+\Delta t/2} \langle n_1(t) n_2(t+\tau+jT) \rangle \, d\tau}{\frac{1}{N-1} \sum\limits_{i \neq 0} \int_{-\Delta t/2}^{+\Delta t/2} \langle n_1(t) n_2(t+\tau+iT) \rangle \, d\tau} \tag{3.2}$$

where N=5 is the number of pulses recorded. The integration range was chosen Δt=6.5 ns, which is roughly half the value of T.

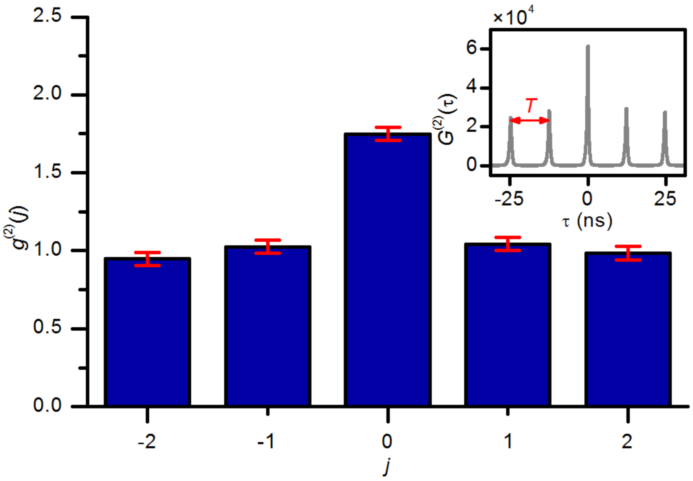

Fig. 3.7 At the bistable threshold the value of $g^{(2)}(0)$ shows a bunched value of 1.75. The corresponding raw data consists of photon coincidences at the HBT photodetectors and is shown in the inset.

The power dependence of $g^{(2)}(0)$ is plotted in Fig. 3.8(a). At pumping powers below the P_2 threshold [1], $g^{(2)}(0)$ values remain at a value of 1 representing a coherent state. At the onset of the P_2 threshold, the $g^{(2)}(0)$ value suddenly increases to 1.75 (see Fig. 3.7 for the $g^{(2)}$ profile of individual signal pulses) before sharply returning to 1 with further increase of pumping power above threshold. Despite the narrow resonance of $g^{(2)}(0)$, these results were very reproducible from day to day measurements.

In addition to the results obtained in our planar cavity sample, photon correlations were also measured in a micropillar. This represents a similar system to our planar cavity but differing in the key aspect of lateral confinement. Parametric scattering is suppressed by the absence of a continuum of transverse modes to which polaritons can scatter, which also precludes pattern formation. A micropillar then represents a system with pure bistability. By selecting the same pumping conditions as for the planar cavity

---

[1] Data in Fig. 3.8 were taken for a linearly polarized pump, for which the strength of polariton-polariton interactions is about twice smaller than in the case of circularly polarized pump. This leads to thresholds P_1 and P_2 higher than in Fig. 3.3.

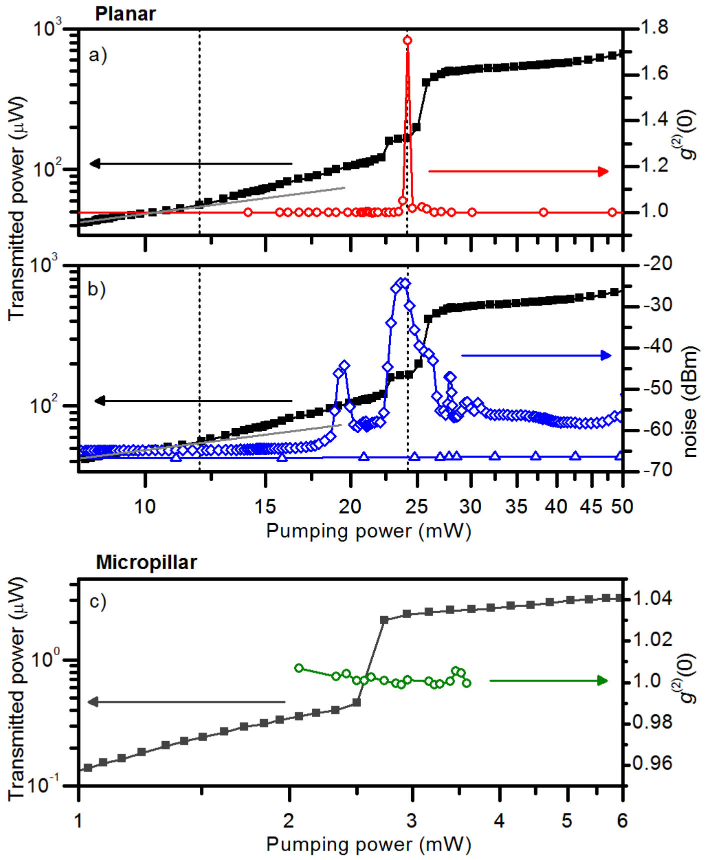

Fig. 3.8 (a) The transmitted power through the planar cavity sample (black squares) and the corresponding value of $g^{(2)}(0)$ (red circles) against pumping power. (b) The measured photocurrent noise of the emitted light (blue diamonds) shown with the detector noise floor (blue triangles) and the transmitted power (black squares) against pumping power. The vertical dotted lines show the two P_1 and P_2 thresholds. (c) The value of $g^{(2)}(0)$ (green circles) along with transmitted power (gray squares) against pumping power in the micropillar sample.

case, the dynamics of a bistable polariton system without inter-mode scattering could be investigated. It was found that in the micropillar the value of $g^{(2)}(0)$ remained at that of a coherent state value across the range of pumping powers as can be seen in Fig. 3.8(c). Such observation indicates that the presence of parametric scattering clearly plays a significant role in the bunching effect in planar structures.

The findings of the $g^{(2)}(0)$ correlation measurements will now be discussed. In the planar cavity case, a value close to unity measured below the P_1 threshold is expected since polaritons are quasiresonantly created by laser pulses, inheriting their coherence properties. In this regime the pump field passes through the cavity with minimal nonlinear interactions. Even above the threshold for parametric scattering, the light generated by FWM processes is in a coherent state, and the statistics of the microcavity emission remain firmly Poissonian. It is only when the bistable threshold is reached that intensity fluctuations are strongly altered with the microcavity light emission exhibiting super-Poissonian statistics.

It has been shown in a multi-mode bistable polariton system that energy can gradually accumulate with time (within tens of picoseconds) in modes populated through parametric scattering, followed by a sharp transition from the lower to the upper steady state branch when the internal energy of the system is sufficient [165]. A similar process is responsible for the bunching effect observed in our system, where signal and idler modes accumulate particles through the parametric instability responsible for pattern formation within the duration of the pump pulse, before a strongly superlinear increase (in time) of pump, signal and idler fields launches the system onto the upper bistable branch (so-called "blowup" temporal dynamics). In the vicinity of this threshold the populations of pump, signal and idler modes integrated over the pump pulse duration are highly sensitive to initial conditions, and thus to quantum fluctuations of the pump and photonic field inside the cavity. This leads to strong noise in the cavity emission from pulse to pulse and thus to the super-Poissonian photon bunching observed experimentally. By contrast, in a single micropillar cavity there is no superlinear temporal dynamics of the intracavity field due to the absence of parametric scattering channels to transverse modes, and before the bistability threshold is reached (the right turning point of the S-shaped curve) the value of quantum fluctuations is insufficient to drive the system into stochastic resonance, precluding the observation of the strong bunching effect.

Above the P_2 threshold, the system resides on the upper bistable branch with a well defined polariton population integrated over each pump pulse, so the value of $g^{(2)}(0)$ is restored to unity, and the statistics revert back to Poissonian. The behaviour in our system differs from that of non-resonantly pumped polariton lasers and condensates [98, 99, 166] where photon bunching is attributed to thermal populations of polaritons, which subsequently scatter into the coherent ground state at higher intensities or longer times in the case of above-threshold pumping.

Simultaneously, the photocurrent power noise arising from the microcavity emission was measured. The principle is that the photocurrent generated by the microcavity emission may also fluctuate significantly on longer time scales (than the laser period) due to various classical noise contributions which would lead to an increase of signal noise at lower frequencies, so it is complementary to the measurements of $g^{(2)}$ [167]. The polariton signal was sent to a Si photodiode detector, generating a photocurrent which was amplified. Its power noise was analyzed in the frequency domain by a spectrum analyzer. The photocurrent was acquired in a 1 MHz bandwidth around a central frequency of 5 MHz, well separated from the 80 MHz repetition rate of the laser.

The power dependence of the noise signal is shown in Fig. 3.8(b). At low pumping powers < 10 mW, noise levels remain relatively close to the detector noise floor, depicted by unfilled triangles. An increase of noise by a few dB above this level appears at pumping power ~ 15 mW before the bistability threshold $P_2 \sim 25$ mW. This is followed by a further sharp increase (20 dB) in noise at $\sim$18 mW and then at $\sim$22 mW pumping powers, producing a wide peak with a shoulder at a lower, but still elevated noise level, in the vicinity of the $P_2 \sim 25$ mW threshold. The noise reduces at higher powers, but oscillations in the noise signal are still seen. The underlying physics differs from the power dependence of $g^{(2)}(0)$, which reflects amplification of high frequency (80 MHz) quantum fluctuations, i.e. pulse-to-pulse photon number variations. By contrast, low frequency (5 MHz) noise is likely to originate from amplified classical noise of the pump field, which grows quadratically with excitation power and is probably much stronger than the quantum noise of the pump which depends linearly on excitation power [167]. The noise amplification occurs through generation of fluctuating signal and idler modes and possibly stochastic jumps between lower and upper bistable polariton states similarly to the mechanisms responsible for the enhanced $g^{(2)}(0)$, but this may happen over a broader interval of pump energies since classical fluctuations are stronger than quantum. Different maxima in the power dependence of noise are probably governed by the parametric instabilities responsible for pattern formation below and above the bistability threshold P_2 as observed in Fig. 3.3. It is known in other nonlinear pattern forming systems that noise may be amplified at pump parameters where there is crossover between different pattern states, referred to as domain coexistence [168]. In that case the noise originates from two competing unstable modes both experiencing positive growth rates, very similar to the situation discussed theoretically in the next section.

3.4 Theoretical analysis

3.4.1 Linear stability analysis

A theoretical analysis by Oleg Egorov from Universität Würzburg which provides additional insight into the mechanisms underlying pattern formation will now be presented, substantiating further the interpretations presented in the previous section. Single-shot numerical simulations of the propagation of a pump beam through the cavity in the presence of symmetry-breaking perturbations were performed. The system can be described by the widely accepted mean-field model for excitons strongly coupled to circularly polarized cavity photons [169, 7, 170, 151, 92] whose fields are given as follows:

$$\partial_t E^{\pm} - i\nabla_{\perp}^2 E^{\pm} + \left[\gamma - i\left(\omega_p + \delta\right)\right] E^{\pm} = i\Omega_R \Psi^{\pm} + E_p^{\pm}(x,y), \tag{3.3}$$

$$\partial_t \Psi^{\pm} + \left[\gamma - i\omega_p\right] \Psi^{\pm} + i\left(\left|\Psi^{\pm}\right|^2 + \alpha\left|\Psi^{\mp}\right|^2\right) \Psi^{\pm} = i\Omega_R E^{\pm}. \tag{3.4}$$

Here $E^{\pm}$ and $\Psi^{\pm}$ are the complex amplitudes of the photonic field and coherent excitons obtained through a standard averaging procedure of the related creation or annihilation operators. Normalization is such that $g^{-1}|E^{\pm}|^2$ and $g^{-1}|\Psi^{\pm}|^2$ are the photon and exciton numbers per unit area. Here g is the exciton-exciton interaction constant. The symbols + and - represent right and left circular polarization of light and the corresponding exciton spins. γ denotes the cavity and exciton damping constants. $\omega_p = \omega - \omega_0$, $\delta = \omega_0 - \omega_c$ describe the detunings of the pump frequency ω and the cavity ω_c from the excitonic resonance ω_0. Ω_R is the Rabi frequency. The two spin components of the excitons are coupled by the dimensionless parameter α which exhibit values around $\alpha =$ -0.1 [169, 7, 170].

The analysis begins at the onset of the P_1 threshold, with a circularly polarized coherent pump which has an azimuthally-symmetric Gaussian profile:

$$E_p^+(x,y) = A_0 e^{-r^2(R^{-2}+i\eta)}, \tag{3.5}$$

$$E_p^-(x,y) = 0. \tag{3.6}$$

where $r = \sqrt{x^2+y^2}$. A finite phase curvature of the pump beam is characterized by the constant η and reflects the fact that in experiment the beam waist was displaced with respect to the position of the quantum wells, resulting from the small adjustments of the excitation objective from its focal distance used to produce the most pronounced patterns. A non-zero and negative η is used in the theoretical analysis to provide a good qualitative agreement with experiment, although the phase curvature is not fundamental to the underlying nonlinear processes themselves so patterns are still observable in both experiment and theory over a range of values of η.

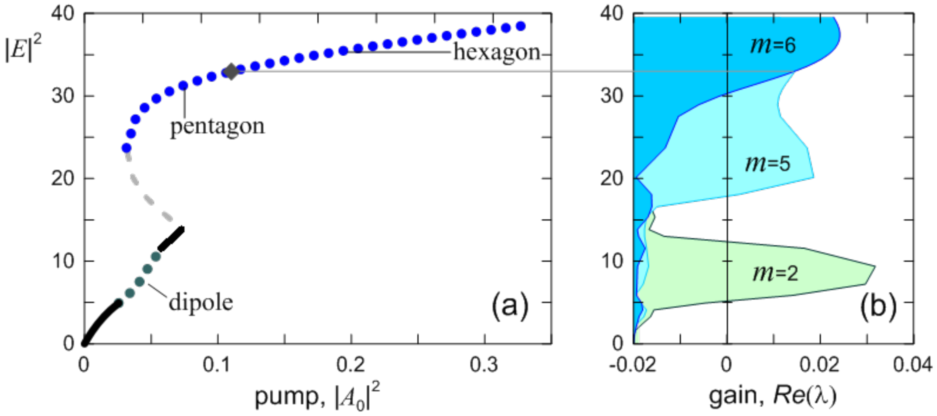

Fig. 3.9 (a) Maximum intensity of radially-symmetric steady-state against pump power. The pump beam has a Gaussian profile with radius R=18 μm and phase curvature $\eta = -0.02\ \mu\text{m}^{-2}$. Stable states are depicted by solid lines whereas dotted lines show unstable solutions breaking spontaneously their radial symmetry. The dashed line represents solutions which are unstable against $m = 0$ perturbations. (b) Growth rates of leading unstable modes (with angular numbers m=2, 5, 6) against intensity of the radially-symmetric solution. Other parameters: δ=-2.561 meV, ω_p=-3.3 meV, γ=0.02 meV, Ω_R=2.142 meV. These parameters are very close to the experimental conditions of Fig. 1.

First, the radially-symmetric steady-state response which is independent of the polar angle θ=arg$(x + iy)$ was considered. Applying the Newton iterative method, radially-symmetric steady-states were calculated for different driving intensities, shown in Fig. 3.9(a). In agreement with pioneering works on exciton-polariton dynamics [92], the obtained solutions are bistable provided the pump frequency is blue-detuned by more than a certain amount with respect to the LPB. The threshold P_2 corresponding to the abrupt intensity transition in the experiment [see Fig. 3.3(a)] is expected to occur at the turning point of the lower bistability branch, approximately where the pump equals 0.075 in Fig. 3.9(a). In the limit of weak pumping, the spatial intensity profiles of the intracavity field possess the previously described ring structure as seen in Fig. 3.10(a). This confirms that the pump beam excites polaritons on the LPB which are in resonance with the pump frequency most strongly, compared to the $k = 0$ mode, which is comparatively very weakly driven [see Fig. 3.10(b)].

A full two-dimensional linear stability analysis of the localized structures was also performed, which provides insight into the pattern selection process by showing which transverse modes experience parametric gain. The linear perturbations were assumed to be vortices carrying OAM with the general form

$$a_+(r)e^{im\,\theta+\lambda(m)t} + a_-^*(r)e^{-im\,\theta+\lambda^* t} \tag{3.7}$$

where the azimuthal winding number is integer, m=0, 1, 2, 3... . The solution becomes unstable if at least one of the obtained eigenmodes possesses a positive growth rate, i.e. $\mathrm{Re}[\lambda] > 0$. The linear stability analysis shows that the radially-symmetric solutions can become unstable with respect to perturbations breaking the azimuthal symmetry, i.e. with $m \neq 0$, shown in Fig. 3.9(b). For instance, the linear eigenmode with m=2 can destabilize the steady-state field profile for pump intensities below the bistability threshold [see Figs. 3.9(a) and (b)]. Direct numerical simulations within the original equations show that this instability develops with time and results in the formation of a dipole-like steady-state with three intensity peaks [see Figs. 3.10(c) and (d)] in strong qualitative agreement with the experimental observation of Fig. 3.3(c).

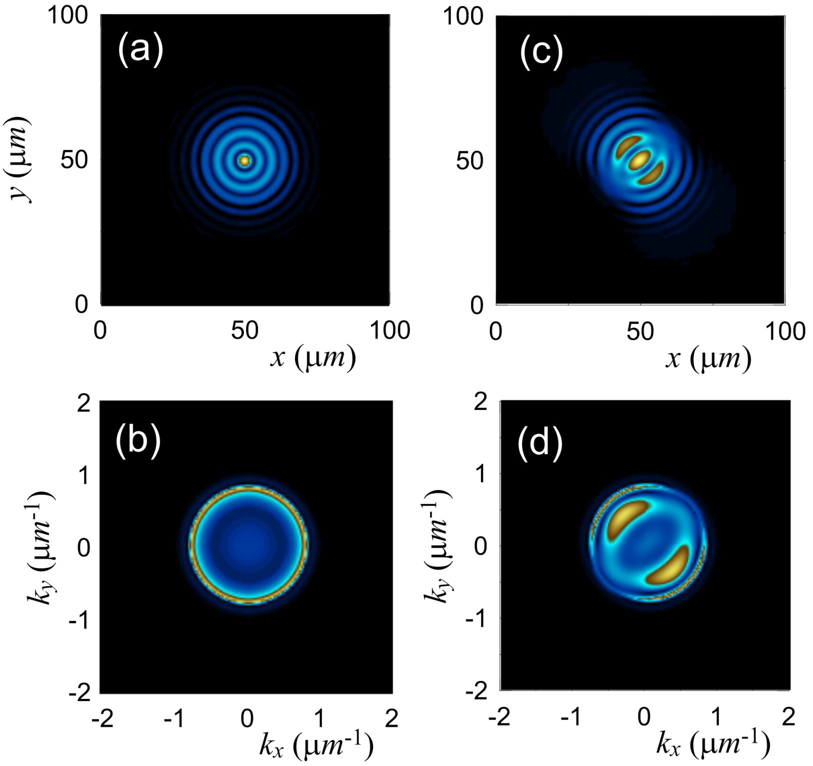

Fig. 3.10 Intensity profiles of steady-state solutions are shown in real (a, c) and momentum (b, d) space. (a, b) Radially-symmetric solution in a low-pump limit for A_0^2=0.01. (c, d) Stable dipole state for A_0^2=0.0529. Other parameters are similar to those of Fig. 6.

For stronger driving intensities above the bistability threshold, the radially symmetric solutions undergo azimuthal instabilities with larger winding numbers m. For instance the growth of the unstable mode with winding number m=5 results in the formation of the pentagonal structures shown in Figs. 3.11(a) and (b). At even higher pumping intensities, the growth rate of the unstable mode with m=6 overtakes that of the pentagon and thus a hexagon becomes the most favorable solution, winning the mode competition [see Figs. 3.11(c) and (d)]. Such a behaviour is in agreement with pentagon and hexagon experimental observation above bistability threshold in Figs. 3.3(f) and 3.5. A spatial Fourier analysis [see Figs. 3.11(b) and (d)] shows strong agreement with experimentally measured far-field intensity profiles above the bistability threshold seen in Figs. 3.5(c) and (d), showing the strongly populated $k = 0$ mode surrounded by a polygon pattern and the sustained ring structure at larger wave number, which itself shows some azimuthal dependence on the intensity. In numerical simulations it was found that switching between the pentagon and hexagon states is possible by changing either the radius or the phase curvature of the pump beam. In experiment both of these scenarios correspond to shifting the focus position of the excitation objective, which irradiates the sample with a different cross-section of the input beam. It was shown in Fig. 3.5 that this switching behavior is simple to achieve, as expected by the theoretical model used here. Despite the simplicity of the model, the above stability analysis of the radially symmetric polariton patterns offers very good qualitative agreement with the near- and far-field pattern profiles observed in Figs. 3.3 and 3.5, both before and after the P_2 threshold.

3.4.2 Pattern rotation

In order to clarify the physics behind the polarization-dependent rotation of patterns numerical modeling of the dynamics within the mean-field model was also performed. As discussed previously [see Eqs. 3.3 and 3.4]:

$$\partial_t E^{\pm} - i\nabla_{\perp}^2 E^{\pm} + \left[\gamma - i\left(\omega_p + \delta\right)\right] E^{\pm} + i\beta\left(\partial_x \mp i\partial_y\right)^2 E^{\mp} + i\Delta_{XY} E^{\mp} = i\Omega_R \Psi^{\pm} + E_p^{\pm}(x, y), \tag{3.8}$$

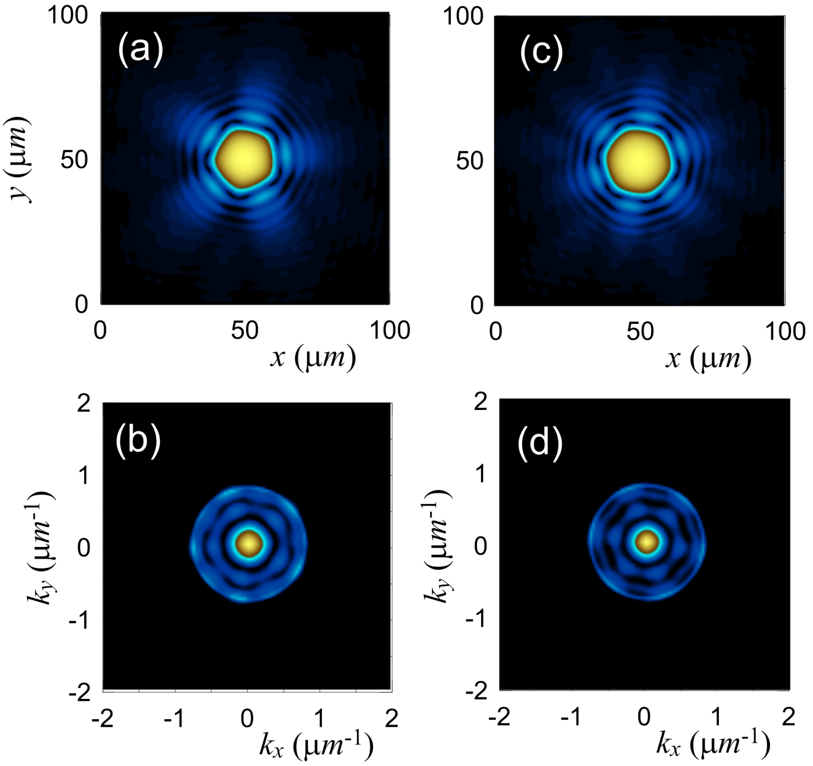

Fig. 3.11 Intensity profiles of steady-state solutions are shown in real (a,c) and momentum (b,d) space. (a,b) Pentagon state for A_0^2=0.09. (c,d) Hexagon state for A_0^2=0.16. Other parameters are similar to those of Fig. 6.

Additionally to the already discussed parameters the TE-TM splitting of the cavity is taken into account by β and birefringence through the parameter Δ_{XY}. The interplay between TE-TM splitting and birefringence resulting in the polarization-dependent rotation of pattern states will be demonstrated. Figs. 3.12(a) and (b) show a typical example of two real space intensity patterns excited by coherent pump beams with opposite circular polarizations. The orientation of the pattern is defined by a minimum angle between an axis going through pattern maxima and the x axis. Rotation is given by the angle α^- between the two axes under excitation with left circular polarization of the pump beam and angle α^+ for right circular polarization as in Figs. 3.12(a) and (b). In order to elucidate the influence of different physical mechanisms numerical simulation of the total angle of pattern rotation ($\alpha = \alpha^+ - \alpha^-$) depending on the birefringence parameter was simulated for two values of TE-TM splitting, as can be seen in Fig. 3.12(c). From fitted curves to the experimentally-measured dispersion relation the TE-TM splitting factor was found to be $\beta \sim 0.062$ meVμm^2, which lies between the values used in simulations. It was found that for vanishing birefringence, the patterns are oriented randomly. For small birefringence <0.03 meV the patterns are oriented along the x axis and at intermediate values of birefringence (0.03 meV $< \Delta_{XY} <$ 0.06 meV) the pattern axis rotates with respect to the x axis by $\alpha^+(\alpha^-)$ angle for a left (right) circularly polarized pump. For large birefringence >0.07 meV the patterns again tend to orient along the x axis. These numerical simulations show that patterns can be controllably rotated by about 30° by switching between right and left circular polarization of the pump provided the birefringence parameter is strong enough. The theoretical values of Δ_{XY} at which the rotation of the pattern is observed are consistent with the typical experimental values of birefringence (0.02-0.05 meV) in GaAs microcavity samples.

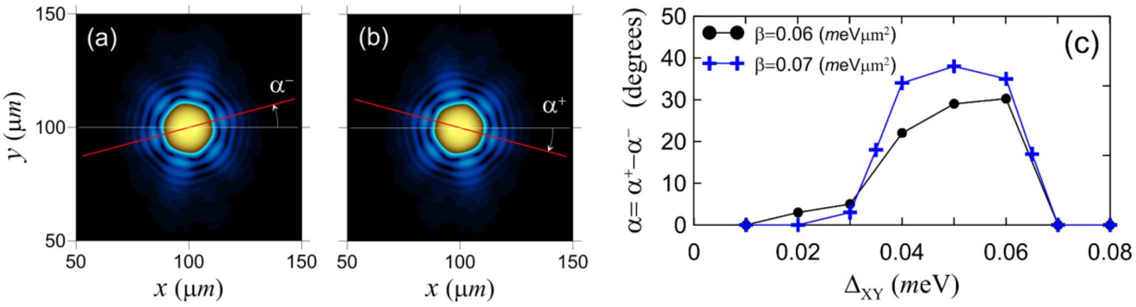

Fig. 3.12 Calculated intensity profiles of the hexagon patterns under (a) left circularly polarized and (b) right circularly polarized pump beam. Parameters are similar to those of Fig. 8 of the main text. (c) Rotation angle $|\alpha^+| + |\alpha^-|$ of the pattern vs. the birefringence parameter Δ_{XY} for two realistic values of the TE-TM splitting.

3.5 Summary and conclusions

In this chapter the spontaneous formation of polygon patterns in a coherently driven dissipative system of polaritons has been reported. The effect of the interplay between parametric instability and bistability on the system dynamics has been investigated. These results present a new and simple paradigm for the creation of patterns with novel geometries in unconfined polariton fluids, which does not rely on the use of pumps with nontrivial geometries or phase, or confinement within heterostructures with multiple dispersions. It has been shown how the onset of parametric instability causes coherent scattering to states carrying orbital angular momentum, leading to spontaneous symmetry-breaking and the emergence of stationary structures. The coherent superposition of a driven pump mode with parametrically unstable signal and idler modes has proven in numerical simulations to be able to reproduce the main behaviours of our system, namely the generation, competition and selection of different patterns similar to those observed in experiment.

A bunching effect at the bistable threshold has also been observed, where the light emitted by the microcavity exhibits super-Poissonian statistics, which can be attributed to the underlying strongly superlinear temporal dynamics of the system. Specifically, it is a nonlinear effect in which the intracavity intensity fluctuations are strongly enhanced by the interplay between the pump-induced bistability and the dynamic “pattern-forming” parametric instability, which provides scattering channels into which particles can scatter and accumulate.

In terms of future directions, there is a vast wealth of potential physics to be explored. Microcavities engineered to feature a large TE-TM splitting are expected to generate patterns with rich polarization properties resulting from an in-plane effective magnetic field and spin-anisotropic interactions [171], whilst also offering the observation of new topological excitations, such as Skyrmions and half-solitons [77]. The presence of polarization multistability [172] remains unexplored in the context of pattern formation. Single shot time-resolved measurements will certainly provide invaluable insight into the pattern formation process. Extreme spatio-temporal statistical fluctuations in the value of the intracavity field known as rogue waves are expected, which may play a key role in the transverse mode dynamics [173] and so far have yet to be explored in polariton systems. Furthermore, such measurements will shed light on the bunching effect measured at the threshold. Squeezing has already been observed at the bistable threshold in a single-mode micropillar [174], but theoretically predicted antibunching amplified by parametric scattering [175] is yet to be observed.

Beyond exciton-polariton systems, ideal candidates for further exploration of spontaneous vortex patterns are nonlinear optical systems such as cavities with photorefractive crystals and atomic vapours [65], where pattern formation relies on a dynamical combination of propagation, nonlinearity, gain and loss as is the case here. Further afield, in condensed matter systems such as superfluids and atomic Bose-Einstein condensates described by a conservative Gross-Pitaevskii equation, the opportunity arises to investigate what exotic patterns may be formed by matter-wave dynamical instabilities in different dimensionalities and trapping geometries [176]. For example, modulational instability leading to the generation of new harmonics was recently reported in an atomic condensate, [177] but it remains to be seen whether components carrying high order vorticity can be created during pattern formation [178]. Furthermore, studies of quantum effects in the context of pattern formation such as quantum entanglement, squeezing and spatial correlations are still to be explored, and have potential to be stimulated by the findings reported here.

Chapter 4

Polarization effects in topological dimer chains

4.1 Motivation

The successful application of topological arguments to the energy bands of photonic systems [179] has led to a surge in research activity related to topology over the past decade [180–183]. A few notable examples of photonic systems exhibiting topological effects are shown in Fig. 4.1. The interest lies in the potential for integrated devices offering robust transport of photons. Protection against scattering losses, which are currently a large hindrance when it comes to integrated photonic devices, is provided by additional ordering of the system which can be classified according to a discrete topological invariant. A commonly used example of topological ordering is the *genus* of a 3D object, which corresponds to the total Gaussian curvature integrated over its whole surface, which is always an integer (equivalent to the number of holes). Smooth and continuous deformations of the object change the geometry of the object whilst preserving its genus, unless for example a new hole is created, which corresponds to a topological phase transition. In photonic systems, the Brillouin zone is a 2D surface (equivalent to a torus due to its periodic boundary conditions) over which one may calculate the total phase picked up by a wave function along a closed path to define the *Chern number*, the topological invariant used to describe quantum Hall-type phases. One of the most common approaches to engineering topological phases is to start with a Dirac Hamiltonian such as that of a honeycomb lattice potential which has linearly intersecting bands, and hence point degeneracies, and introduce symmetry-breaking (time or inversion) perturbations which open a non-trivial gap. The signature of the latter feature is the appearance of unidirectional edge states at the interface with a trivial insulator, e.g. vacuum.

Recent advances in semiconductor lithography and nanofabrication techniques have allowed sophisticated tailoring of the potential landscape of microcavity polaritons [189, 190]. Whilst polaritons already offer a unique combination of high mobility, large nonlinearity and ultrafast response times, confining polaritons in lattice potentials allows precise control over the shape and flow of polaritonic wave packets. They are attractive candidates in the realm of topological photonics due to their polarization properties, susceptibility to magnetic fields and appreciable nonlinearity, all of which may be utilized to reach novel polariton phases with non-trivial topological ordering [191–194]. In this chapter, a textbook topological system, a dimerized 1D chain which

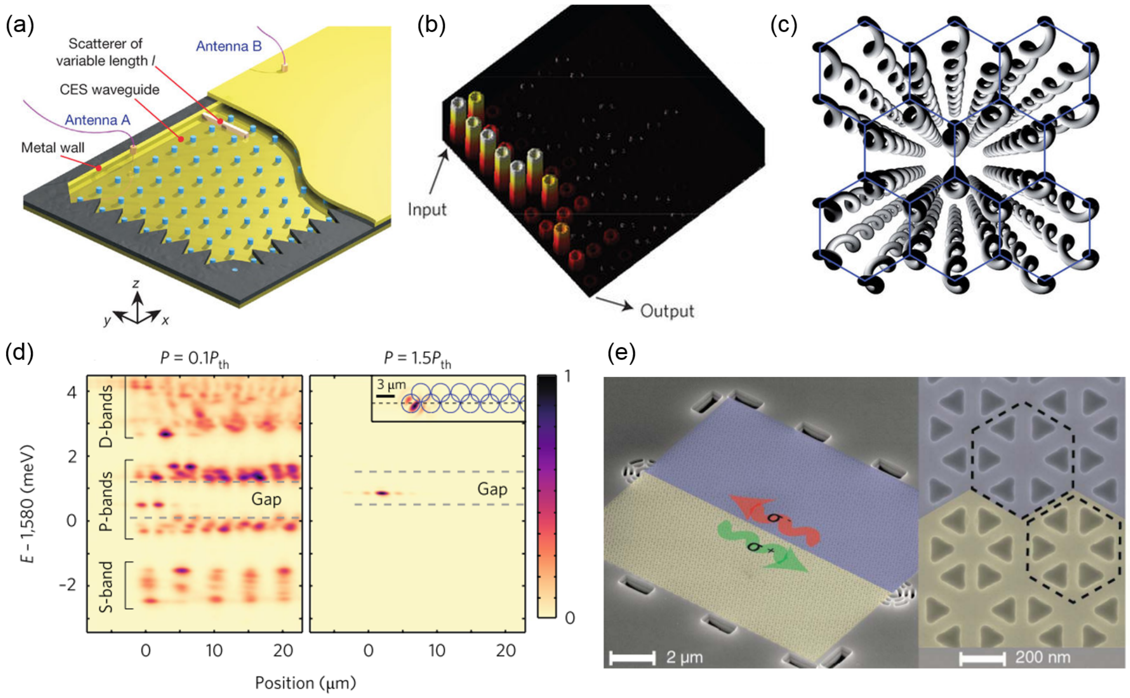

Fig. 4.1 Advances in topological photonics. (a) Schematic of the gyro-magnetic photonic crystal (PhC) slab reported in Ref. [184]. The blue dots indicate the ferrite rods arranged in a 2D square lattice subject to a magnetic field of 0.2 T which explicitly breaks time-reversal symmetry (TRS). Chiral edge states (CESs) are found at the interface between the PhC and metal wall, with two dipole antennas A and B serving as feeds/probes. (b) Experimental propagation of topological edge states around a defect in a lattice of Si-based ring resonators from Ref. [185]. An artificial gauge field is engineered via a hopping phase between resonators, which acts oppositely on clockwise/anti-clockwise resonator modes due to TRS. The two pseudospins behave as two independent quantum Hall systems with equal and opposite Chern number. (c) 2+1 D (two spatial dimensions and one temporal) system of helical waveguides as described in Ref. [186]. Propagation of wave packets along z can be used to simulate temporal evolution and observe CESs in the x, y plane. This so-called Floquet topological insulator has broken z-reversal symmetry due to the waveguide helicity. (d) Polariton lasing in the topological edge state of a 1D chain of micropillars from Ref. [187]. At low pumping powers (left) all modes are incoherently populated whereas above threshold (right) lasing occurs in a state residing in the bulk energy gap, localized at the edge of the chain (inset). (e) Interface between a quantum emitter and topological system from Ref. [188], where the boundary between two PhCs with different topologies (blue and yellow regions) created by deforming honeycomb lattices (see right) supports CESs. Radiative transitions of the quantum dot with opposite spins couple to the CESs defining a topological waveguide.

constitutes a Su-Schrieffer-Heeger (SSH) model [195] for photons, will be studied in detail using spatially- and polarization-resolved PL spectroscopy. Starting from the building block of a single micropillar with a discrete energy spectrum and progressing towards a finite zigzag chain with a topological gapped spectrum, we will consider how photonic spin-orbit coupling (SOC) affects the eigenstates of the system, perturbing both the energies and tunnelling rates of confined states.

4.2 Photonic atoms and dimers

4.2.1 Zero-dimensional cavity

First we will consider a single micropillar as shown in Fig. 4.2. In Fig. 4.2(a) we see a scanning electron microscope image of a typical micropillar. The fabrication process [see Section 2.1] is used to create in this case cylindrical structures patterned into Sample 2 with diameters of 3 μm and etch depths of $\sim$8 μm. The other etched structures mentioned throughout this Chapter, which were all fabricated in the same run on Sample 2, have the same parameters. This is sufficient to induce confinement potentials on the order of 10 meV. In Fig. 4.2(b) we see a schematic of a single pillar, showing the cavity layer sandwiched between vertical DBR stacks along the growth direction. The red layer represents the position of the embedded QWs. Due to the large negative cavity-exciton detuning in Sample 2, the polaritons are highly photonic. In Fig. 4.2(c) we see the fundamental LP resonance of the micropillar. A fitted Lorentzian gives a spectral width of around 85 μeV, corresponding to a Q factor of over 17000. The peak is typically broadened compared to the LP resonance of the unprocessed planar cavity, resulting from extra etching-induced losses. Besides the vertical confinement of photons from the DBRs, the large disparity between the refractive indices of the cavity layer and the surrounding air leads to strong lateral confinement of photons via total internal reflection at the sidewalls. As a result, there is quantization of both the longitudinal and transverse wave vector of photons, so the micropillar is essentially a 0D circular waveguide. This three-dimensional confinement leads to a series of equally spaced peaks in the energy spectrum, as can be seen in Fig. 4.2(d). The three peaks shown correspond to the first three modes of the pillar and are reminiscent of the electronic energy levels of an atom. Hence the micropillar is a “photonic atom”. As we ascend in energy the increasing kinetic energy of polaritons means they are less strongly confined in the potential well of the micropillar, until eventually the kinetic energy is comparable to the barrier height and strong mode confinement no longer occurs.

In Fig. 4.2(e) the normalized transverse profiles of the first two modes are plotted. This corresponds to a cut through the centre of the pillar, whose potential profile is represented in shaded grey. The 1D profiles of the confined modes are proportional to the square of the wave functions and hence the amplitude at a given position determines the probability of finding a particle there. The results strongly resemble the solutions to a paradigmatic example of quantum mechanics, the “particle in a 1D finite potential well” [196]. Inside the pillar we see stationary states with single and double-lobed distributions reflecting the underlying symmetric and anti-symmetric wave functions,

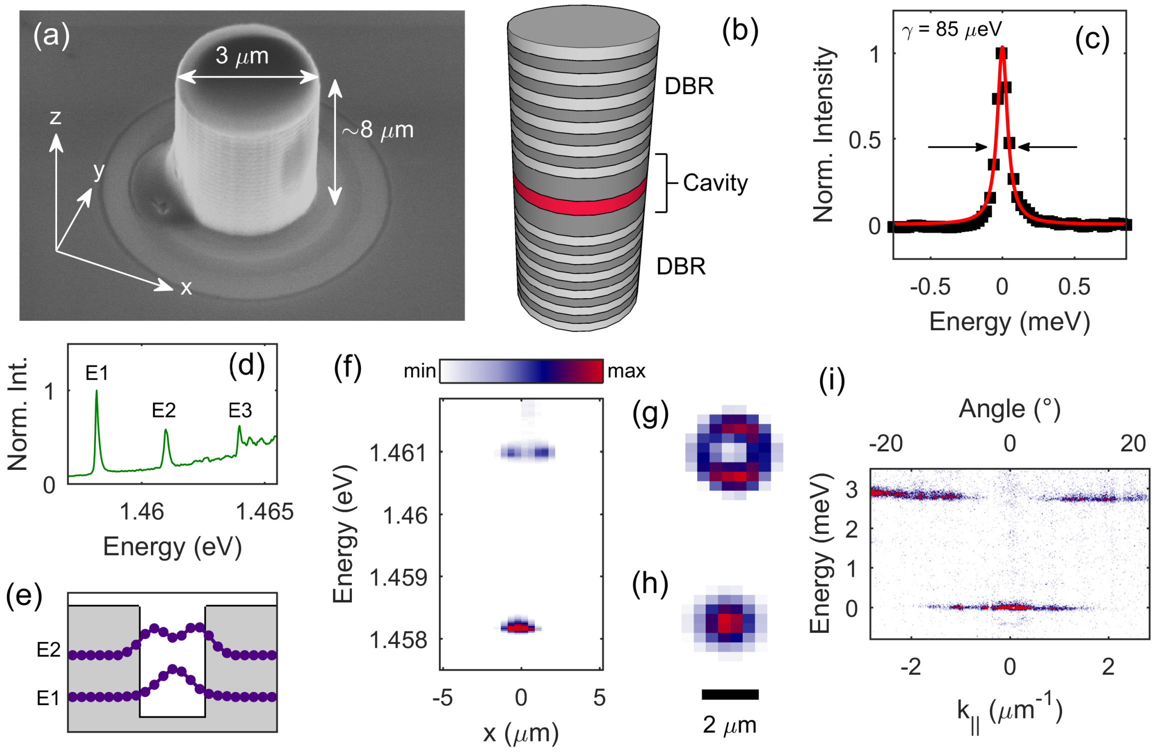

Fig. 4.2 (a) Scanning electron microscope image of a single micropillar cavity labelled with characteristic length scales and with x, y and z directions defined. (b) Schematic of a single micropillar showing the distributed Bragg reflector (DBR) layers and cavity layer. (c) PL spectrum of the fundamental pillar mode with fitted Lorentzian. The x axis represents the energy detuning from the fundamental resonance. (d) PL spectrum showing the first three quantized pillar modes. (e) Transverse profiles of the E1 and E2 modes in real space. (f) Real space PL spectrum (through a cut of the micropillar at $y = 0$). (g) Tomographic real space image of mode at E2 energy. (h) Tomographic real space image of mode at E1 energy. The scale bar at the bottom corresponds to 2 μm. (i) Angle-resolved PL spectrum. All contour plots (and in subsequent figures) use the colour scale shown in (f). Note that the 'min' and 'max' values have been capped so as to enhance the visibility of features.

whilst at the pillar boundaries the intensity exponentially decays into the classically forbidden region. A spatially and spectrally resolved slice of the near field emission through the centre of the micropillar is presented in Fig. 4.2(f), where the different populations (intensities) of the two modes can be seen, reflecting their different photon fractions and thermalization towards the ground state. In order to fully visualize the eigenstates of our system, the PL of the micropillar was scanned across the slit of the spectrometer as described in Section 2.3.3. 2D spatial maps of the E1 and E2 modes are shown in Figs. 4.2(g),(h). The cylindrical geometry of the potential well produces 2D modes described by Bessel functions of the first kind [197], which differs from the case of square pillars [107, 198] or non-planar mirrors [199]. In our case the eigenstates are most appropriately described in a polar coordinate basis using quantum numbers n and m which give the number of nodes in the radial and azimuthal directions respectively. The E1 state has $n = 0$ and $m = 0$ whilst the E2 state has $n = 0$ and $m = 1$. The azimuthal winding of the phase can be clockwise or anti-clockwise for the E2 state, making it doubly degenerate [139]. In principle, if one takes a cut going through the origin of the pillar for any azimuthal angle one should retrieve a 1D profile identical to the one shown in Fig. 4.2(e) due to the axial symmetry of the micropillar. Here it can be seen for the E2 mode that there is a slight variation in intensity in the azimuthal direction. This is a result of imperfections in the confinement potential which preclude the formation of perfectly axially symmetric modes [139, 200]. Finally, in Fig. 4.2(i) we see a central cut of the energy spectrum of the micropillar in momentum space (the far-field profile). We observe that the spectral isolation (Fig. 4.2(f)) and real space localization (Fig. 4.2(g),(h)) of the pillar modes lead to narrow and flat modes with broad angular extension.

When 0D cavities are coupled into an array or extended lattice, the in-plane cylindrical symmetry is broken and a Cartesian coordinate basis becomes more convenient, in which eigenstates are described in the framework of Hermite-Gaussian modes. In this new basis the quantum numbers simply correspond to the number of nodes along x and y directions. The E1 mode has a HG_{00} profile, while the E2 mode can be decomposed into degenerate HG_{10} and HG_{01} modes. As can be seen in Figs. 4.3(c),(d), these two degenerate modes are characterized by a node in the intensity profile along orthogonal dimensions. Thinking of our micropillar as a photonic atom, we see that the wave function of the HG_{00} mode is analogous to an electronic orbital with s-type symmetry, and will henceforth be referred to as a photonic s orbital, whilst the HG_{10} and HG_{01} modes correspond to orbitals with p-type symmetry, featuring a two-lobed "dumbbell" shape, and can be accordingly labelled as p_x and p_y orbitals.

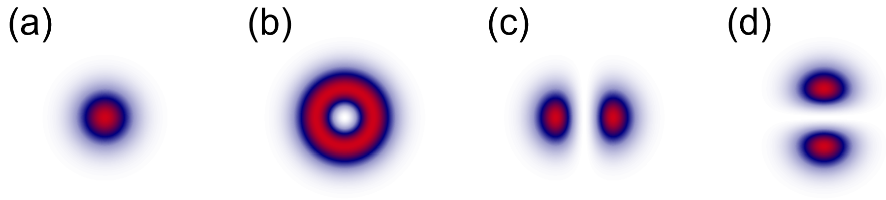

Fig. 4.3 Calculated real space emission of micropillar eigenmodes. (a) The fundamental mode with a cylindrically symmetric Gaussian profile is analogous to an s orbital. (b) The first excited mode has a ring-shaped profile, and can be decomposed into HG_{10} (c) and HG_{01} (d) modes, analogous to p_x and p_y orbitals respectively.

4.2.2 Coupled cavities

Now we shall consider the effect of finite coupling between a pair of 0D cavities. Previously we dealt with an isolated micropillar whose photonic orbitals can be classified in terms of numbers of nodes. When cavities are sufficiently close that wave functions of the confined modes overlap, the finite tunnelling energy between cavities splits the energy of the orbitals into new hybridized orbitals, which represent linear combinations of s and p orbitals and are now classified according to bonding character. The mode structure of these bonded orbitals is determined by the electromagnetic field overlap, where superpositions of orbitals with symmetric and anti-symmetric wave functions are referred to as bonding and anti-bonding modes respectively. The bonding strength can be tuned through the geometry of the micropillars and their centre-to-centre distance [201]. As with the single pillar and the electronic orbitals of an atom, now there is strong analogy with the hybridized electronic orbitals of diatomic molecules in chemistry. In that case, the energy splitting and strength of bonding is determined by Coulomb interactions between electrons [202].

In Fig. 4.4(a) we see a scanning electron microscope image of a photonic diatomic molecule structure. We see that there is spatial overlap of the micropillars since the diameter of the micropillars (3 μm) exceeds the centre-to-centre distance (2.55 μm) which allows evanescent coupling of the photonic fields. A schematic of the molecule comprising two identical cavities labelled as A and B is shown in Fig. 4.4(b). Each pillar induces an approximately harmonic confinement potential and there is finite tunnelling between pillars which is represented by some energy J, which encompasses different terms J_i corresponding to different orbitals [7]. Using this notation a 2×2 Hamiltonian for our photonic molecule (neglecting polarization) can be written as follows:

$$\hat{\mathcal{H}} = \begin{pmatrix} E_i & J_i \\ J_i & E_i \end{pmatrix}, \tag{4.1}$$

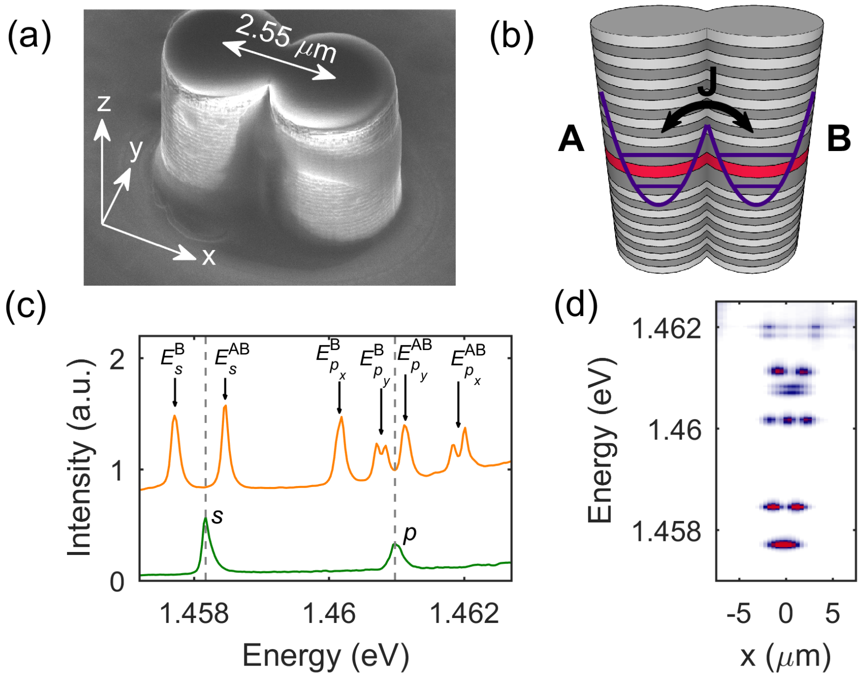

Fig. 4.4 (a) Scanning electron microscope image of a photonic molecule comprising two spatially overlapping micropillars with a centre-to-centre distance of 2.55 μm. (b) Schematic of the photonic molecule overlaid with a sketch of the double potential well experienced by polaritons. (c) PL spectrum of a photonic atom (solid green line) and photonic molecule (solid orange line) labelled with the corresponding bare and hybridized orbitals. (d) Real space PL spectrum (integrated along y) of the photonic molecule.

where E_i is the energy of the i^{th} orbital. For the s orbitals the eigenvalues of this matrix are simply $E_s^{\mathrm{B/AB}} = E_s \mp J_s$ which corresponds to the bonding (E_s^{B}) and anti-bonding (E_s^{AB}) modes. The energy separation between bonding and anti-bonding orbitals is given by twice the tunnelling energies between the bare orbitals. For p orbitals, we can no longer treat the p_x and p_y orbitals on the same footing, since coupling between pillars is along the x direction, so p_x orbitals undergo "head-to-head" σ bonding whilst p_y orbitals undergo "shoulder-to-shoulder" π bonding. These have very different energies due to the different spatial mode overlap, such that the off-diagonal terms in the Hamiltonian become

$$J_p = \begin{pmatrix} J_{p_x} & 0 \\ 0 & J_{p_y} \end{pmatrix}. \tag{4.2}$$

This gives eigenvalues $E_{p_x}^{\mathrm{B/AB}} = E_p \mp J_{p_x}$ and $E_{p_y}^{\mathrm{B/AB}} = E_p \mp J_{p_y}$. Fitting to the experimental data gives values of $J_{p_x} = 0.88$ meV and $J_{p_y} = 0.18$ meV. In principle, there may also be a finite splitting between the bare energies of the p_x and p_y orbitals if the potential well of the pillars does not have perfect cylindrical symmetry, such that $E_{p_x} \neq E_{p_y}$ [139, 200].

In Fig. 4.4(c) we see a comparison of the energy spectrum of a single pillar (corresponding to bare s and p orbitals) and the spectrum of a photonic molecule where orbitals hybridize into new eigenmodes. Fig. 4.4(d) shows an energy-resolved slice of the real space emission along the long axis of the molecule. We see discrete modes characterized by nodes in their intensity, showing a marked thermalization towards the ground state as with the single pillar. For the hybridized p orbitals, the lowermost and uppermost modes have an energy separation approaching 2 meV, corresponding to a tunnelling energy on the order of 1 meV, which is an order of magnitude larger than the linewidth. Yet, there still remains a large gap between s and p modes, so there is no hybridization between orbitals (interatomic matrix elements). Fig. 4.5 shows the real space emission at the energy of the labelled peaks seen in Fig. 4.4(c). The hybridized modes are classified according to bonding character and orbital symmetries. In the case of the photonic s orbitals, we see a merged wave function for the bonding mode, whilst the anti-bonding wave function shows two separated peaks. These reflect the even (zero nodes in intensity) and odd (one node in intensity transverse to molecule) parity of the coupled modes. For the p orbitals, we see four different ways the modes can bond, reflecting the spatial (axial) asymmetry of the underlying p_x and p_y orbitals. Note that there is no tunnelling between orthogonal p orbitals. Taking into account solutions with even and odd parity (bonding and anti-bonding), the dimerization between the degenerate p orbitals of the 0D micropillars leads to four distinct orbitals. In order of energy, these modes correspond to σ bonding, π bonding, π anti-bonding and σ anti-bonding.

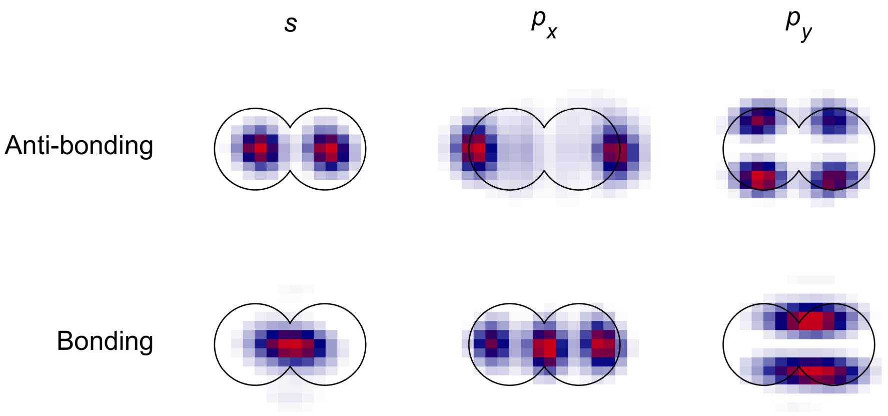

Fig. 4.5 Experimental tomographic real space images of the hybridized modes formed by overlapping confined wave functions in the molecule structure.

In Fig. 4.6 the wave functions of the hybridized modes are approximated by taking linear combinations of the underlying orbitals positioned in cavities A and B. Assuming the two orbitals have the same parity, bonding modes can be constructed by adding their wave functions and anti-bonding modes by subtracting one from the other (equivalent to reversing the parity of one orbital). The contour lines map the electric field profiles of the modes.

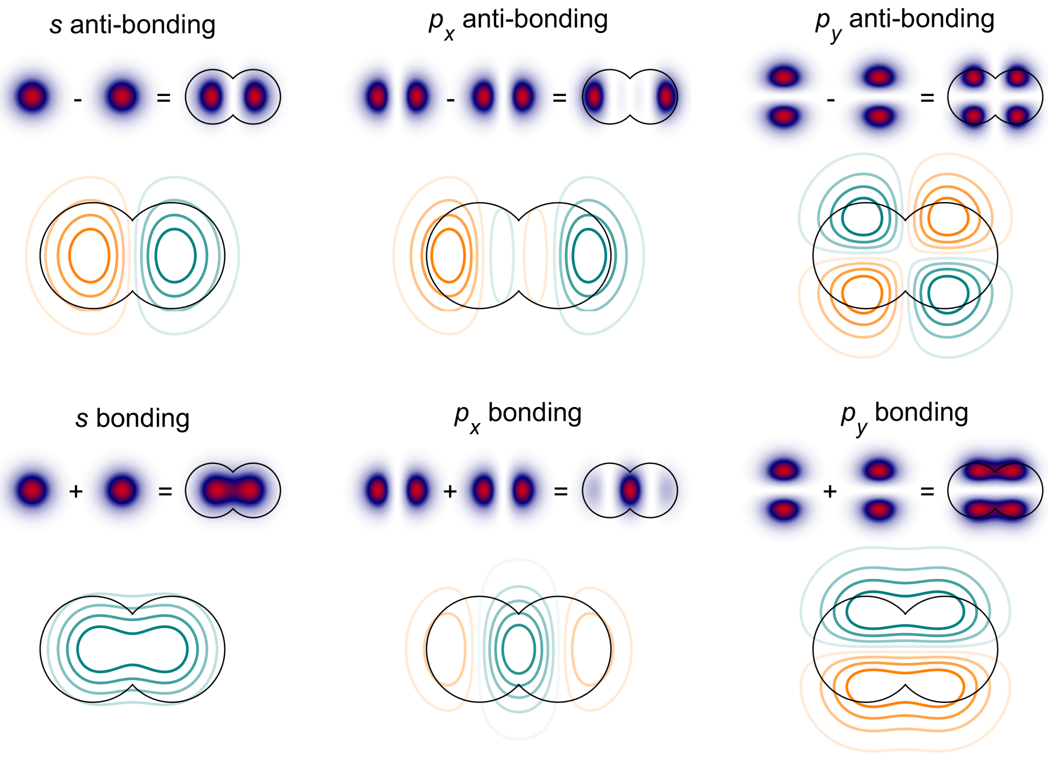

Fig. 4.6 Calculated real space images of the hybridized modes formed by linearly combining orbital wave functions from cavities A and B in the molecule structure. The smaller images correspond to $|E|^2$ whilst the larger contour plots correspond to E.

4.3 Polarization effects

4.3.1 TE-TM splitting

TE-TM splitting has previously been discussed in Section 1.4.2 in the context of planar microcavities where it induces an energy splitting in the 2D polariton dispersion, which scales quadratically with wave vector. The microcavity studied in this chapter features a prominent TE-TM splitting, as can be seen in Fig. 4.7, engineered by creating an offset between the cavity mode and central frequency of the stopband through judicious choice of heterostructure design parameters (see Appendix A). Due to the highly photonic nature of the polaritons studied here, the TE-TM splitting exceeds several hundred μeV at large oblique in-plane angles. In the case of 0D cavities, there is no longer a continuous parabolic dispersion, as polaritons are confined to the previously discussed quantized orbitals. As can be seen in Fig. 4.2(i), the fundamental s orbital is centred at $k = 0$, whilst the p orbital mode comprises finite k vectors (an annulus in Fourier space), meaning that the k^2-dependent TE-TM splitting should be non-zero. Its effect has previously been elucidated by Dufferwiel *et. al.* [203] where it was shown that the spin angular momentum s (left or right circular polarization of the electric field) and orbital angular momentum l (azimuthal winding of the phase due to non-planar wave fronts) degrees of freedom become coupled by TE-TM splitting. A similar effect was also explored in a photonic analogue of a benzene molecule consisting of six coupled micropillars in a ring [109]. In both cases, the eigenmodes of the system in the presence of TE-TM splitting are described by their total angular momentum $J = l + s$ since spin and orbital angular momentum quantum numbers s and l are no longer conserved.

Let us now consider the two degenerate $l = 1$ modes of the 0D cavity introduced in Section 4.2.1, where the single clockwise/anti-clockwise winding of the phase was described. Including spin (polarization), we can then construct four possible states, corresponding to either co- or counter-rotating spin and orbital angular momenta. These new eigenmodes have $J = 0, \pm 2$ and have been described in polariton systems as spin vortices (SVs) due to the fact that the linear polarization angle winds around the core of the mode (in other photonic contexts such modes are referred to as vector vortex beams [204–206]). They are also expected to be separated in energy, hence inducing an *on-site* perturbation to the Hamiltonian describing confined polaritons in coupled 0D lattice sites [see diagonal terms in Eq. 4.1]. Note that using a linear polarization basis rather than a SV basis also introduces non-diagonal terms.

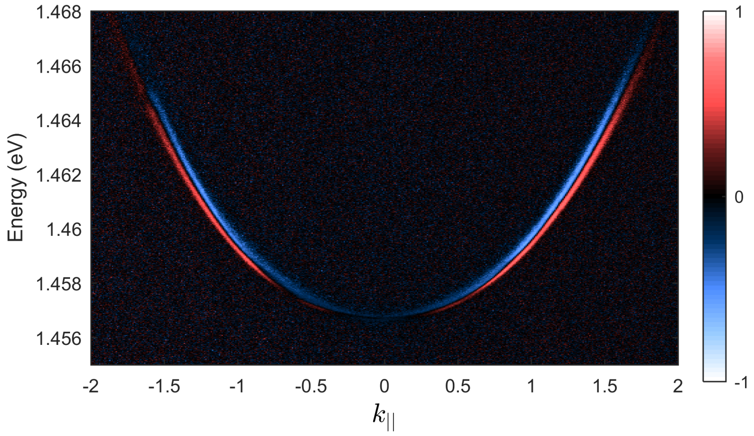

Fig. 4.7 Stokes linear polarization parameter S_1 of a typical angle-resolved PL spectrum in a planar unetched region of the sample. The TE-TM splitting induces a pronounced splitting of the lower polariton branch.

Polarization-resolved measurements were performed on a single micropillar like the one studied in Section 4.2.1 (with a slightly more negative detuning due to it being at a different sample position[1]) allowing the Stokes parameters S_1 and S_2 to be constructed. S_1 characterizes the polarization state in the horizontal/vertical (H/V) basis while S_2 corresponds to diagonal/anti-diagonal (D/A), with both being required to fully describe the linear polarization state of a photonic mode. Measurements in the

---

[1] There is a minimal change in the effective mass of particles since $|C|^2$ approaches 1 at such large negative detunings.

pure circular polarization basis (S_3) were not performed since all polarization effects are in-plane. In Fig. 4.8(a) the total intensity of the PL emission (sum of all four polarizations) is plotted. The lower energy peak corresponds to the $l = 0$ s orbital which does not experience any *on-site* polarization perturbation, and the higher peak corresponds to the $l = 1$ p orbital. As we see in Fig. 4.8(b), the latter peak is actually a triplet, which can be fitted by Lorentzians of similar widths ($\sim$ 90-100 μeV). The middle peak corresponds to the $J = \pm 2$ spin anti-vortices and is the brightest due to this double degeneracy. The peaks either side belong to the $J = 0$ SVs. Their population disparity may be ascribed to different radiative losses [19]. Real space polarization-resolved images at the energies of the spin-orbit coupled eigenmodes are shown (in descending energy) in Figs. 4.8(c)-(e). The arrows depict the orientation of the linear polarization detection angle, and at the far right we see the total emission intensity. The upper and lower rows correspond to the radial and azimuthal SVs seen at the high and low energy peaks in Fig. 4.8(b) respectively. In both cases a clear rotation of the measured intensity distribution follows a rotation of the in-plane polarization detection axis. In contrast, the mode(s) measured in Fig. 4.8(d) show little to no variation in the emission pattern with detection polarization. Although each of the two underlying spin anti-vortices has their own distinctive polarization texture (which may be observed under certain circumstances [203]), their degeneracy means no net polarization structure is generally observed. Whilst the total intensities of the modes show approximately ring-shaped profiles as expected [203], the slightly elliptical nature of the confinement potential is evidenced by the double lobe structure visible in e.g. the lower energy mode in Fig. 4.8(e) [200].

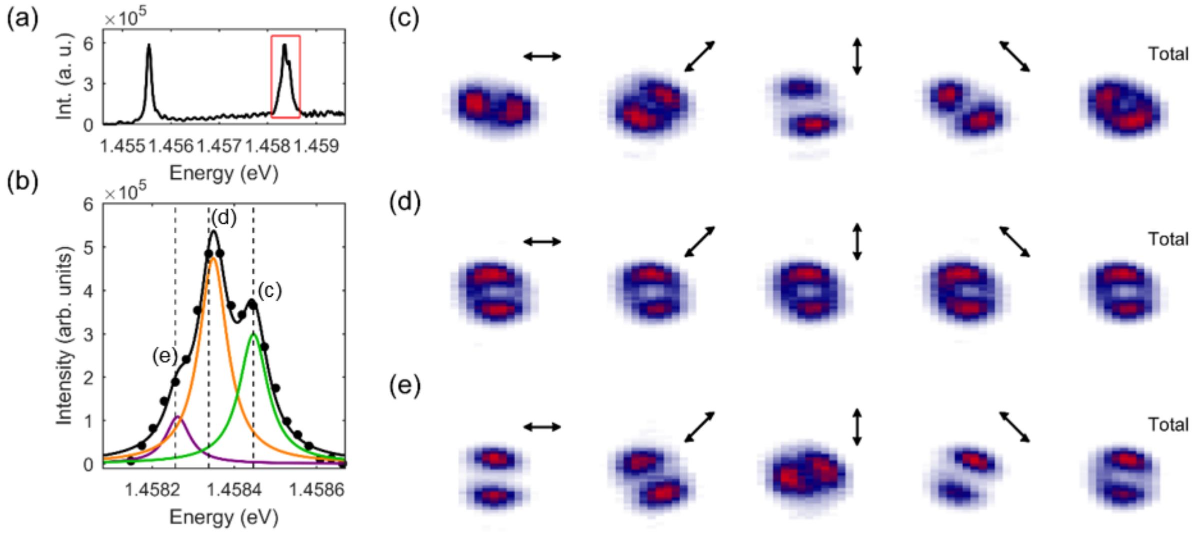

Fig. 4.8 (a) PL spectrum of a single micropillar showing the s and p orbital peaks. (b) Close-up of the p orbital peak corresponding to the red box in (a) showing a fit to the data (solid black line) with three underlying Lorentzian peaks (coloured lines). The vertical dashed black lines lie roughly at the peak energies, and correspond from right to left to the real space images shown in (c)-(e). (c) The higher energy $J = 0$ mode, which is a radial SV. (d) The zero-energy $J = \pm 2$ modes (separately orthogonal hyperbolic spin anti-vortices) whose combination results in no net polarization. (e) The lower energy $J = 0$ mode, which is an azimuthal SV.

In Figs. 4.9 and 4.10 we explore further the polarization structure of the different p modes, comparing experimental and calculated results. Figs. 4.9(a),(b),(g),(h) show the measured intensity difference of the emission in orthogonal polarization bases. In contrast to the Stokes parameters, the differential intensities shown here are not normalized to the total intensities of modes, in order to visualize the polarization structure only in regions with large signal. Figs. 4.9(a),(b) and (g),(h) show the differential intensities in the H/V and D/A bases respectively, given by $I_H - I_V$ and $I_D - I_A$, where the upper row corresponds to the radial SV and the lower row the azimuthal SV. In both cases, clearly orthogonal p orbitals couple to orthogonal polarizations (e.g. p_x is H polarized and p_y V polarized in Fig. 4.9(a)). The spatially varying polarization texture of the modes can be visualized by calculating for each pixel the linear polarization angle defined as $\Psi = 0.5 \cdot \arctan(S_2/S_1)$. The lines in Figs. 4.8(c) and (i) are oriented at this angle, which winds from $-\pi/2$ to $\pi/2$ with H and V polarizations being found at angles of 0 and π respectively. In the higher energy mode the polarization generally points outwards, i.e. radially, and in the lower energy mode it points tangentially to this direction, i.e. azimuthally. These results can be compared with calculated SV modes representing linear combinations of Hermite-Gaussian modes with their intensity nodes oriented at different angles. There is good qualitative agreement between the experimentally measured and theoretically calculated mode profiles, confirming that the measured eigenmodes of a single pillar are not far from ideal SVs.

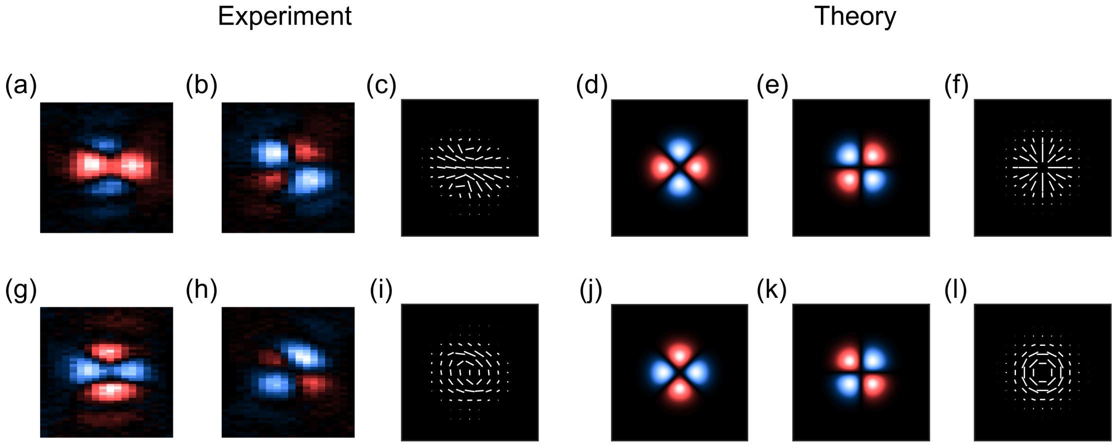

Fig. 4.9 Experimental and theoretical SV modes. Intensity difference of the radial SV in the H/V basis (a),(d) and D/A basis (b),(e). (c) and (f) are traces of the real space linear polarization angle convolved with the intensity. Intensity difference of the azimuthal SV in the H/V basis (g),(h) and D/A basis (h),(k). (i) and (l) are traces of the real space linear polarization angle convolved with the intensity.

In Fig. 4.10 the linear polarization angle is plotted against position along a path of fixed radius which encircles the core of the mode (the spatial coordinate is given by the real space azimuthal angle $\theta = \arctan(y/x)$). A clear double winding of the linear polarization angle accompanies a full revolution about the centre of the modes, analogous to the pure phase winding of conventional vortex beams. Again we see good agreement between experiment and theory. Finally, it should be noted that the discrepencies between experiment and theory in Figs. 4.9 and 4.10 are consistent with the previously mentioned ellipticity of the confinement potential which also affects the observed intensity distribution [203]. Specifically, it can be seen that there is a slight preference towards a certain polarization angle in the pillars which both distorts the patterns shown in Figs. 4.9(c),(i) and bends the stripes plotted in Figs. 4.10(a),(b).

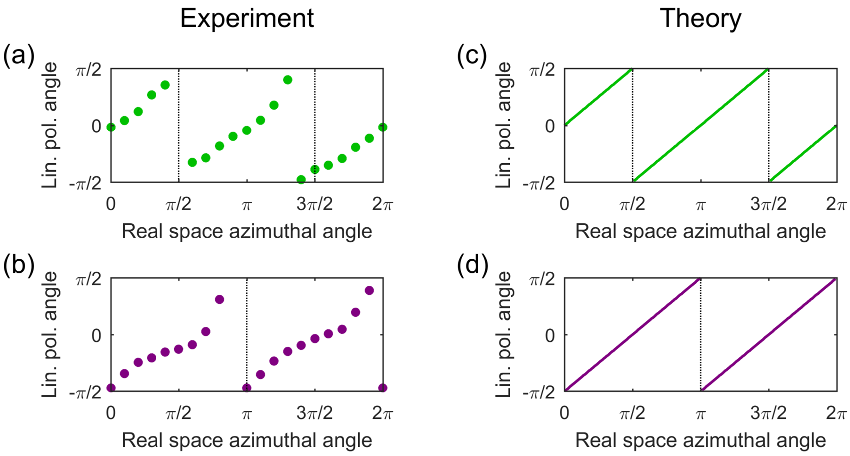

Fig. 4.10 Visualization of the double polarization winding of the SV modes. The upper row corresponds to the experimental (a) and theoretical (b) radial SV and the lower row to the experimental (c) and theoretical (d) lower energy azimuthal SV.

4.3.2 Polarization-dependent tunnelling

Besides the on-site polarization splitting which occurs in single micropillars with sizeable TE-TM splitting as we have just described, polarization effects also act on photons as they hop between cavities due to different effective masses (governed by TE-TM splitting) and lateral boundary conditions (governed by the geometry of the structure). This polarization-dependent tunnelling has been explored experimentally [109] and appears to have fascinating theoretical implications [207, 191, 74]. Here we consider the single photonic molecule, or dimer, shown in Fig. 4.4(a) and measure the influence of this effect directly by measuring the PL spectrum in H and V polarization bases. These two linear polarizations have an electric field orientation which lies longitudinally and transversely to the tunnelling direction (along x) respectively. In Fig. 4.11 polarization-resolved spectra of the s and p modes of a single dimer are presented. As previously mentioned, bare s orbitals experience no on-site polarization splitting in the presence of TE-TM splitting, due to their zero orbital angular momentum. Therefore, the polarization splitting observed in the hybridized modes in Fig. 4.11(a) arises entirely due to polarization-dependent tunnelling. As expected, the energy gap between the bonding and anti-bonding peaks is larger for H polarization, reflecting the larger tunnelling energy since it is longitudinal to the tunnelling direction. Below the spectrum, we see real space images of the modes which exhibit high degrees of linear polarization. In Fig. 4.11(d) the spectrum of bonded p orbitals is shown. In this case, in addition to the polarization-dependent tunnelling, there is also the on-site TE-TM splitting term which further contributes to polarization splitting of the four modes.

The lowest and highest energy doublets appear to arise largely from hybridization of p_x orbitals. From polarization-dependent tunnelling alone we would expect the very lowest and highest energy peaks to have H polarization. However, the on-site TE-TM splitting term pushes H polarized p_x orbitals (radial SV) up in energy and V polarized p_x orbitals (azimuthal SV) down. The result is an asymmetry of the spectrum, where both hybridized p_x orbitals have the same sign of polarization splitting. The inner two doublets arise from hybridization of p_y orbitals. The polarization-dependent tunnelling has the same effect as for the p_x orbitals. However, now the TE-TM splitting has opposite sign such that V polarization gets pushed up in energy and H polarization down. Once again this gives rise to a polarization asymmetry in the spectrum.

Revisiting the Hamiltonian of a photonic molecule for p orbitals

$$\hat{\mathcal{H}}_p = \begin{pmatrix} E_p & J_p \\ J_p & E_p \end{pmatrix}, \tag{4.3}$$

the TE-TM splitting can be included as a perturbation to diagonal and off-diagonal matrix elements using the basis states $\left|p_x^H\right\rangle, \left|p_x^V\right\rangle, \left|p_y^H\right\rangle, \left|p_y^V\right\rangle$, such that

$$E_p = \frac{1}{2}\begin{pmatrix} \Delta E_{\mathrm{SOC}} & 0 & 0 & \Delta E_{\mathrm{SOC}} \\ 0 & -\Delta E_{\mathrm{SOC}} & \Delta E_{\mathrm{SOC}} & 0 \\ 0 & \Delta E_{\mathrm{SOC}} & -\Delta E_{\mathrm{SOC}} & 0 \\ \Delta E_{\mathrm{SOC}} & 0 & 0 & \Delta E_{\mathrm{SOC}} \end{pmatrix}, \tag{4.4}$$

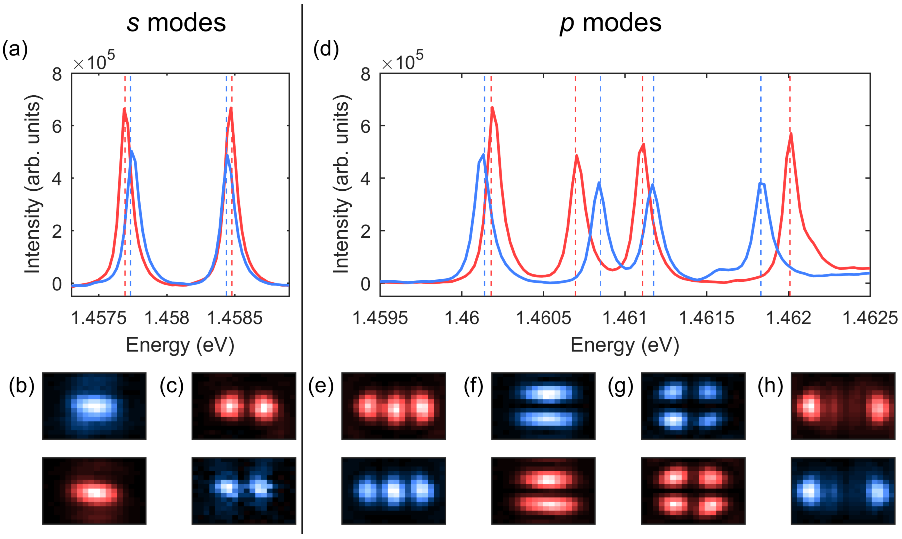

Fig. 4.11 Effect of polarization-dependent tunnelling. (a) Spectrum of the s modes of a single dimer resolved in H (red) and V (blue) polarizations which are longitudinal and transverse to the tunnelling direction respectively. (b) Real space images of bonding modes formed from s orbitals. (c) Real space images of anti-bonding modes formed from s orbitals. The images are ordered vertically according to their energies, which are indicated by dashed vertical lines in (a). (d) Spectrum of the p modes of a single dimer resolved in polarization. A baseline has been removed from the spectra. (e) Real space images of bonding modes formed from p_x orbitals. (f) Real space images of bonding modes formed from p_y orbitals. (g) Real space images of anti-bonding modes formed from p_y orbitals. (h) Real space images of anti-bonding modes formed from p_x orbitals. The images are ordered vertically according to their energies, which are indicated by dashed vertical lines in (d).

where ΔE_{SOC} represents the total energy splitting of p orbitals induced by TE-TM splitting, and the off-diagonal terms reflect the fact that the eigenvectors of the Hamiltonian are in fact SVs rather than uncoupled p_x and p_y orbitals. This basis was chosen rather than a circular polarization basis since it allows for easier evaluation of the matrix elements needed to determine the perturbed eigenmodes of $\hat{\mathcal{H}}_p$. Polarization-dependent tunnelling can be introduced as a perturbation to the off-diagonal (hopping) matrix elements in Eq. 4.3 such that

$$J_p = \begin{pmatrix} J_{p_x} + \delta J_{p_x}/2 & 0 & 0 & J_m \\ 0 & J_{p_x} - \delta J_{p_x}/2 & J_m & 0 \\ 0 & J_m & -(J_{p_y} + \delta J_{p_y}/2) & 0 \\ J_m & 0 & 0 & -(J_{p_y} - \delta J_{p_y}/2) \end{pmatrix}, \qquad (4.5)$$

where δJ_{p_x} and δJ_{p_y} give the total energy splitting induced by polarization-dependent tunnelling for p_x and p_y orbitals and J_m is a term that mixes orbitals in the same SV manifold. By starting with the values for J_{p_x} and J_{p_y} extracted earlier, the full Hamiltonian for the p orbital spin-orbit coupled dimer was solved numerically, giving values of: $\Delta E_{\mathrm{SOC}} = 110$ μeV, $\delta J_{p_x} = 50$ μeV, $\delta J_{p_y} = 30$ μeV and $J_m = 115$ μeV, which provide a good fit to the experimental data and polarization-dependent tunnelling energies consistent with extracted values in coupled micropillars from other works [201, 109].

Now we have considered the confinement of polaritons in 0D cavities, photonic coupling between two cavities, and the separate and combined effects of TE-TM splitting and polarization-dependent tunnelling on their energy spectra. The p orbitals of a single pair of cavities form a photonic spin-orbit coupled dimer. An interesting next step is to use this as a building block to construct something more complex and explore the polarization degree of freedom.

4.4 Topological dimer chains

4.4.1 Edge states

A textbook example of topological physics is the so-called SSH model which admits 0D topological edge modes [208]. It was recently shown in Ref. [187] that the p orbitals of polariton micropillar lattices realize a two-fold "orbital" version of the SSH chain, featuring an exponentially localized mid-gap state in one of the p orbital subspaces of the form

$$\Psi_n \propto (t/t')^n, \tag{4.6}$$

where n denotes the unit cell counted from the edge, and t and t' denote two hopping amplitudes (within and between unit cells respectively). The size of the gap containing the edge states is given by

$$\Delta = 2|t - t'|. \tag{4.7}$$

As previously discussed for the case of a single dimer, the two possible "head-to-head" (σ) and "shoulder-to-shoulder" (π) bonding types of p orbitals feature a large difference in tunnelling energy ($J_\pi \approx 0.2 J_\sigma$ was previously estimated for a dimer with its long axis along x in the last section). One can see from this how a 1D chain of dimers with 90° bond angles implements a variant of the classic SSH model, since the hopping energy alternates between strong and weak for one orbital subspace and vice versa for the orthogonal one. In principle, one can realize an SSH model using s orbitals and relying on the dimerization provided by polarization-dependent tunnelling [208]. In our case, for s orbitals we extract a tunnelling energy of $J_s = 0.37$ meV, compared to a polarization splitting of $J_s \sim 30\ \mu$eV, meaning the size of the gap based on Eq. 4.7 is expected to be around 60 μeV, compared to a linewidth $\gamma_s \sim 85\ \mu$eV. Hence from here onwards only p orbitals will be considered.

In order to study the polarization degree of freedom in the SSH chain, 1D arrays of overlapping micropillars forming dimer chains in a zigzag geometry were fabricated [see Fig. 4.12(a)]. In Figs. 4.12(b) and (c) the differential near field profiles of the p orbitals of a single micropillar resolved in D and A polarizations are shown (corresponding to the previous single pillar measurements), since the two orthogonal orbital orientations and two orthogonal linear polarizations form the four basis states of our SSH chain. Each zigzag chain thus constitutes four coexistent SSH models for photons.

In Fig. 4.12(d) the main hopping processes for p orbitals in the zigzag chains are shown schematically. The thick and thin solid lines represent strong and weak bonding respectively, and the colours of the bonds represent coupling of polarization to tunnelling direction as verified in the last section. Note that for convenience x and y directions are defined to be at a 45° angle with respect to the laboratory frame. Figs. 4.12(e) and (f) show the possible dimerization states of a zigzag chain with 10 sites, for the separate p_x and p_y subspaces and two orthogonal polarizations. It can be seen that when strong bonding occurs along the x direction, all sites in the chain couple to form dimers (represented by ovals). This dimerization leads to a gapped spectrum, which

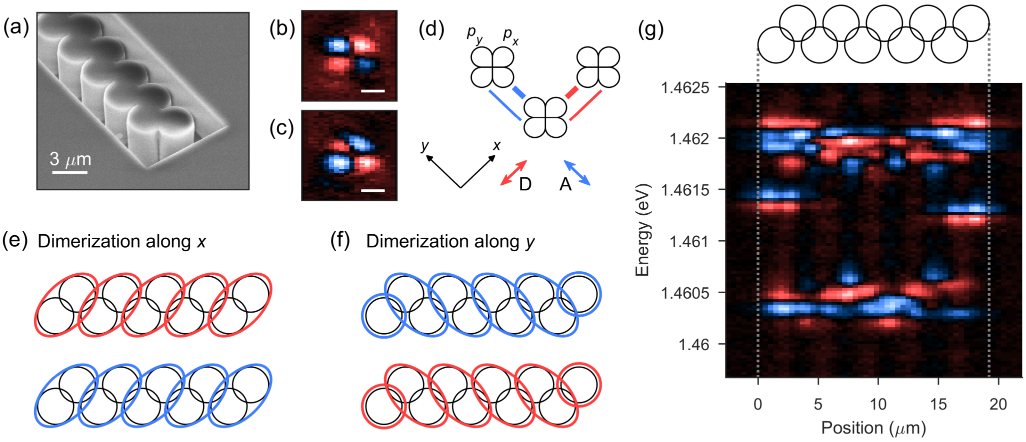

Fig. 4.12 (a) Scanning electron microscope image of a typical zigzag chain of coupled micropillars. (b),(c) Real space images of the confined $l = 1$ mode of a single micropillar, perturbed in the presence of TE-TM splitting to form radial (b) and azimuthal (c) spin-vortices. The colour contrast represents the intensity difference in D (red) and A (blue) polarization bases [see (d)] and the white scale bar corresponds to 2 μm. (d) Schematic of p orbital tunnelling processes, with strong and weak bonding represented by thick and thin lines respectively. Note that there is only bonding between like orbitals. The coordinate basis and D and A polarizations are defined underneath. (e) Dimerization states of an $N = 10$ chain where p_x orbitals are strongly bonded, with no resulting edge states. The two different polarizations have a different energy due to TE-TM splitting. (f) Alternative dimerization states of an $N = 10$ chain where p_y orbitals are strongly bonded. The leftmost and rightmost sites are weakly bonded to the rest of the chain, hosting 0D topological edge states. Note that the polarization splitting has opposite sign. (g) Experimental differential PL spectrum (spatially integrated along transverse direction) against longitudinal position for an $N = 10$ chain.

has the topology of a trivial insulator. However, when strong bonding occurs along the y direction, the pillars at the left and right edges couple only weakly to the rest of the chain. In the spectrum of eigenstates, states localized at the left and right edges exist at zero energy (they are non-bonding states) which closes the energy gap and changes the topology of the band structure, making it distinct from the trivial case of (e)[2]. Fig. 4.12(g) shows the experimentally measured differential near field spectrum of a 10 site

---

[2] Formally, the different topologies can be quantified via the Zak phase [209], where the topologically trivial and non-trivial cases have a difference of π.

chain. Within the chain (delimited by vertical dashed lines) we see two bands of states extended across the whole lattice and separated by a large energy gap. Within the gap, we see polarization doublets at the left and right edges. Their topological nature is immediately evident by the fact they are spectrally isolated and do not penetrate into the bulk. One may also observe that edge states at the left are higher in energy than those at the right. This results from an energy gradient along the long axis of the chain[3]. For the sake of clarity, we henceforth analyze the left and right sides of our chains separately.

4.4.2 Odd chains

In chains where the number of sites N is odd, an extra site at the boundary of the lattice exists. Now, the system configurations associated with strong bonding (dimerization) along x and y directions have different topological properties compared to the $N = 10$ (even) case previously discussed. In Figs. 4.13(a) and (b) the two types of dimerization states for an $N = 11$ chain are shown schematically. We see immediately that in contrast to the even case both dimerization states present non-bonding edge states. Since the two configurations are formed from p_x and p_y orbitals respectively, both subspaces are now topologically non-trivial, featuring exponentially localized edge states at opposite sides of the chain. Furthermore, the TE-TM splitting couples orthogonal p orbitals to orthogonal linear polarizations, meaning that the left and right

---

[3] Since it exceeds that expected to arise simply from the cavity wedge, there is most likely additional strain introduced by etching.

edge states in odd chains feature opposite signs of polarization splitting, unlike the even case.

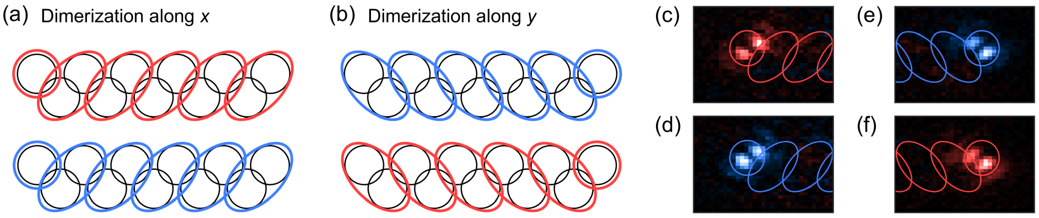

Fig. 4.13 $N = 11$ zigzag chain. (a) Dimerization states along x for D (upper) and A (lower) polarizations. There are topological states in the p_x subspace at the left edge. (b) Dimerization states along y for D (lower) and A (upper) polarizations. There are topological states in the p_y subspace at the right edge. (c),(d) Real space images of the left side of the chain corresponding to the dimerization states shown in (a). (e),(f) Real space images of the right side of the chain corresponding to the dimerization states shown in (b).

4.4.3 Polarization-dependent tunnelling

Previously the subtle interplay of polarization effects was investigated in a single dimer. We have already seen how in the zigzag chain the TE-TM splitting acts as an on-site perturbation, lifting the degeneracy between D and A polarized p_x and p_y orbitals, as seen in the edge states in Fig. 4.12(g) and confirmed by their corresponding spectra in Figs. 4.14(a),(e). The question that then naturally arises is if and how the polarization dependence to the tunnelling energy affects the orbital SSH chain, and to what extent this influence can be observed experimentally. In principle, the J and δJ terms extracted in the single dimer case are the same in the zigzag chain and so give a good idea of the tunnelling rates for the two polarizations. The disparity between the two polarizations is expected to affect the penetration of the edge state into the rest of the chain via Eq. 4.6. One way to delineate its effect is then to consider the profile of the spatial wave functions of the edge states.

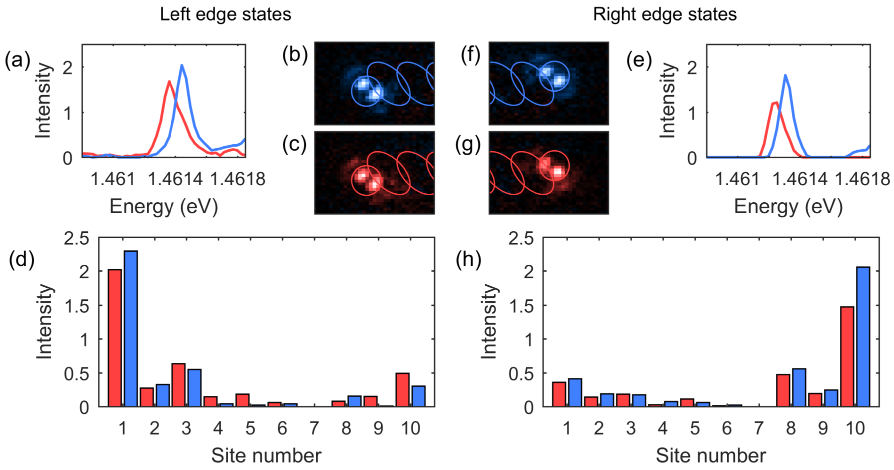

Fig. 4.14 Experimentally measured left (a)–(d) and right (e)–(h) edge states for an $N = 10$ chain. (a) Spectrum of midgap states at left edge in D (red) and A (blue) polarizations. (b),(c) Real space images of the left side of the chain at the energies of the edge states shown in (a). (d) Intensity against site number for the two polarizations. (e) Spectrum of midgap states at right edge in D (red) and A (blue) polarizations. (f),(g) Real space images of the right side of the chain at the energies of the edge states shown in (e). (h) Intensity against site number for the two polarizations.

The effect of the polarization-dependent tunnelling term is demonstrated in Figs. 4.14(d) and (h) which show the intensity against site number at the edge state energies extracted by applying a binning technique to the experimental data. According to Eq. 4.6 the intensity is expected to drop exponentially with the *unit cell* number (every other site) with a decay length proportional to the ratio of strong and weak hopping energies. In experiment, it can be difficult to reliably extract the true decay length since beyond the first two unit cells the intensity becomes very small and comparable to noise. However, it is instructive to compare the intensities of the first and second unit cells at the edges of the chain, i.e. $|\Psi_0|^2/|\Psi_1|^2$, to give an indication of the rate at which the wave function is decaying. For both sides of the 10-site chain sketched in Fig. 4.12 this quantity is smaller for D polarization than A polarization. Considering the left side of the chain as an example, one can see that this result is expected since the connection between the state on the first pillar with the rest of the chain is along the x direction to which D (A) polarization is parallel (perpendicular). As a rough measure of the different decays for the two polarizations, one may then take the ratio of $|\Psi_0|^2/|\Psi_1|^2$ (which is proportional to the inverse localization length) for the two polarizations, defining a new quantity

$$\xi = \frac{|\Psi_0^{\parallel}|^2/|\Psi_1^{\parallel}|^2}{|\Psi_0^{\perp}|^2/|\Psi_1^{\perp}|^2}, \tag{4.8}$$

where $\parallel$ and $\perp$ denote the polarization which can be parallel or perpendicular to the link. Using the values of strong and weak bonding of p orbitals extracted from a single dimer (0.88 meV and 0.18 meV respectively) and polarization-dependent corrections to these terms (50 μeV and 30 μeV respectively) we can estimate a ballpark theoretical figure yielding $\xi^{\text{theory}} = 0.80$. Physically this tells us that the *inverse* localization length should be shorter for parallel polarization, i.e. the edge state penetrates more into the rest of the chain when its polarization is parallel to the tunnelling link.

To test this experimentally, two values of ξ (one for each edge) have been calculated for three different chains [see Fig. 4.15] using the same binning technique used to evaluate the site intensities in Figs. 4.14(d) and (h). Remarkably, despite the crudity of this approach, all values are <1 and lie between 0.68 and 0.89, providing an averaged

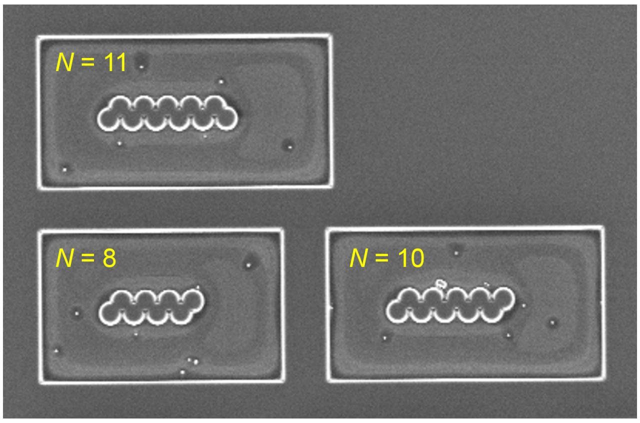

Fig. 4.15 SEM image corresponding to the $N = 8$, 10 and 11 chains studied.

experimental value of $\xi^{\mathrm{exp.}} = 0.78 \pm 0.07$. Of course, caution must be taken, since the quoted error is the standard deviation of the ξ values, whose individual errors are not taken into account. Nevertheless, the results strongly suggest that polarization-dependent tunnelling leads to different localization lengths for the two polarizations.

4.5 Summary and conclusions

To conclude, we have used spatially- and polarization-resolved spectroscopy to study different 1D arrays of micropillars in the single-particle (low-density) limit. We have considered the interplay between different polarization effects in etched lattice environments, beginning with a single pillar, whose eigenstates in the presence of TE-TM splitting become spin vortex modes, progressing to a single dimer, which shows a polarization dependence to the rate of hopping between cavities due to the interplay between various diagonal and off-diagonal perturbations to the Hamiltonian, and eventually reaching a 1D topological chain of dimers where we observe not just an energy splitting of the topological edge modes but a significant disparity in the rate at which orthogonally-polarized wave functions decay. Importantly, this result shows the potential for engineering strong artificial gauge fields for photons in topological systems using the polarization degree of freedom.

Chapter 5

Spatial, spectral and pseudospin properties of a two-dimensional Lieb lattice

5.1 Introduction

Arrays of etched micropillars were introduced in the last chapter, and the spectrum of eigenstates of the zigzag chains may be treated with a simple tight-binding (TB) Hamiltonian similar to that describing 1D polymer chains. In this chapter we will consider 2D arrays of micropillars whose photonic energy bands have strong analogy with the electronic energy bands of real world 2D (or quasi-2D) materials. This exciting avenue of research began with pioneering papers showing that the π and π^* bands of graphene arising from hybridization of the out-of-plane p_z orbitals could be emulated by the photonic bands arising from hybridization of the fundamental s modes of micropillars in a honeycomb lattice geometry [106, 114]. Owing to the large Kerr nonlinearity, the authors also demonstrated non-equilibrium condensation in nonlinear defect states [210] which form at the top of the π^* band and move into the forbidden energy gap under high-power incoherent excitation. Another fascinating feature is the higher energy $l = 1$ bands with p-type symmetry, where the bulk energy spectrum shows both Dirac cones and flat bands, and both flat and dispersive states are found at the edges [115]. Such observations mean polaritonic lattices have attracted keen interest as a versatile platform to study fundamental physical effects of solid state materials in a nonlinear photonic environment, reaching regimes which may otherwise be inaccessible [189]. The emulation of complex many-body phenomena is facilitated by the high degree of control over polariton trapping potentials and the ability to form bosonic macroscopically coherent phases such as condensates and superfluids [27, 50]. Even more appealing is the ease with which polaritons can be loaded into lattice potentials, and the direct access to the spatial wave functions, all available via standard optical techniques.

The main focus of this chapter will be a 2D Lieb lattice [211] (line-centered square lattice), a crystal structure found in nature in high-T_c cuprates and Perovskites [212]. The band structure of the Lieb lattice has celebrated topological properties arising from the arrangement of its three-site unit cell which induces a geometric phase cancellation effect: the destructive interference of linear eigenmodes associated with the different sublattices leads to non-dispersive (flat) energy bands [213]. There are also Dirac cones in the spectrum which have interesting topology in their own right. Lieb lattice modes have been realized experimentally in various different systems [see Fig. 5.1]. A 1D analogue of a Lieb lattice (Stub lattice) was studied in Ref. [111], where the localization properties of a flat-band polariton condensate were studied, with measured effects being attributed to the photonic potential disorder in the fabricated structure.

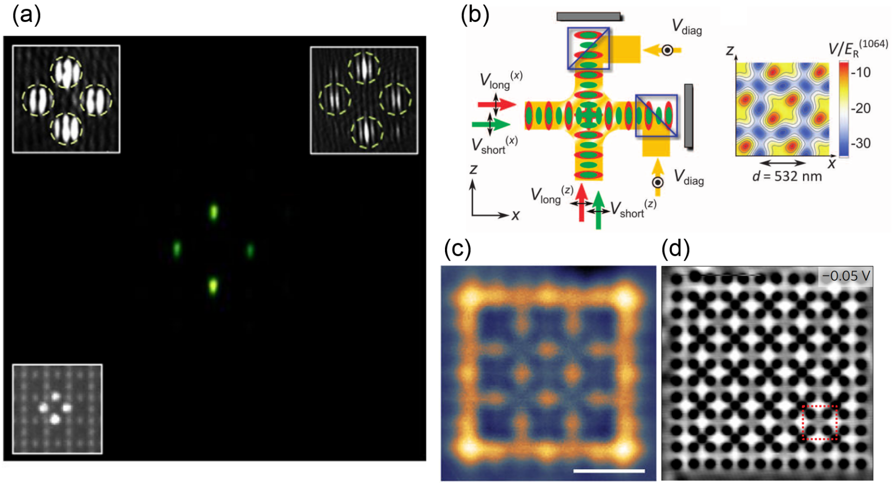

Fig. 5.1 Experimental realizations of Lieb lattices in different systems. (a) A non-diffracting Lieb lattice flat-band state in a coupled waveguide array in fused silica. The top left (right) inset shows an interferogram of the input (output) beam revealing π phase shifts between spots. The lower left inset shows the intensity of the input beam. Taken from Ref. [214]. (b) Engineering an optical Lieb lattice for ultracold atoms by interfering multiple laser beams (left) to create a periodic potential (right) from Ref. [215]. (c) Flat-band density of states in a vacancy lattice in a chlorine monolayer revealed by scanning tunnelling spectroscopy in Ref. [216]. (d) Differential conductance map at the flat band energy in an electronic Lieb lattice formed by CO molecules on a Cu(111) surface from Ref. [217].

Here we will start by studying the linear properties of the 2D Lieb lattice using low-power non-resonant excitation as in the last chapter, followed by regimes of high-power quasi-resonant excitation where optical nonlinearities lead to renormalization of the band structure, non-equilibrium condensation into s- and p-type flat bands and fragmentation of the condensate energies. Finally we consider the polarization degree of freedom, and show that photonic spin-orbit coupling (SOC) generates pseudospin textures in the flat band emission. Many of the main results can be found in Ref. [218].

5.2 Linear regime

5.2.1 Band structure

Firstly we will consider a 2D Lieb lattice of micropillars in the same sample studied in Chapter 4. A scanning electron microscope image of the full microstructure is shown in Fig. 5.2. As discussed in the previous chapter, microstructures in this particular sample have been etched to a depth of $\sim$8 μm, and it can be seen that the micropillars feature highly vertical sidewalls. The small structures that can be seen surrounding the lattice arise from "micromasking", wherein masking material gets randomly redeposited onto areas of the sample meant for uniform etching. Nevertheless, the high quality of the etching (leading to deep confinement) and large negative cavity-exciton detuning mean this sample is highly favourable for studying the band structure of the Lieb lattice. Henceforth we will refer to this sample as the "photonic" sample, and the less negatively-detuned sample (Sample 3) where high-power experiments were performed will be known as the "excitonic sample", which features smaller etch depths of around $\sim$2.5 μm [218].

In Fig. 5.3 an angle-resolved PL spectrum of the photonic sample showing the s- and p-type energy bands is presented, which was measured under low-power non-resonant

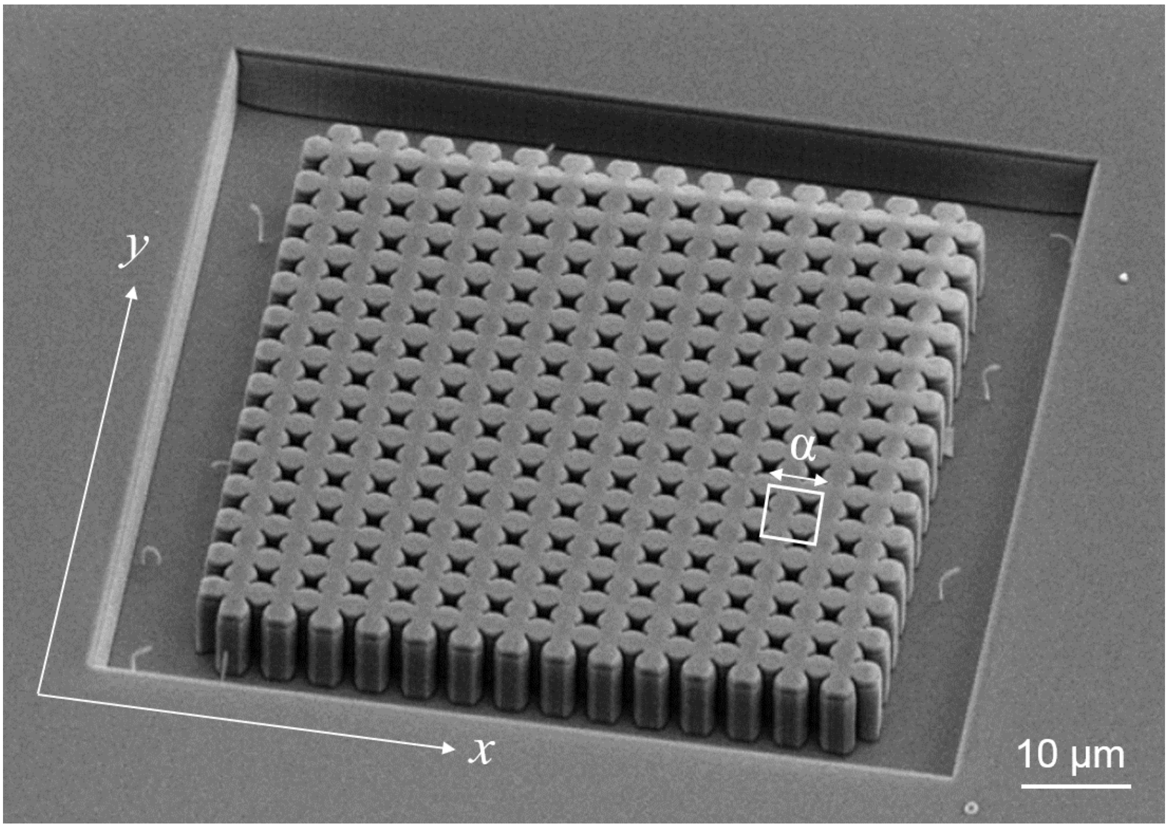

Fig. 5.2 Scanning electron microscope image of a fully etched 2D Lieb lattice. The etch depth is approximately 8 μm and the lattice constant α is 5.1 μm, the width of one unit cell (white box).

excitation. Since there is no energy renormalization in this low-density regime, the measurements reveal the "single-particle" band structure of the lattice. First, one may note the inhomogeneity of the emission intensity; for example, of the s bands only the lowest energy band appears to be visible within the first Brillouin zone (BZ). This may be attributed to a combination of far-field destructive interference and varying lifetimes of different modes [218]. Otherwise, in both the s and p modes we see bands which are dispersive, with both positive and negative curvatures (effective masses), and bands which are approximately non-dispersive, implying infinite effective mass. These flat bands are shown by dashed green lines. The origin of the flat bands is the destructive interference between the probability amplitudes of particle tunnelling processes in the unit cell (A to B and C to B) which leads to zero net flow of particles to B sites. Thus, a macroscopic number of momentum eigenstates become degenerate, and the energy band is flat. This phase cancellation is purely geometric in origin, owing to the three-site unit cell of the Lieb lattice. In reality, there is also finite coupling beyond nearest neighbour sites, which has two effects: (i) it breaks the particle-hole symmetry, such that the dispersive bonding and anti-bonding bands are asymmetric about "zero" energy (the flat bands), and (ii) it adds a small k-dependence (waviness) to the energy of flat bands [219].

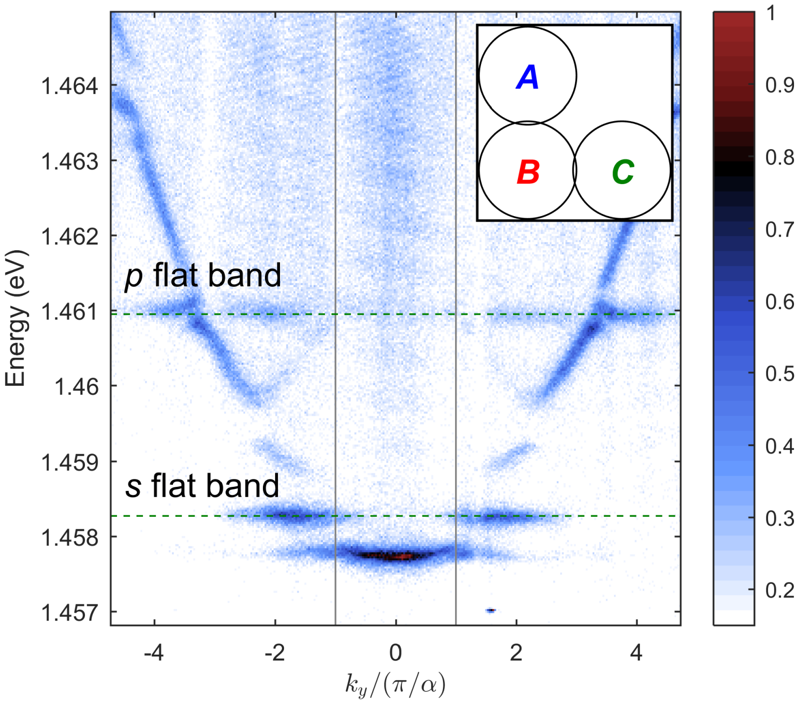

Fig. 5.3 Band structure of the fully etched (photonic) sample at $k_x = 0$. The green dashed lines show the position of the flat bands. The solid grey vertical lines are the boundaries of the first Brillouin zone. The inset shows a schematic of a single unit cell labelled with A, B and C sublattices.

Single-particle measurements were also taken in the excitonic Lieb lattice sample. In contrast to the photonic sample, this structure is only partially etched down to 4–6 layers in the top DBR, such that the active layer of the microcavity remains intact in the bulk of the lattice [218]. This helps to prevent etching-induced broadening of the exciton resonance (due to surface recombination) which is expected to be more prominent in this sample because of the smaller cavity-exciton detuning. Band structures at three different values of k_x are shown in Fig. 5.4, with calculated TB curves plotted on top for reference. The TB model developed [218] does not include the effects of polarization or coupling beyond nearest neighbours, but provides good qualitative agreement with the observed bands as can be seen.

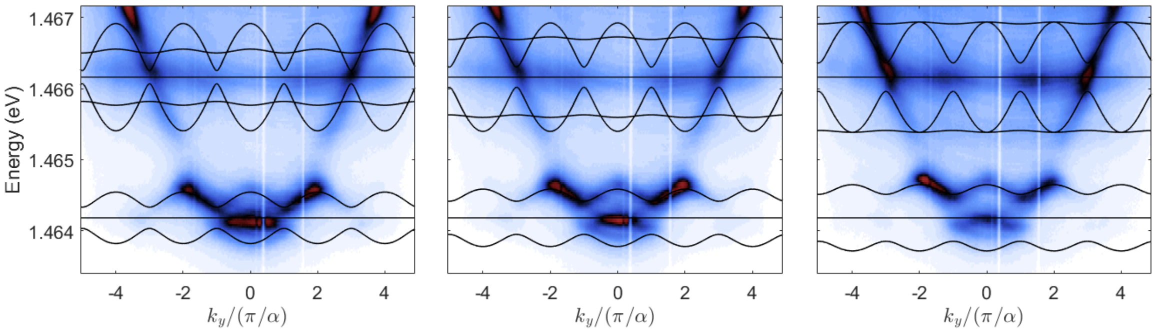

Fig. 5.4 Band structures of the partially etched (excitonic) sample at $k_x = 1.3$, 1.5 and 2 (left to right). In this sample the lattice constant $\alpha = 5.8$ μm.

In Fig. 5.5 the real space emission of the partially etched Lieb lattice is shown at three energies. The images are constructed using the optical tomography procedure described in Ref. [139]. In Figs. 5.5(a),(c) we see the real space emission of the s- and p-type flat bands. Within a single unit cell (white boxes) it can be seen that the intensity is almost entirely distributed on the A and C sublattices, with little to no population on the B sublattice. This gives rise to a distinctive diamond-shaped intensity pattern for the flat band eigenmodes, as highlighted by the dashed green lines. As previously mentioned, there is (ideally) zero net flow of particles to B sites in flat bands, which is reflected here in the high degree of localization on A and C. For comparison, the real space emission at the top of the s anti-bonding (AB) band is shown in Fig. 5.5(b). This corresponds to the maxima of the highest energy s band, at approximately 1.4645 eV in Fig. 5.4. Unlike the flat bands, emission can be seen on all three sublattices, which reflects the fact that the particles are delocalized as is normally the case for the linear eigenmodes of 2D lattices.

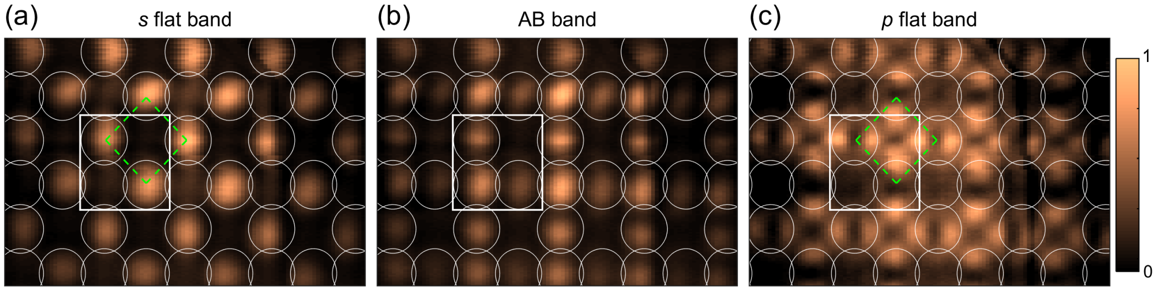

Fig. 5.5 Real space emission at the energies of the s flat band (a), anti-bonding band (b) and p flat band (c). The white box delimits a single unit cell.

It is interesting to note the arrangement of p_x and p_y orbitals in the p flat band seen in Fig. 5.5, where clearly p_x orbitals are predominantly occupied on A sites and p_y orbitals on C sites. Intuitively, this offset in the populations of orbitals on different sublattices creates a necessary imbalance to allow destructive wave interference and flat band formation, given the fact that the hopping of p orbitals is highly directionally-dependent. For example, p_x orbitals tunnel much more easily from C to B (along x) than A to B (along y), so the population of p_x orbitals on A sites must be increased for the net propagation to be zero; the opposite holds for p_y orbitals. The real space intensity patterns of p-type lattice modes have also been studied in photonic graphene [106, 115].

5.2.2 Polarization properties

The polarization degree of freedom in micropillar lattices adds rich physics and is expected to play an important role in the engineering of topological phases [191, 220] and emulation of spinor phenomena in solid state systems [221]. The refractive index step induced by the small physical size of etched microcavities, which is on a scale comparable to the cavity photon wavelength, enhances so-called spin-orbit coupling of light [74]. In addition, as previously discussed in earlier chapters, the polarization-dependent reflection phase experienced by photons at oblique angles (TE-TM splitting) is also present in microcavity systems, which can be tuned by structure design and further increases polarization splitting. It has previously been shown in a hexagonal ring of coupled micropillars that such polarization terms can lead to non-trivial pseudospin textures [109].

In Fig. 5.6 we see Fourier space images from the photonic sample at the energy of the s flat band showing the total emission and a corresponding polarization map (Stokes parameters S_0 and S_1 respectively). The dashed green lines show the boundaries of the second BZ, and it can be seen that the flat band emission resides predominantly at its four vertices. In the polarization map it is evident that the polarization winds around these points, which creates an in-plane gauge field for photons [207]. In the next section we will study the polarization properties of the emission in the high-density regime in the excitonic sample. It should be noted that whilst the reported polarization effects can also be observed in the linear regime in that sample, the narrowing of the lattice modes in energy above the condensation threshold allows enhancement of the polarization effects.

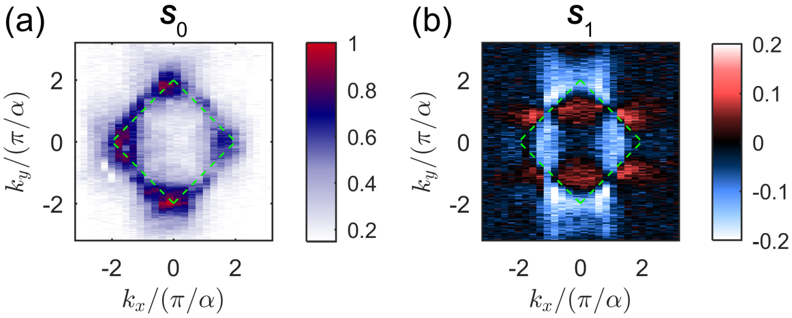

Fig. 5.6 Total intensity (S_0, left) and rectilinear polarization map (S_1, right) of the s flat band emission in k space.

5.3 Nonlinear regime

5.3.1 High-angle excitation

High-angle coherent excitation has previously been employed in both planar [85] and acoustically-modulated [222] microcavities to induce optical parametric oscillation (OPO). It allows efficient direct scattering to low energy/k "signal" states (with a corresponding high energy/k "idler" state) provided phase-matching conditions are met: $2k_{\text{Pump}} = k_{\text{Signal}} + k_{\text{Idler}}$. In order to enter an OPO regime in the Lieb lattice system the excitation was taken to an angle of approximately 20° from the optical axis, as represented schematically in Fig. 5.7, roughly at the lattice wave vector

$(k_x, k_y) = (-4\pi/\alpha, 0)$. The pump energy was around 1.4685 eV, detuned by roughly 0.5 meV with respect to the polaritonic state at that wave vector, and -2.5 meV from the bare exciton energy. The spectrally-resolved k space PL emission was recorded on the CCD.

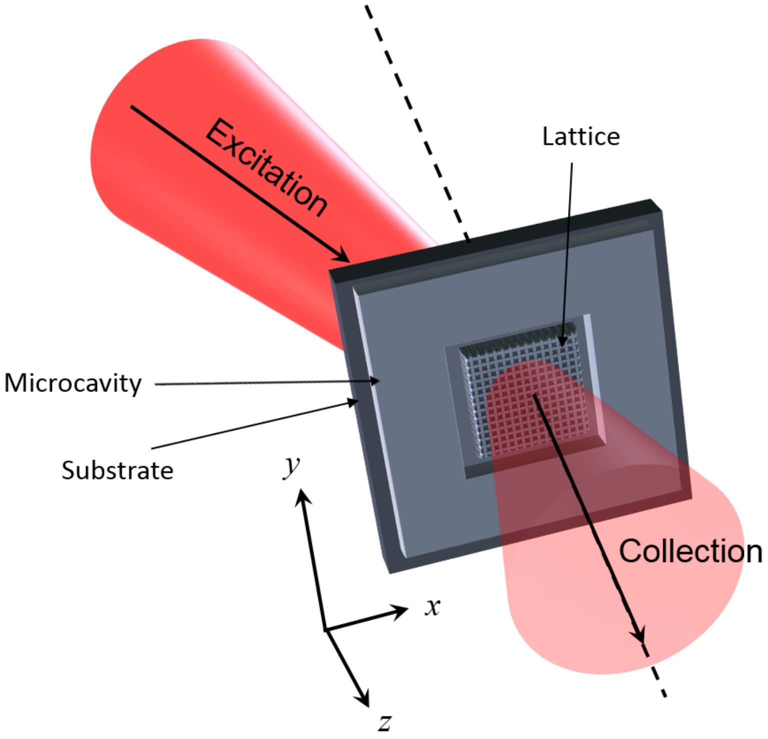

Fig. 5.7 Schematic of the OPO experiment with the Lieb lattice.

In Fig. 5.8 we see the power dependence of the Lieb lattice emission. For this particular measurement, the pump was spectrally filtered to allow analysis of the states at lower energy. The total intensity of these states against excitation power P is plotted in Fig. 5.8(a), where clear threshold behaviour can be seen. In Fig. 5.8(b) the intensity is broken down into the three states which are predominantly populated. It can be seen that at low powers the p flat band dominates the emission spectrum, with an intensity increasing linearly with power. Relaxation to these states occurs via polariton-phonon scattering. The fact that polaritons accumulate in the p states and the s states are only weakly populated suggests that the p flat band presents a significant bottleneck in the dispersion, perhaps due to the enhanced lifetime [19]. Even in this linear regime, self-interactions in the pump mode renormalize the lattice energy spectrum as the excitation power increases, changing both real and imaginary eigenvalue components [90]. OPO behaviour switches on when the complex eigenvalue (where the imaginary component describes losses) of a signal mode becomes real-valued, meaning there is net gain [7]. At a time-averaged power of approximately 47 mW, the threshold power P_{th} for the OPO regime is reached as the pumped polariton states blueshift into resonance with the excitation laser, creating high particle densities favouring efficient polariton-polariton scattering. At this power the total intensity starts to increase superlinearly [Fig. 5.8(a)], which coincides with the appearance of the gap state whose population also jumps rapidly, whilst the p flat band population starts to plateau [Fig. 5.8(b)]. Such behaviour is caused by the interplay between polariton-phonon, polariton-exciton and polariton-polariton scattering. Note that no idler is registered in our experiment due to its high angle and exciton content. As the excitation power is taken further beyond the threshold power, the s flat band population starts to increase nonlinearly [Fig.5.8(b)]. Simultaneously, depopulation of the p flat band occurs. This suggests the opening up of a scattering or relaxation channel which allows the s flat band to populate on faster timescales than the p flat band. Note that thermally-induced phonon channels probably also play a role in polariton relaxation as the sample irradiance increases. Indeed, at the highest excitation powers sample heating started to induce a small redshift of the energy bands.

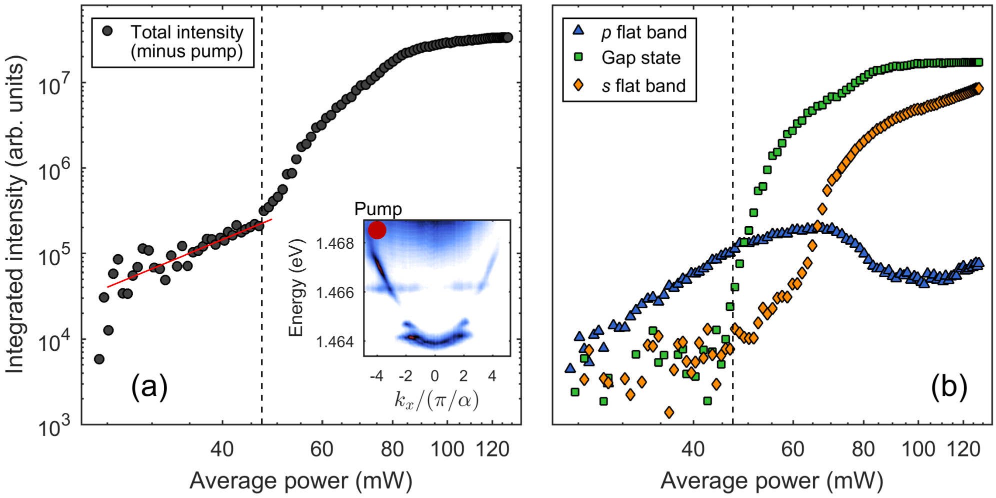

Fig. 5.8 (a) Power dependence of the total emission intensity at energies below the pump. The inset shows a schematic of the pumping scheme, where the laser is blue-detuned with respect to the state at $k_x/(\pi/\alpha) = -4$. (b) Power dependence of the three highly populated lattice modes.

The nonlinear gap state at $k_y/(\pi/\alpha) = -2$ is presented in Fig. 5.9 where the emission is shown at threshold. Such modes are nonlinear defect states which are highly favoured in lattice potentials owing to the negative effective mass of certain states, which makes the product of the repulsive interaction term $\alpha > 0$ and effective mass $m < 0$ negative [210, 7]. This allows the formation of excited states bound to the reservoir potential of the pump, which has been explored previously in polaritonic lattices in Refs. [110, 222].

The spectra of the signal states in the Lieb lattice OPO are shown for various excitation powers in Fig. 5.10. We see that well below threshold, only the p flat band is visibly populated, whilst close to threshold the s bands also show intensity peaks.

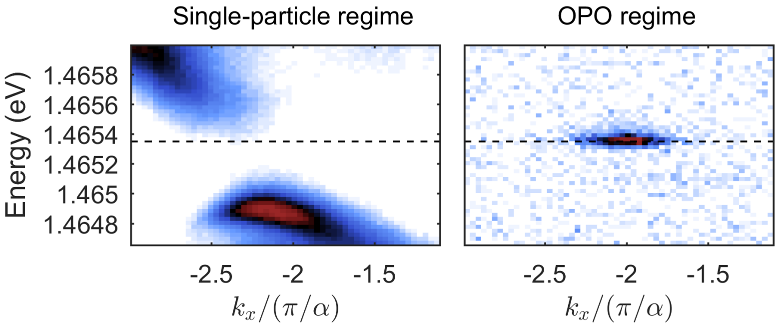

Fig. 5.9 k space emission around $k_x/(\pi/\alpha) = -2$ showing the band gap in the single-particle spectrum (left) and state at the centre of the energy gap in the OPO regime (right).

Just above threshold, the gap state peak dominates the excitation spectrum, and a peak at lower energies attributed to the s flat band can be clearly seen. At even higher excitation powers, one can observe that the s flat band has risen at a faster rate than the gap states. Interestingly, a small energy splitting appears in the gap state, whose origin is unclear.

5.3.2 Normal-incidence excitation

Experiments were also performed with the excitation laser incident normal to the sample surface, as represented in Fig. 5.11, where the results were quite different. This time the laser was detuned to approximately 1.47 eV, around 1 meV below the bare exciton energy, and a horizontally-polarized beam of roughly 20 μm was used to excite about 15 lattice unit cells.

The power dependence can be seen in Fig. 5.12. Threshold behaviour was seen successively in the p flat band, gap states emerging from the s anti-bonding band maxima and the s flat band [Fig. 5.12(a)]. Plotting the full-width at half-maximum

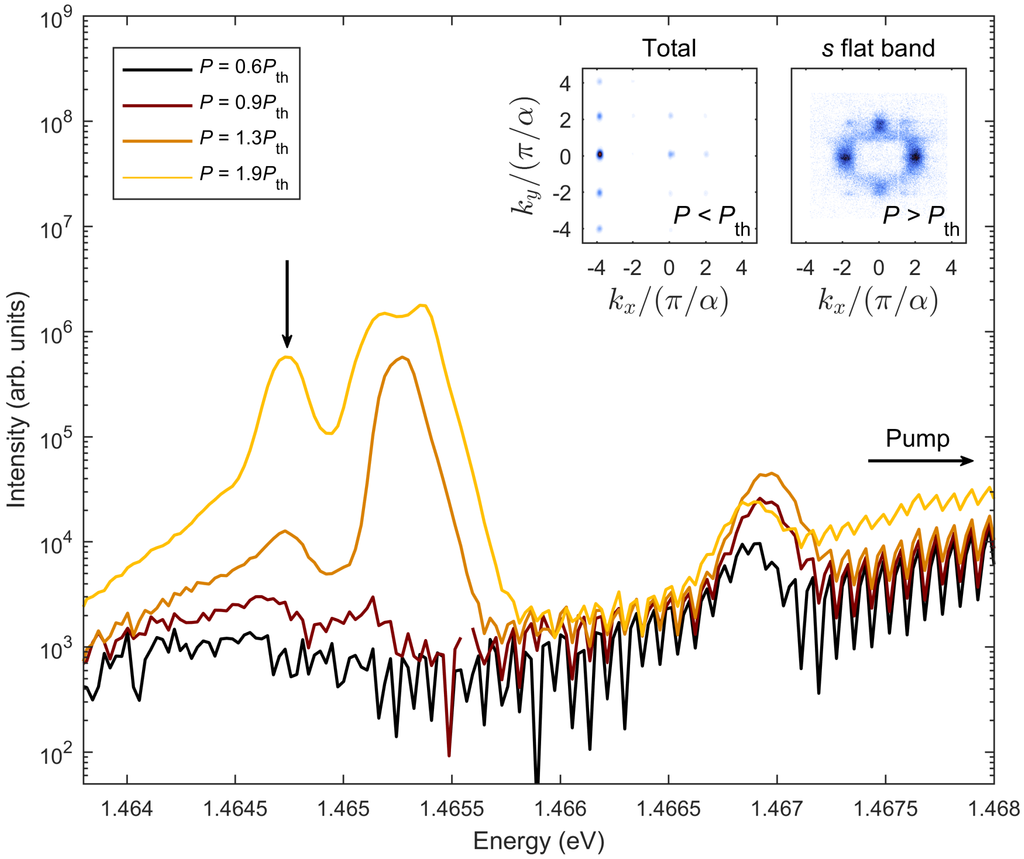

Fig. 5.10 Evolution of the Lieb lattice emission spectrum with excitation power. The pump energy is at a higher energy (horizontal arrow). The two insets show the total k space emission below threshold (left) and the s flat band k space emission above threshold (right), at an energy shown by the vertical arrow in the main panel.

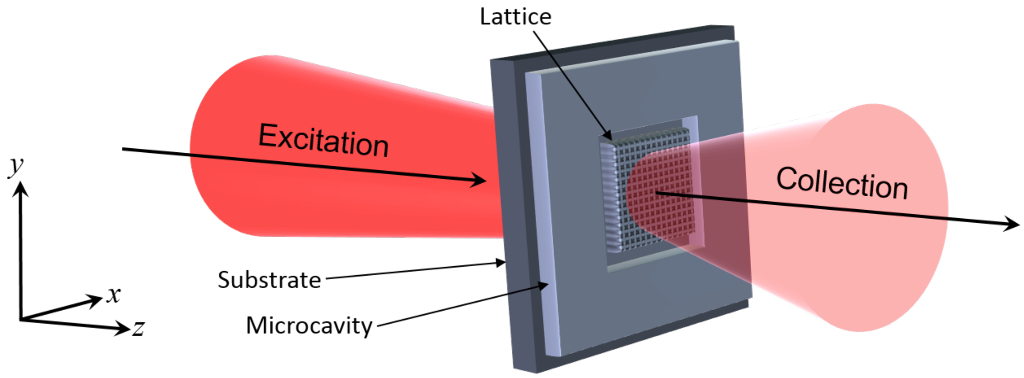

Fig. 5.11 Schematic showing excitation of the Lieb lattice at normal incidence.

(FWHM or linewidth) of the modes shows a sharp drop at the threshold excitation powers. Angle-resolved PL spectra at increasing excitation powers as seen in Figs. 5.12(c)-(g) reveal both the sharp increase of intensity and narrowing in energy of the three lattice modes above threshold. The corresponding real space emission from the condensed modes is shown in Figs. 5.12(h)-(j). As expected, emission from the flat bands shows dark B sites, while the gap states are formed on all three sublattices.

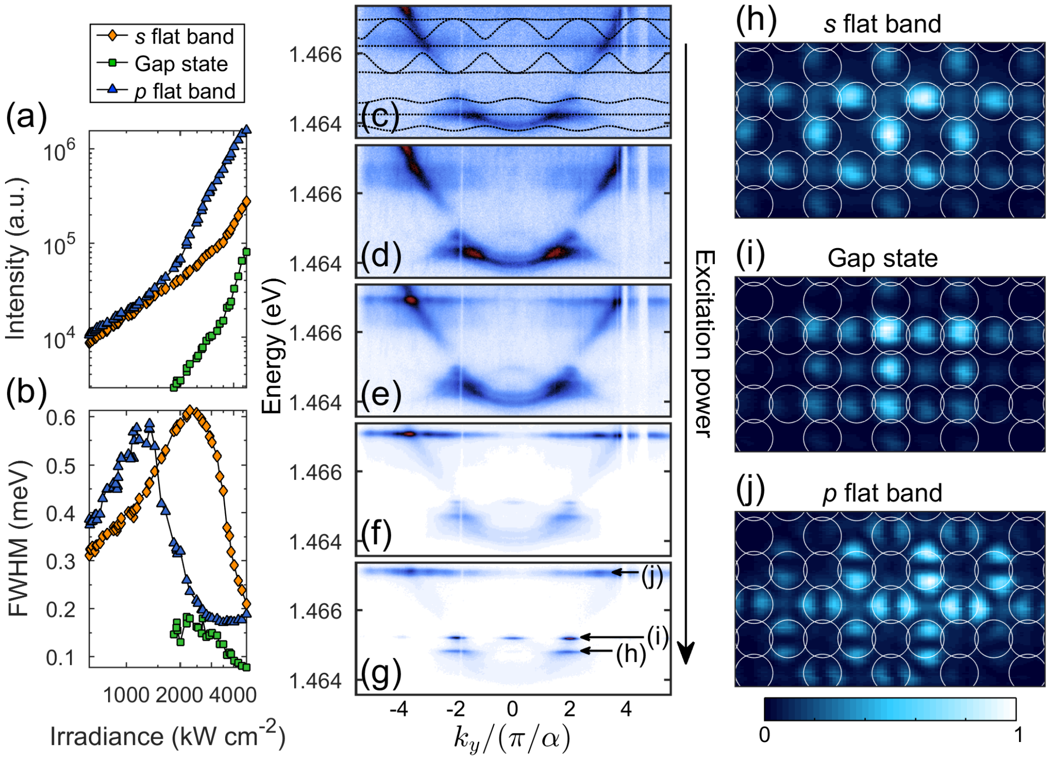

Fig. 5.12 (a) Intensity of lattice modes as a function of excitation power. (b) Full-width at half-maximum (FWHM) of lattice modes as a function of excitation power. (c)-(g) Evolution of the angle-resolved PL emission with excitation power. (h)-(j) Real space images of the lattice condensates.

In the high-density regime above the multiple condensation thresholds, the presence of polariton-polariton and polariton-exciton scattering leads to nonlinear renormalization of the band structure. As previously mentioned, in quasi-flat bands the effective mass of particles tends to infinity, meaning kinetic energy (proportional to the curvature of the bands) is quenched. As a result, flat band particles respond non-perturbatively in the presence of on-site interactions [223]. Under quasi-resonant excitation as is the case here, polariton-polariton and polariton-exciton scattering create a large interaction energy as evidenced by significant blueshift of polaritonic modes. Above threshold, we analyse small regions of the real space emission close to the pump spot and plot the emission energy against lattice site in Fig. 5.13. In the case of the flat bands, significiant energy variation can be seen across the condensates, represented by the artificial colour plot, showing the nonlinear fragmentation in the presence of interactions. In contrast, the nonlinear gap states emit at a constant energy across the lattice. Intuitively, the localization of flat band eigenmodes means interacting macroscopic phases cannot equalize the pump-induced potential energy by propagation to low potential energy regions. In contrast, for the gap states there exists a dynamical balance of nonlinearity and propagation [210], meaning the kinetic degree of freedom balances the effects of interactions. Similar findings were reported in the 1D Lieb lattice counterpart [111].

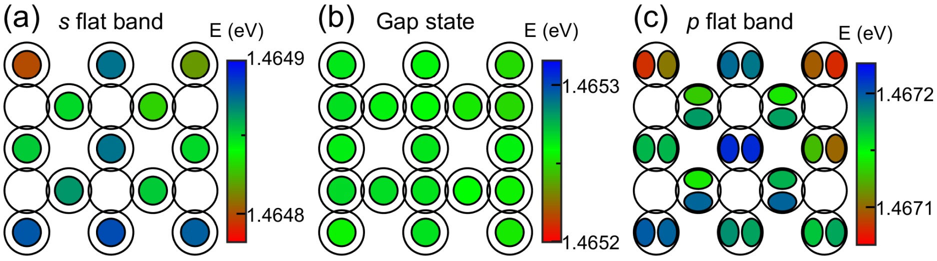

Fig. 5.13 Artificial colour plots showing the real space energy variation of emission from the s flat band (a), gap state (b) and p flat band (c).

In Fig. 5.14 we show a plot of the data presented in Fig. 5.13. Each data point corresponds to the emission from one orbital lobe (1 and 2 bright lobes for the s

and p orbitals respectively). Along the horizontal axis we see the intensity of the identified peaks, normalized to the average intensity of the ensemble (the Gaussian pump creates a broad distribution of intensities across the sites). Along the vertical axis the energy detuning of the peaks relative to the average condensate energy is plotted. A significant energy variation about the mean can be seen in the case of the flat-band condensates, which is absent for the gap state condensates. A positive correlation (positive slope) between the population (intensity) and on-site energy exists for the flat bands as demonstrated by the solid fitted least squares lines, as is expected for a blueshift arising from interactions, whereas the data points for the gap states all lie at the mean energy (dashed black line). Note that the flat-band energy fragmentation is on the order of 100-150 μeV, which lies within their spectral width ($\sim$0.2 meV) hence enabling the destructive interference required for their formation. The fact that flat-band eigenmodes are localized also explains why they are favoured for condensation in the first place, since injected particles (which act as a source for condensation) do not propagate out of the pump region, maximizing the overlap integral of the pump and final state [210].

5.4 Pseudospin textures

The Lieb lattice emission was also measured in the four linear polarization bases above condensation threshold. When passing from below to above this threshold, there was a sharp increase in the total degree of linear polarization of the emission, as is commonly

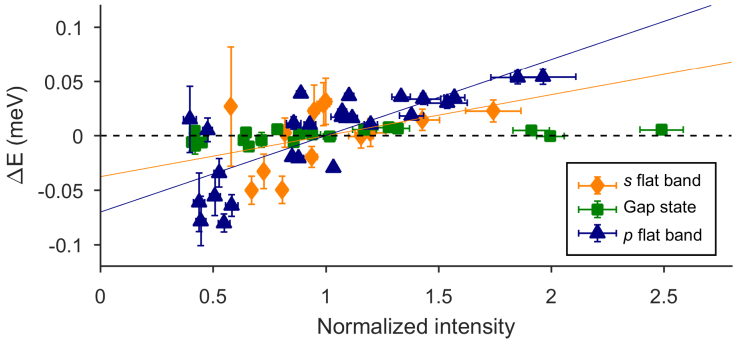

Fig. 5.14 On-site energy (with respect to ensemble average) vs. normalized intensity of individual photonic orbitals for data shown in Fig. 5.13.

reported in polariton condensates. A large contribution in this case comes from the gap states which are strongly horizontally polarized. Since different decay rates exist for different linear polarizations, maximum gain occurs in the state with the smallest total losses. In contrast, in the flat bands, where we have already seen distinctive intensity patterns [Fig. 5.5], macroscopic polarization textures were revealed in the emission.

Real space polarization maps of the s- and p-type flat band condensates are shown in Fig. 5.15. Periodic polarization patterns extended across several unit cells can be observed. This shows the presence of polarization terms with magnitude comparable to or greater than the polariton decay rate, leading to a modest degree of linear polarization in the measured PL emission. In Ref. [218], a phenomenological analysis of the pseudospin textures was provided by E. Cancellieri [see Appendix B]. A simple nearest-neighbour TB Hamiltonian with polarization-dependent hopping energies is sufficient to explain and emulate the observed pseudospin patterns. It should be noted that, compared to the last chapter, where analysis of the $l = 1$ (p) modes included an on-site correction to their energies, the sample studied here features a combination of a smaller β factor, broader linewidths and larger exciton fraction, meaning that the influence of TE-TM splitting was substantially smaller and did not play a significant in the experimental observations, and hence was not included in the analysis.

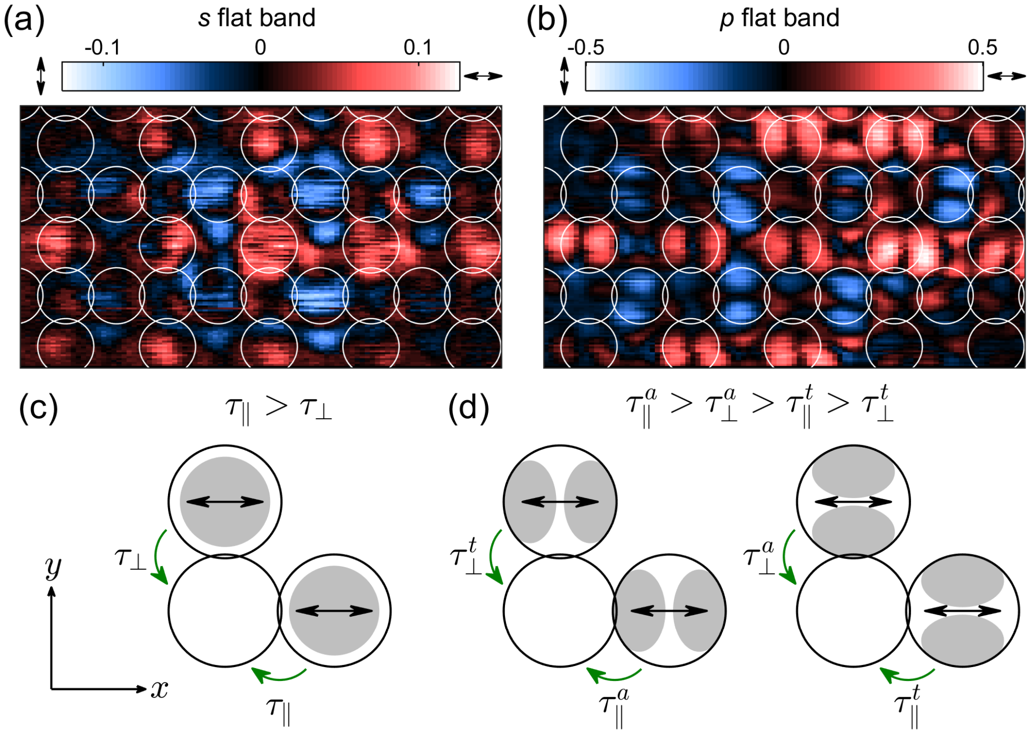

Fig. 5.15 Rectilinear polarization maps (Stokes parameter S_1) of emission from the s flat band (a) and p flat band (b). Schematic of the nearest neighbour particle tunnelling processes for s orbitals (c) and $p_{x,y}$ orbitals (d).

The hopping processes described by this model are depicted in Figs. 5.15(c),(d). Just as the combination of tunnelling constraints imposed by flat band formation and directionally-dependent hopping has previously been shown to lock the orientation of p orbitals [Fig. 5.5(c)], the polarization-dependent tunnelling here also creates a staggered hopping effect which locks the polarization. Specifically, tunnelling of horizontally-polarized orbitals in suppressed along the y direction (A to B sites), leading to an increased population in these orbitals on the A sublattice to compensate.

The opposite holds for tunnelling from C to B sites, where horizontal polarization is favoured and hence vertical polarization is dominant on the C sublattice. This TB model uses linear polarization splittings on the order of $10 - 100$ μeV to successfully replicate the intensity and pseudospin patterns in the flat bands.

5.5 Summary

To summarize, the spatial, spectral and pseudospin properties of 2D Lieb lattices for polaritons have been studied in both linear and nonlinear regimes. The lattices, fabricated via full and partial etching of planar microcavities, showed pronounced band structure formation induced by the periodic modulation of the energy landscape, and access to the spatial wave functions of different modes using optical tomography revealed distinctive intensity patterns associated with the flat bands. Using pulsed excitation at normal and oblique incidence, tuned to be (quasi-) resonant with polariton states below band gap, high-density regimes were explored wherein large nonlinearities were observed. Pseudospin textures arising from the polarization-dependent tunnelling of polaritons between pillars were also revealed. The results show the potential for engineering versatile lattice Hamiltonians for polaritons, highlighting the ease with which spin-orbit coupling terms and population of higher orbitals can be implemented, which presents a significant advantage of this system. Furthermore, the observation of flat-band condensate fragmentation demonstrates the effect of many-body interactions in the presence of quenched kinetic energy. An intriguing future prospect is studying quantum fluctuations as in recent polariton works [224, 149, 101] in lattice environments where novel driven-dissipative phase transitions are expected. Currently the strength of polariton-polariton interactions in a single lattice site (few μeV) [36] is comparable to or less than the polariton decay rate. However, the ratio of these two quantities may be further enhanced via polariton Feshbach resonances [225] or recently developed high-Q open-access microcavities with strong lateral confinement [203]. This would open the way to strongly correlated regimes described by driven-dissipative Bose-Hubbard models in polaritonic lattices [226].

Chapter 6

Conclusions and outlook

6.1 Summary

In this thesis, monolithic and nanofabricated semiconductor microcavities have been experimentally investigated in both linear and nonlinear regimes. In particular, internal degrees of freedom in the system such as polarization and orbital angular momentum have been considered in a variety of phenomena relating to pattern formation, topology and nonlinear lattice effects.

In Chapter 3, planar microcavities were studied under high-power pulsed excitation where the spontaneous formation of vortex patterns was observed. It was shown that under conventional plane wave excitation, a ring of polariton states at fixed wave vector is excited on the lower polariton branch, leading to a Bessel distribution of injected polaritons, which becomes unstable against symmetry-breaking pattern-forming instabilities beyond a critical pumping threshold. The spontaneous nucleation of even and odd polygon patterns of increasing order was observed as the polariton density was increased, and it was shown how varying the central power density under fixed pumping intensity enabled switching between patterns. The optically-controlled rotation of patterns was addressed experimentally and theoretically. At the same time, statistical properties of the microcavity emission were considered by studying the second order coherence and signal noise. It was shown in the former case that a narrow peak exists across the bistability threshold possibily related to superlinear kinetics of the polariton system. In the latter case, an oscillating signal far above shot noise was revealed in the amplitude fluctuations of the microcavity emission which arise due to transitions between different pattern states and between lower and upper stable branches in the vicinity of the threshold.

In Chapter 4, one-dimensional zigzag chains of micropillars were addressed under low-power incoherent excitation, and the polarization degree of freedom was shown to have different effects on the topological edge states of the system. Specifically, an on-site polarization splitting term was shown to perturb the energies of the edge states whilst a polarization-dependent tunnelling term was demonstrated to give different localization lengths for the two polarizations. This represents to the best of this author's knowledge the first time spinor effects have been studied in photonic SSH chains, where the huge enhancement of typically weak spin-orbit coupling of light is made possible in modulated microcavity structure lattices due to the wavelength-scale confinement of light in a structure with large in-plane index steps.

In Chapter 5, two-dimensional Lieb lattices of micropillars were studied in low-power and high-power non-resonant and quasi-resonant regimes. A multi-mode condensation behaviour was reported under both high-angle and normal-incidence excitation, wherein lasing occurred in the p modes followed by a relaxation towards the s modes at higher powers due to nonlinear scattering. Intriguingly, the flat band emission was shown to feature a pronounced pseudospin texture arising from the polarization degree of freedom, and intensity pattern in the case of the p flat band as a result of the directional dependence to hopping due to its axial asymmetry. Finally, the quenched kinetic energy scale of flat-band particles was evidenced by analyzing the spectral variation in the emission across different lattice sites, where a significant fragmentation of the condensate energy was observed. The role of interactions was highlighted by the correlation between mode blueshift and population.

6.2 Future directions

The work presented in this thesis paves the way towards many potential future studies of exciton-polaritons in both planar and etched microcavities. A research direction of considerable contemporary interest within and outside of the polariton community is the engineering of topological phases for photons, for which confined polaritons in lattice environments are an ideal platform to study novel nonlinear, spinor and non-Hermitian phenomena associated with topology. Whilst the measurements from Chapter 3 were performed using unconfined polaritons, they shed interesting light on optical bistability, parametric instabilities and photon bunching in polariton systems, which not only highlight potentially favourable features of polariton systems compared to other photonic platforms but are yet to be studied in lattice environments where features such as bistability may be exploited for use in topological states [227]. The results presented in Chapters 4 and 5 provide some early indications of the numerous fascinating photonic and polaritonic features associated with semiconductor micropillar lattices. Here a few potential future research directions which build upon the experiments performed in the previous chapters will be discussed.

6.2.1 Towards artificial gauge fields

Besides the Lieb lattices reported in Chapter 5, honeycomb lattices (i.e. polariton graphene [106]) were fabricated as an another interesting lattice geometry to study. By using the analytical tight-binding expressions for the π and π^* bands in the presence of nearest-neighbour (NN) and next-nearest-neighbour (NNN) coupling [228], curves can be fitted to experimentally measured dispersions to extract the NN coupling (t) and NNN coupling (t') strengths. By fabricating several repeats of the lattice with different periodicities, one can obtain a rough idea of the dependence between tunnelling energy and pillar separation[1], for use in the design of pseudomagnetic fields [see Fig. 6.1]. The interest in pseudomagnetic fields lies in the potential for studying artificial magnetic effects in optical systems which are otherwise inaccessible due to the weak magneto-optical response. For example, depending on the strain geometry different

---

[1] It should be noted that this of course depends on the particle effective mass (cavity-exciton detuning) and confinement depth.

edge states may be observed as discussed theoretically in a recent work [229] whilst it has been shown theoretically [230] and experimentally using coupled waveguide arrays [231] that photonic pseudo-Landau levels (pLLs) may be engineered using strain. Based on preliminary calculations from the dependence extracted in Fig. 6.1, it seems that it may be difficult to create well-separated pLLs within a realistic range of pillar separations. However, triggering polariton lasing in pLLs may offer a way to circumvent this issue.

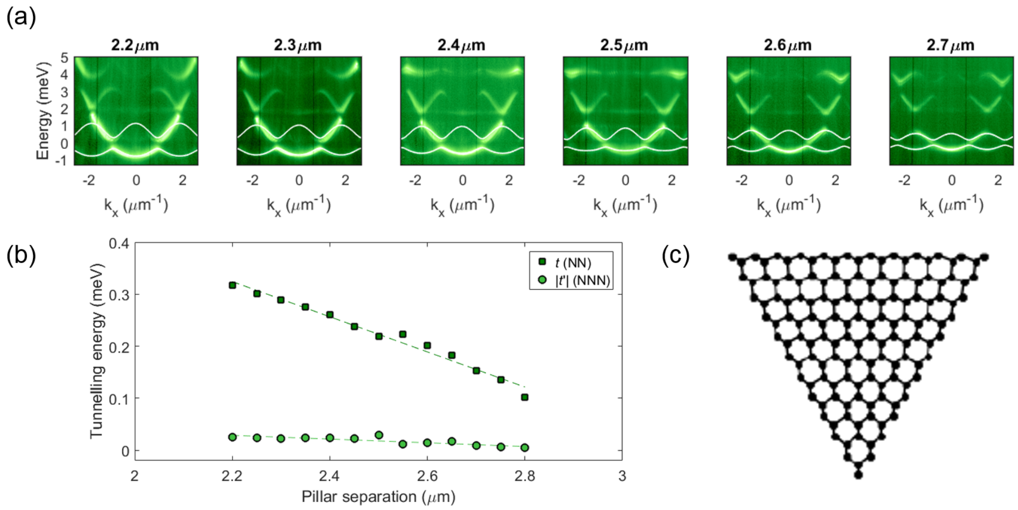

Fig. 6.1 (a) Measured dispersions in honeycomb lattices with different lattice constants from Sample 2, showing fitted tight-binding curves. (b) A plot of t and $|t'|$ extracted from experimental data for pillar separations ranging between 2.2 and 2.8 μm. The dependence within this range is approximately linear, as shown by the best fit lines. (c) Schematic of a preliminary strained honeycomb lattice design. Starting from the central plaquette (six sites), the pillar separation changes slightly with each successive coating, inducing pLLs in the dispersion.

Alternatively, effective magnetic fields arising from microcavity TE-TM splitting, which was discussed in Section 1.4.2, may also be engineered in lattice environments. For example, it has been shown theoretically for the case of a honeycomb lattice [207] that the reduced spatial symmetry of the periodic potential compared to a planar microcavity transforms the double-winding TE-TM field, previously sketched in Fig. 1.9 and visualized in Fig. 2.9, into a Dresselhaus-type field in the vicinity of the Dirac points, wherein the linear polarization angle is expected to wind singly around the K and K' points.

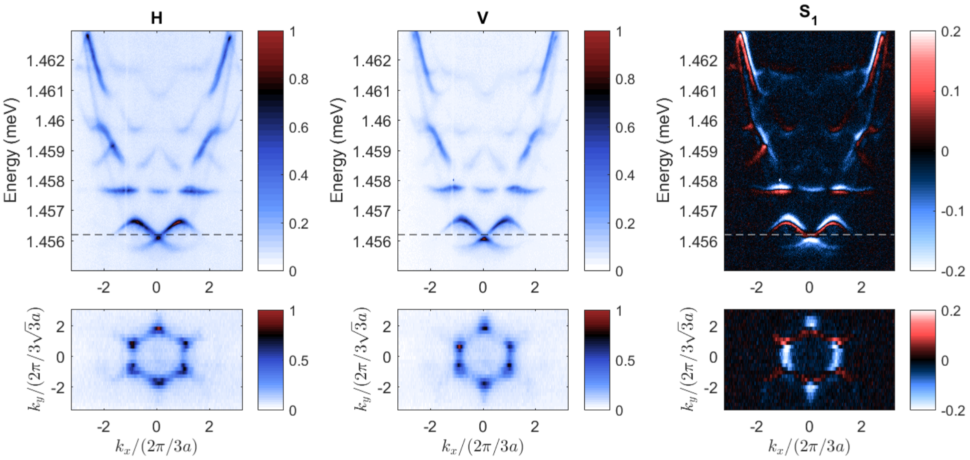

Fig. 6.2 Upper panel: Experimentally measured dispersion relations for a honeycomb lattice with periodicity $a = 2.40$ μm (shown at $k_y/(2\pi/3\sqrt{3}a) = 1$) in H and V bases, with the corresponding Stokes parameter S_1 showing polarization splitting of the bands. Lower panel: Corresponding Fourier space maps at the energies of the dashed lines in the upper panel. It can be seen in the S_1 map that the polarization winds only once around the Dirac points (the six vertices of the hexagonal pattern).

Engineering lattices with large polarization splitting paves the way towards interesting future studies of spinor phenomena in lattices, such as spin precession under resonant injection of wave packets [207], spin-dependent barrier tunnelling [221], whilst also fulfilling early criteria for the realization of topologically insulating phases with real or self-induced (by spin-anisotropic interactions) Zeeman fields, not just in honeycomb lattices [232, 191] but also Kagome [220] and Lieb [233] lattices.

6.2.2 Other polaritonic systems

Besides the micropillar lattices which have been discussed in this thesis, other systems capable of supporting exciton-polaritons may also offer certain advantages or capabilities compared to etched microcavities. For example, another highly promising system to study confined polaritons is in the slab waveguide geometry as in Refs. [36, 39], where solitons, continuum generation and self-phase modulation[2] have been studied in highly nonlinear regimes (so far without lateral confinement). Perhaps more intriguingly, in the paraxial approximation the evolution equation describing the waveguide system becomes formally analagous to the nonlinear Schrödinger or Gross- Pitaevskii equations, but with the propagation direction z replacing time t, which could allow the simulation of topological [186] or PT symmetric [234] Hamiltonians.

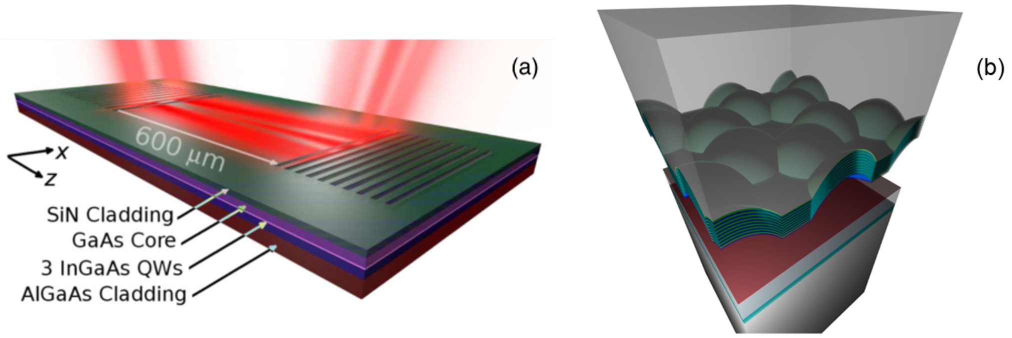

Fig. 6.3 Two possible alternative candidates for future research into confined exciton-polaritons. (a) Schematic of the GaAs-based slab waveguide device, where a guided photonic mode couples to quantum well excitons embedded in the core layer, studied in Ref. [39]. (b) Design schematic of a lattice in the open cavity geometry, formed from periodically positioned concave mirrors and a tuneable air gap. Image courtesy of M. Sich.

---

[2] The latter two effects are the subject of an upcoming publication by P. M. Walker.

Another interesting geometry is the open cavity geometry [199, 235, 203, 101], where strong lateral confinement has shown to lead to small mode volumes which are not possible in micropillars. Open cavity lattices [see Fig. 6.3(b)] potentially allow future studies of driven-dissipative phase transitions [236] and Bose-Hubbard models [226], whilst also offering a possible route towards elusive quantum polaritonic regimes [102].

Bibliography

[1] Stéphane Kéna-Cohen and Stephen R. Forrest. *Exciton–Polaritons in Organic Semiconductor Optical Microcavities*, pages 349–375. Springer Berlin Heidelberg, Berlin, Heidelberg, 2012.

[2] Daniele Sanvitto and Stephane Kena-Cohen. The road towards polaritonic devices. *Nat Mater*, 15(10):1061–1073, Oct 2016. Review.

[3] O. Madelung, U. Rössler, and M. Schulz, editors. *Gallium arsenide (GaAs) dielectric constants*, pages 1–11. Springer Berlin Heidelberg, Berlin, Heidelberg, 2001.

[4] S. I. Pekar. Theory of electromagnetic waves in a crystal in which excitons arise. *Sov. Phys. JETP*, 6(4):785, 1958.

[5] J. J. Hopfield. Theory of the contribution of excitons to the complex dielectric constant of crystals. *Phys. Rev.*, 112:1555–1567, Dec 1958.

[6] C.F. Klingshirn. *Semiconductor Optics*. Advanced Texts in Physics. Springer Berlin Heidelberg, 2006.

[7] A.V. Kavokin, J.J. Baumberg, G. Malpuech, and F.P. Laussy. *Microcavities*. Series on Semiconductor Science and Technology. OUP Oxford, 2017.

[8] W. T. Masselink, P. J. Pearah, J. Klem, C. K. Peng, H. Morkoç, G. D. Sanders, and Yia-Chung Chang. Absorption coefficients and exciton oscillator strengths in algaas-gaas superlattices. *Phys. Rev. B*, 32:8027–8034, Dec 1985.

[9] Kerry J. Vahala. Optical microcavities. *Nature*, 424:839 EP –, Aug 2003.

[10] R. N. Hall, G. E. Fenner, J. D. Kingsley, T. J. Soltys, and R. O. Carlson. Coherent light emission from gaas junctions. *Phys. Rev. Lett.*, 9:366–368, Nov 1962.

[11] Marshall I. Nathan, William P. Dumke, Gerald Burns, Frederick H. Dill Jr., and Gordon Lasher. Stimulated emission of radiation from gaas p-n junctions. *Applied Physics Letters*, 1(3):62–64, 1962.

[12] J J Coleman. The development of the semiconductor laser diode after the first demonstration in 1962. *Semiconductor Science and Technology*, 27(9):090207, 2012.

[13] C. Weisbuch, M. Nishioka, A. Ishikawa, and Y. Arakawa. Observation of the coupled exciton-photon mode splitting in a semiconductor quantum microcavity. *Phys. Rev. Lett.*, 69:3314–3317, Dec 1992.

[14] Yongbao Sun, Patrick Wen, Yoseob Yoon, Gangqiang Liu, Mark Steger, Loren N. Pfeiffer, Ken West, David W. Snoke, and Keith A. Nelson. Bose-einstein condensation of long-lifetime polaritons in thermal equilibrium. *Phys. Rev. Lett.*, 118:016602, Jan 2017.

[15] L. Tinkler, P. M. Walker, E. Clarke, D. N. Krizhanovskii, F. Bastiman, M. Durska, and M. S. Skolnick. Design and characterization of high optical quality ingaas/gaas/algaas-based polariton microcavities. *Applied Physics Letters*, 106(2):021109, 2015.

[16] R. Houdré, C. Weisbuch, R. P. Stanley, U. Oesterle, P. Pellandini, and M. Ilegems. Measurement of cavity-polariton dispersion curve from angle-resolved photoluminescence experiments. *Phys. Rev. Lett.*, 73:2043–2046, Oct 1994.

[17] C. Ell, J. Prineas, T. R. Nelson, S. Park, H. M. Gibbs, G. Khitrova, S. W. Koch, and R. Houdré. Influence of structural disorder and light coupling on the excitonic response of semiconductor microcavities. *Phys. Rev. Lett.*, 80:4795–4798, May 1998.

[18] F. Pinsker, W. Bao, Y. Zhang, H. Ohadi, A. Dreismann, and J. J. Baumberg. Fractional quantum mechanics in polariton condensates with velocity-dependent mass. *Phys. Rev. B*, 92:195310, Nov 2015.

[19] V. Savona, F. Tassone, C. Piermarocchi, A. Quattropani, and P. Schwendimann. Theory of polariton photoluminescence in arbitrary semiconductor microcavity structures. *Phys. Rev. B*, 53:13051–13062, May 1996.

[20] F. Tassone, C. Piermarocchi, V. Savona, A. Quattropani, and P. Schwendimann. Bottleneck effects in the relaxation and photoluminescence of microcavity polaritons. *Phys. Rev. B*, 56:7554–7563, Sep 1997.

[21] A. Imamog¯lu, R. J. Ram, S. Pau, and Y. Yamamoto. Nonequilibrium condensates and lasers without inversion: Exciton-polariton lasers. *Phys. Rev. A*, 53:4250–4253, Jun 1996.

[22] Michael D. Fraser, Sven Höfling, and Yoshihisa Yamamoto. Physics and applications of exciton-polariton lasers. *Nature Materials*, 15:1049 EP –, Sep 2016.

[23] Daming Huang, Jen-Inn Chyi, and Hadis Morkoç. Carrier effects on the excitonic absorption in gaas quantum-well structures: Phase-space filling. *Phys. Rev. B*, 42:5147–5153, Sep 1990.

[24] Moongoo Choi, Koo-Chul Je, Sang-Youp Yim, and Seung-Han Park. Relative strength of the screened coulomb interaction and phase-space filling on exciton bleaching in multiple quantum well structures. *Phys. Rev. B*, 70:085309, Aug 2004.

[25] R. Houdré, J. L. Gibernon, P. Pellandini, R. P. Stanley, U. Oesterle, C. Weisbuch, J. O'Gorman, B. Roycroft, and M. Ilegems. Saturation of the strong-coupling regime in a semiconductor microcavity: Free-carrier bleaching of cavity polaritons. *Phys. Rev. B*, 52:7810–7813, Sep 1995.

[26] L. Kappei, J. Szczytko, F. Morier-Genoud, and B. Deveaud. Direct observation of the mott transition in an optically excited semiconductor quantum well. *Phys. Rev. Lett.*, 94:147403, Apr 2005.

[27] J Kasprzak, M Richard, S Kundermann, a Baas, P Jeambrun, J M J Keeling, F M Marchetti, M H Szymańska, R André, J L Staehli, V Savona, P B Littlewood, B Deveaud, and Le Si Dang. Bose-Einstein condensation of exciton polaritons. *Nature*, 443(7110):409–414, 2006.

[28] Hui Deng, Gregor Weihs, David Snoke, Jacqueline Bloch, and Yoshihisa Yamamoto. Polariton lasing vs. photon lasing in a semiconductor microcavity. *Proceedings of the National Academy of Sciences*, 100(26):15318–15323, 2003.

[29] Jonathan Keeling and Natalia G. Berloff. Spontaneous rotating vortex lattices in a pumped decaying condensate. *Phys. Rev. Lett.*, 100:250401, Jun 2008.

[30] J Rogel-Salazar. The gross-pitaevskii equation and bose-einstein condensates. *European Journal of Physics*, 34(2):247, 2013.

[31] F. Tassone and Y. Yamamoto. Exciton-exciton scattering dynamics in a semiconductor microcavity and stimulated scattering into polaritons. *Phys. Rev. B*, 59:10830–10842, Apr 1999.

[32] M. Vladimirova, S. Cronenberger, D. Scalbert, K. V. Kavokin, A. Miard, A. Lemaître, J. Bloch, D. Solnyshkov, G. Malpuech, and A. V. Kavokin. Polariton-polariton interaction constants in microcavities. *Phys. Rev. B*, 82:075301, Aug 2010.

[33] Lydie Ferrier, Esther Wertz, Robert Johne, Dmitry D. Solnyshkov, Pascale Senellart, Isabelle Sagnes, Aristide Lemaître, Guillaume Malpuech, and Jacqueline Bloch. Interactions in confined polariton condensates. *Phys. Rev. Lett.*, 106:126401, Mar 2011.

[34] A. S. Brichkin, S. I. Novikov, A. V. Larionov, V. D. Kulakovskii, M. M. Glazov, C. Schneider, S. Höfling, M. Kamp, and A. Forchel. Effect of coulomb interaction on exciton-polariton condensates in gaas pillar microcavities. *Phys. Rev. B*, 84:195301, Nov 2011.

[35] A. V. Sekretenko, S. S. Gavrilov, and V. D. Kulakovskii. Polariton-polariton interactions in microcavities under a resonant 10 to 100 picosecond pulse excitation. *Phys. Rev. B*, 88:195302, Nov 2013.

[36] P. M. Walker, L. Tinkler, D. V. Skryabin, a. Yulin, B. Royall, I. Farrer, D. a. Ritchie, M. S. Skolnick, and D. N. Krizhanovskii. Ultra-low-power hybrid light-matter solitons. *Nat. Commun.*, 6:8317, 2015.

[37] S. R. K. Rodriguez, A. Amo, I. Sagnes, L. Le Gratiet, E. Galopin, A. Lemaître, and J. Bloch. Interaction-induced hopping phase in driven-dissipative coupled photonic microcavities. *Nature Communications*, 7:11887 EP –, Jun 2016. Article.

[38] Yongbao Sun, Yoseob Yoon, Mark Steger, Gangqiang Liu, Loren N. Pfeiffer, Ken West, David W. Snoke, and Keith A. Nelson. Direct measurement of polariton-polariton interaction strength. *Nature Physics*, 13:870 EP –, Jun 2017. Article.

[39] P. M. Walker, L. Tinkler, B. Royall, D. V. Skryabin, I. Farrer, D. A. Ritchie, M. S. Skolnick, and D. N. Krizhanovskii. Dark solitons in high velocity waveguide polariton fluids. *Phys. Rev. Lett.*, 119:097403, Aug 2017.

[40] P. KAPITZA. Viscosity of liquid helium below the l-point. *Nature*, 141:74 EP –, Jan 1938.

[41] J. F. ALLEN and A. D. MISENER. Flow phenomena in liquid helium ii. *Nature*, 142:643 EP –, Oct 1938.

[42] F. LONDON. The l-phenomenon of liquid helium and the bose-einstein degeneracy. *Nature*, 141:643 EP –, Apr 1938.

[43] F. London. On the bose-einstein condensation. *Phys. Rev.*, 54:947–954, Dec 1938.

[44] L. Landau. Theory of the superfluidity of helium ii. *Phys. Rev.*, 60:356–358, Aug 1941.

[45] U. Essmann and H. Träuble". The direct observation of individual flux lines in type ii superconductors. *Physics Letters A*, 24(10):526 – 527, 1967.

[46] Hermann Träuble and Uwe Essmann. Flux-line arrangement in superconductors as revealed by direct observation. *Journal of Applied Physics*, 39(9):4052–4059, 1968.

[47] K. W. Madison, F. Chevy, W. Wohlleben, and J. Dalibard. Vortex formation in a stirred bose-einstein condensate. *Phys. Rev. Lett.*, 84:806–809, Jan 2000.

[48] J. R. Abo-Shaeer, C. Raman, J. M. Vogels, and W. Ketterle. Observation of vortex lattices in bose-einstein condensates. *Science*, 292(5516):476–479, 2001.

[49] K. G. Lagoudakis, M. Wouters, M. Richard, A. Baas, I. Carusotto, R. André, Le Si Dang, and B. Deveaud-Plédran. Quantized vortices in an exciton-polariton condensate. *Nature Physics*, 4:706 EP –, Aug 2008.

[50] A. Amo, J. Lefrere, S. Pigeon, C. Adrados, C. Ciuti, I. Carusotto, R. Houdré, E. Giacobino, and A Bramati. Observation of Superfluidity of Polaritons in Semiconductor Microcavities. *Nat. Phys.*, 5(11):14, 2008.

[51] A. Amo, S. Pigeon, D. Sanvitto, V. G. Sala, R. Hivet, I. Carusotto, F. Pisanello, G. Leménager, R. Houdré, E Giacobino, C. Ciuti, and A. Bramati. Polariton superfluids reveal quantum hydrodynamic solitons. *Science*, 332(6034):1167–1170, 2011.

[52] Gaël Nardin, Gabriele Grosso, Yoan Léger, Barbara Pietka, François Morier-Genoud, and Benoît Deveaud-Plédran. Hydrodynamic nucleation of quantized vortex pairs in a polariton quantum fluid. *Nature Physics*, 7:635 EP –, Apr 2011. Article.

[53] D. N. Krizhanovskii, D. M. Whittaker, R. A. Bradley, K. Guda, D. Sarkar, D. Sanvitto, L. Vina, E. Cerda, P. Santos, K. Biermann, R. Hey, and M. S. Skolnick. Effect of interactions on vortices in a nonequilibrium polariton condensate. *Phys. Rev. Lett.*, 104:126402, Mar 2010.

[54] T. Boulier, H. Terças, D. D. Solnyshkov, Q. Glorieux, E. Giacobino, G. Malpuech, and A. Bramati. Vortex chain in a resonantly pumped polariton superfluid. *Scientific Reports*, 5:9230 EP –, Mar 2015. Article.

[55] Georgios Roumpos, Michael D. Fraser, Andreas Löffler, Sven Höfling, Alfred Forchel, and Yoshihisa Yamamoto. Single vortex-antivortex pair in an exciton-polariton condensate. *Nature Physics*, 7:129 EP –, Nov 2010.

[56] K. Guda, M. Sich, D. Sarkar, P. M. Walker, M. Durska, R. A. Bradley, D. M. Whittaker, M. S. Skolnick, E. A. Cerda-Méndez, P. V. Santos, K. Biermann, R. Hey, and D. N. Krizhanovskii. Spontaneous vortices in optically shaped potential profiles in semiconductor microcavities. *Phys. Rev. B*, 87:081309, Feb 2013.

[57] C. Antón, G. Tosi, M. D. Martín, L. Vi na, A. Lemaître, and J. Bloch. Role of supercurrents on vortices formation in polariton condensates. *Opt. Express*, 20(15):16366–16373, Jul 2012.

[58] F. Ricci, W. Löffler, and M.P. van Exter. Instability of higher-order optical vortices analyzed with a multi-pinhole interferometer. *Opt. Express*, 20(20):22961–22975, Sep 2012.

[59] G. D. Telles, P. E. S. Tavares, A. R. Fritsch, A. Cidrim, V. S. Bagnato, A. C. White, A. J. Allen, and C. F. Barenghi. Twisted unwinding of multi-charged quantum vortex and generation of turbulence in atomic bose-einstein condensates, 2015.

[60] Kirill Kalinin, Matteo Silva, Julian D. Töpfer, Wolfgang Langbein, Natalia G. Berloff, and Pavlos G. Lagoudakis. Giant vortices of controlled multiplicity in polariton lattices, 2017.

[61] E. Karsenti. Self-organization in cell biology: a brief history. *Nat. Rev. Mol. Cell Biol.*, 9:255–262, 2008.

[62] Jean-Marie Lehn. Toward self-organization and complex matter. *Science*, 295(5564):2400–2403, 2002.

[63] Xiangbing Zeng, Robert Kieffer, Benjamin Glettner, Constance Nürnberger, Feng Liu, Karsten Pelz, Marko Prehm, Ute Baumeister, Harald Hahn, Heinrich Lang, Gillian A. Gehring, Christa H. M. Weber, Jamie K. Hobbs, Carsten Tschierske, and Goran Ungar. Complex multicolor tilings and critical phenomena in tetraphilic liquid crystals. *Science*, 331(6022):1302–1306, 2011.

[64] M. C. Cross and P. C. Hohenberg. Pattern formation outside of equilibrium. *Rev. Mod. Phys.*, 65(851), 1993.

[65] F.Tito Arecchi, Stefano Boccaletti, and PierLuigi Ramazza. Pattern formation and competition in nonlinear optics. *Physics Reports*, 318(1):1 – 83, 1999.

[66] J. K. Chana, M. Sich, F. Fras, A. V. Gorbach, D. V. Skryabin, E. Cancellieri, E. A. Cerda-Méndez, K. Biermann, R. Hey, P. V. Santos, M. S. Skolnick, and D. N. Krizhanovskii. Spatial patterns of dissipative polariton solitons in semiconductor microcavities. *Phys. Rev. Lett.*, 115:256401, Dec 2015.

[67] Vincenzo Ardizzone, Przemyslaw Lewandowski, M. H. Luk, Y. C. Tse, N. H. Kwong, Andreas Lücke, Marco Abbarchi, Emmanuel Baudin, Elisabeth Galopin, Jacqueline Bloch, Aristide Lemaitre, P. T. Leung, Philippe Roussignol, Rolf Binder, Jerome Tignon, and Stefan Schumacher. Formation and control of turing patterns in a coherent quantum fluid. *Scientific Reports*, 3:3016 EP –, Oct 2013. Article.

[68] Albrecht Werner, Oleg A. Egorov, and Falk Lederer. Exciton-polariton patterns in coherently pumped semiconductor microcavities. *Phys. Rev. B*, 89:245307, Jun 2014.

[69] Jonathan Keeling and Natalia Berloff. Exciton-polariton condensation. *Contemporary Physics*, 52(2):131–151, 2 2011.

[70] N. G. Berloff and J. Keeling. *Universality in Modelling Non-equilibrium Pattern Formation in Polariton Condensates*, pages 19–38. Springer Berlin Heidelberg, Berlin, Heidelberg, 2013.

[71] N H Kwong, C Y Tsang, Samuel M H Luk, Y C Tse, Chris K P Chan, P Lewandowski, P T Leung, Stefan Schumacher, and R Binder. Optical switching of polariton density patterns in a semiconductor microcavity. *Physica Scripta*, 92(3):034006, 2017.

[72] G. Panzarini, L. C. Andreani, A. Armitage, D. Baxter, M. S. Skolnick, V. N. Astratov, J. S. Roberts, A. V. Kavokin, M. R. Vladimirova, and M. A. Kaliteevski. Cavity-polariton dispersion and polarization splitting in single and coupled semiconductor microcavities. *Physics of the Solid State*, 41(8):1223–1238, Aug 1999.

[73] M. Z. Maialle, E. A. de Andrada e Silva, and L. J. Sham. Exciton spin dynamics in quantum wells. *Phys. Rev. B*, 47:15776–15788, Jun 1993.

[74] Dmitry Solnyshkov and Guillaume Malpuech. Chirality in photonic systems. *Comptes Rendus Physique*, 17(8):920 – 933, 2016. Polariton physics / Physique des polaritons.

[75] Alexey Kavokin, Guillaume Malpuech, and Mikhail Glazov. Optical spin hall effect. *Phys. Rev. Lett.*, 95:136601, Sep 2005.

[76] C. Leyder, M. Romanelli, J. Ph Karr, E. Giacobino, T. C. H. Liew, M. M. Glazov, A. V. Kavokin, G. Malpuech, and A. Bramati. Observation of the optical spin hall effect. *Nature Physics*, 3:628 EP –, Jul 2007.

[77] H. Flayac, D. D. Solnyshkov, I. A. Shelykh, and G. Malpuech. Transmutation of skyrmions to half-solitons driven by the nonlinear optical spin hall effect. *Phys. Rev. Lett.*, 110:016404, Jan 2013.

[78] E. Kammann, T. C. H. Liew, H. Ohadi, P. Cilibrizzi, P. Tsotsis, Z. Hatzopoulos, P. G. Savvidis, A. V. Kavokin, and P. G. Lagoudakis. Nonlinear optical spin hall effect and long-range spin transport in polariton lasers. *Phys. Rev. Lett.*, 109:036404, Jul 2012.

[79] A. Amo, T. C. H. Liew, C. Adrados, E. Giacobino, A. V. Kavokin, and A. Bramati. Anisotropic optical spin hall effect in semiconductor microcavities. *Phys. Rev. B*, 80:165325, Oct 2009.

[80] M. M. Glazov and L. E. Golub. Spin and transport effects in quantum microcavities with polarization splitting. *Phys. Rev. B*, 82:085315, Aug 2010.

[81] Yuan ping Feng and Harold N. Spector. Exciton linewidth due to scattering from free carriers in semiconducting quantum well structures. *Superlattices and Microstructures*, 3(5):459 – 461, 1987.

[82] A. Honold, L. Schultheis, J. Kuhl, and C. W. Tu. Collision broadening of two-dimensional excitons in a gaas single quantum well. *Phys. Rev. B*, 40:6442–6445, Sep 1989.

[83] Wei Liu, Desheng Jiang, Kejian Luo, Yaohui Zhang, and Xiaoping Yang. Broadening of the excitonic linewidth due to scattering of two-dimensional free carriers. *Applied Physics Letters*, 67(5):679–681, 1995.

[84] P. G. Savvidis, J. J. Baumberg, R. M. Stevenson, M. S. Skolnick, D. M. Whittaker, and J. S. Roberts. Angle-resonant stimulated polariton amplifier. *Phys. Rev. Lett.*, 84:1547–1550, Feb 2000.

[85] R. M. Stevenson, V. N. Astratov, M. S. Skolnick, D. M. Whittaker, M. Emam-Ismail, A. I. Tartakovskii, P. G. Savvidis, J. J. Baumberg, and J. S. Roberts. Continuous wave observation of massive polariton redistribution by stimulated scattering in semiconductor microcavities. *Phys. Rev. Lett.*, 85:3680–3683, Oct 2000.

[86] Iacopo Carusotto and Cristiano Ciuti. Spontaneous microcavity-polariton coherence across the parametric threshold: Quantum monte carlo studies. *Phys. Rev. B*, 72:125335, Sep 2005.

[87] A. Baas, J.-Ph. Karr, M. Romanelli, A. Bramati, and E. Giacobino. Quantum degeneracy of microcavity polaritons. *Phys. Rev. Lett.*, 96:176401, May 2006.

[88] S. M. H. Luk, N. H. Kwong, P. Lewandowski, S. Schumacher, and R. Binder. Optically controlled orbital angular momentum generation in a polaritonic quantum fluid. *Phys. Rev. Lett.*, 119:113903, Sep 2017.

[89] R. Butté, M. S. Skolnick, D. M. Whittaker, D. Bajoni, and J. S. Roberts. Dependence of stimulated scattering in semiconductor microcavities on pump power, angle, and energy. *Phys. Rev. B*, 68:115325, Sep 2003.

[90] D. M. Whittaker. Effects of polariton-energy renormalization in the microcavity optical parametric oscillator. *Phys. Rev. B*, 71:115301, Mar 2005.

[91] Alessandro Tredicucci, Yong Chen, Vittorio Pellegrini, Marco Börger, and Franco Bassani. Optical bistability of semiconductor microcavities in the strong-coupling regime. *Phys. Rev. A*, 54:3493–3498, Oct 1996.

[92] A. Baas, J. Ph. Karr, H. Eleuch, and E. Giacobino. Optical bistability in semiconductor microcavities. *Phys. Rev. A*, 69:023809, Feb 2004.

[93] N. A. Gippius, S. G. Tikhodeev, V. D. Kulakovskii, D. N. Krizhanovskii, and A. I. Tartakovskii. Nonlinear dynamics of polariton scattering in semiconductor microcavity: Bistability vs. stimulated scattering. *EPL (Europhysics Letters)*, 67(6):997, 2004.

[94] D. N. Krizhanovskii, S. S. Gavrilov, A. P. D. Love, D. Sanvitto, N. A. Gippius, S. G. Tikhodeev, V. D. Kulakovskii, D. M. Whittaker, M. S. Skolnick, and J. S. Roberts. Self-organization of multiple polariton-polariton scattering in semiconductor microcavities. *Phys. Rev. B*, 77:115336, Mar 2008.

[95] Fabrice P. Laussy, G. Malpuech, A. Kavokin, and P. Bigenwald. Spontaneous coherence buildup in a polariton laser. *Phys. Rev. Lett.*, 93:016402, Jun 2004.

[96] Paolo Schwendimann and Antonio Quattropani. Statistics of the polariton condensate. *Phys. Rev. B*, 77:085317, Feb 2008.

[97] Hui Deng, Gregor Weihs, Charles Santori, Jacqueline Bloch, and Yoshihisa Yamamoto. Condensation of semiconductor microcavity exciton polaritons. *Science*, 298(5591):199–202, 2002.

[98] J. Kasprzak, M. Richard, A. Baas, B. Deveaud, R. André, J.-Ph. Poizat, and Le Si Dang. Second-order time correlations within a polariton bose-einstein condensate in a cdte microcavity. *Phys. Rev. Lett.*, 100:067402, Feb 2008.

[99] Albert F. Adiyatullin, Mitchell D. Anderson, Pierre V. Busi, Hadis Abbaspour, Régis André, Marcia T. Portella-Oberli, and Benoit Deveaud. Temporally resolved second-order photon correlations of exciton-polariton bose-einstein condensate formation. *Applied Physics Letters*, 107(22):221107, 2015.

[100] Albert F. Adiyatullin, Mitchell D. Anderson, Hugo Flayac, Marcia T. Portella-Oberli, Fauzia Jabeen, Claudéric Ouellet-Plamondon, Gregory C. Sallen, and Benoit Deveaud. Periodic squeezing in a polariton josephson junction. *Nature Communications*, 8(1):1329, 2017.

[101] Thomas Fink, Anne Schade, Sven Höfling, Christian Schneider, and Ataç Imamoglu. Signatures of a dissipative phase transition in photon correlation measurements. *Nature Physics*, 2017.

[102] A. Verger, C. Ciuti, and I. Carusotto. Polariton quantum blockade in a photonic dot. *Phys. Rev. B*, 73:193306, May 2006.

[103] Na Young Kim, Kenichiro Kusudo, Congjun Wu, Naoyuki Masumoto, Andreas Löffler, Sven Höfling, Norio Kumada, Lukas Worschech, Alfred Forchel, and Yoshihisa Yamamoto. Dynamical d-wave condensation of exciton-polaritons in a two-dimensional square-lattice potential. *Nature Physics*, 7:681 EP –, Jun 2011.

[104] E. A. Cerda-Méndez, D. N. Krizhanovskii, M. Wouters, R. Bradley, K. Biermann, K. Guda, R. Hey, P. V. Santos, D. Sarkar, and M. S. Skolnick. Polariton condensation in dynamic acoustic lattices. *Phys. Rev. Lett.*, 105:116402, Sep 2010.

[105] Karol Winkler, Julian Fischer, Anne Schade, Matthias Amthor, Robert Dall, Jonas Geßler, Monika Emmerling, Elena A Ostrovskaya, Martin Kamp, Christian Schneider, and Sven Höfling. A polariton condensate in a photonic crystal potential landscape. *New Journal of Physics*, 17(2):023001, 2015.

[106] T. Jacqmin, I. Carusotto, I. Sagnes, M. Abbarchi, D. D. Solnyshkov, G. Malpuech, E. Galopin, A. Lemaître, J. Bloch, and A. Amo. Direct observation of dirac cones and a flatband in a honeycomb lattice for polaritons. *Phys. Rev. Lett.*, 112:116402, Mar 2014.

[107] T. Gutbrod, M. Bayer, A. Forchel, J. P. Reithmaier, T. L. Reinecke, S. Rudin, and P. A. Knipp. Weak and strong coupling of photons and excitons in photonic dots. *Phys. Rev. B*, 57:9950–9956, Apr 1998.

[108] Marta Galbiati, Lydie Ferrier, Dmitry D. Solnyshkov, Dimitrii Tanese, Esther Wertz, Alberto Amo, Marco Abbarchi, Pascale Senellart, Isabelle Sagnes, Aristide Lemaître, Elisabeth Galopin, Guillaume Malpuech, and Jacqueline Bloch. Polariton condensation in photonic molecules. *Phys. Rev. Lett.*, 108:126403, Mar 2012.

[109] V. G. Sala, D. D. Solnyshkov, I. Carusotto, T. Jacqmin, A. Lemaître, H. Terças, A. Nalitov, M. Abbarchi, E. Galopin, I. Sagnes, J. Bloch, G. Malpuech, and A. Amo. Spin-orbit coupling for photons and polaritons in microstructures. *Phys. Rev. X*, 5:011034, Mar 2015.

[110] D. Tanese, H. Flayac, D. Solnyshkov, A. Amo, A. Lemaître, E. Galopin, R. Braive, P. Senellart, I. Sagnes, G. Malpuech, and J. Bloch. Polariton condensation in solitonic gap states in a one-dimensional periodic potential. *Nature Communications*, 4:1749 EP –, Apr 2013. Article.

[111] F. Baboux, L. Ge, T. Jacqmin, M. Biondi, E. Galopin, A. Lemaître, L. Le Gratiet, I. Sagnes, S. Schmidt, H. E. Türeci, A. Amo, and J. Bloch. Bosonic condensation and disorder-induced localization in a flat band. *Phys. Rev. Lett.*, 116:066402, Feb 2016.

[112] Florent Baboux, Eli Levy, Aristide Lemaître, Carmen Gómez, Elisabeth Galopin, Luc Le Gratiet, Isabelle Sagnes, Alberto Amo, Jacqueline Bloch, and Eric Akkermans. Measuring topological invariants from generalized edge states in polaritonic quasicrystals. *Phys. Rev. B*, 95:161114, Apr 2017.

[113] C. W. Lai, N. Y. Kim, S. Utsunomiya, G. Roumpos, H. Deng, M. D. Fraser, T. Byrnes, P. Recher, N. Kumada, T. Fujisawa, and Y. Yamamoto. Coherent zero-state and p-state in an exciton-polariton condensate array. *Nature*, 450:529 EP –, Nov 2007.

[114] M Milićević, T Ozawa, P Andreakou, I Carusotto, T Jacqmin, E Galopin, A Lemaître, L Le Gratiet, I Sagnes, J Bloch, and A Amo. Edge states in polariton honeycomb lattices. *2D Materials*, 2(3):034012, 2015.

[115] M. Milićević, T. Ozawa, G. Montambaux, I. Carusotto, E. Galopin, A. Lemaître, L. Le Gratiet, I. Sagnes, J. Bloch, and A. Amo. Orbital edge states in a photonic honeycomb lattice. *Phys. Rev. Lett.*, 118:107403, Mar 2017.

[116] A. Amo, T. C. H. Liew, C. Adrados, R. Houdré, E. Giacobino, A. V. Kavokin, and A. Bramati. Exciton-polariton spin switches. *Nat Photon*, 4(6):361–366, Jun 2010.

[117] D. Ballarini, M. De Giorgi, E. Cancellieri, R. Houdré, E. Giacobino, R. Cingolani, A. Bramati, G. Gigli, and D. Sanvitto. All-optical polariton transistor. *Nature Communications*, 4:1778 EP –, Apr 2013. Article.

[118] E. Wertz, A. Amo, D. D. Solnyshkov, L. Ferrier, T. C. H. Liew, D. Sanvitto, P. Senellart, I. Sagnes, A. Lemaître, A. V. Kavokin, G. Malpuech, and J. Bloch. Propagation and amplification dynamics of 1d polariton condensates. *Phys. Rev. Lett.*, 109:216404, Nov 2012.

[119] H. S. Nguyen, D. Vishnevsky, C. Sturm, D. Tanese, D. Solnyshkov, E. Galopin, A. Lemaître, I. Sagnes, A. Amo, G. Malpuech, and J. Bloch. Realization of a double-barrier resonant tunneling diode for cavity polaritons. *Phys. Rev. Lett.*, 110:236601, Jun 2013.

[120] Félix Marsault, Hai Son Nguyen, Dimitrii Tanese, Aristide Lemaître, Elisabeth Galopin, Isabelle Sagnes, Alberto Amo, and Jacqueline Bloch. Realization of an all optical exciton-polariton router. *Applied Physics Letters*, 107(20):201115, 2015.

[121] C. Sturm, D. Tanese, H. S. Nguyen, H. Flayac, E. Galopin, A. Lemaître, I. Sagnes, D. Solnyshkov, A. Amo, G. Malpuech, and J. Bloch. All-optical phase modulation in a cavity-polariton mach-zehnder interferometer. *Nature Communications*, 5:3278 EP –, Feb 2014. Article.

[122] T. Gao, P. S. Eldridge, T. C. H. Liew, S. I. Tsintzos, G. Stavrinidis, G. Deligeorgis, Z. Hatzopoulos, and P. G. Savvidis. Polariton condensate transistor switch. *Phys. Rev. B*, 85:235102, Jun 2012.

[123] C. Antón, T. C. H. Liew, J. Cuadra, M. D. Martín, P. S. Eldridge, Z. Hatzopoulos, G. Stavrinidis, P. G. Savvidis, and L. Viña. Quantum reflections and shunting of polariton condensate wave trains: Implementation of a logic and gate. *Phys. Rev. B*, 88:245307, Dec 2013.

[124] Alexander Dreismann, Hamid Ohadi, Yago del Valle-Inclan Redondo, Ryan Balili, Yuri G. Rubo, Simeon I. Tsintzos, George Deligeorgis, Zacharias Hatzopoulos, Pavlos G. Savvidis, and Jeremy J. Baumberg. A sub-femtojoule electrical spin-switch based on optically trapped polariton condensates. *Nature Materials*, 15:1074 EP –, Aug 2016.

[125] Christian Schneider, Arash Rahimi-Iman, Na Young Kim, Julian Fischer, Ivan G. Savenko, Matthias Amthor, Matthias Lermer, Adriana Wolf, Lukas Worschech, Vladimir D. Kulakovskii, Ivan A. Shelykh, Martin Kamp, Stephan Reitzenstein, Alfred Forchel, Yoshihisa Yamamoto, and Sven Höfling. An electrically pumped polariton laser. *Nature*, 497:348 EP –, May 2013.

[126] Pallab Bhattacharya, Thomas Frost, Saniya Deshpande, Md Zunaid Baten, Arnab Hazari, and Ayan Das. Room temperature electrically injected polariton laser. *Phys. Rev. Lett.*, 112:236802, Jun 2014.

[127] K. V. Kavokin, M. A. Kaliteevski, R. A. Abram, A. V. Kavokin, S. Sharkova, and I. A. Shelykh. Stimulated emission of terahertz radiation by exciton-polariton lasers. *Applied Physics Letters*, 97(20):201111, 2010.

[128] A. V. Kavokin, I. A. Shelykh, T. Taylor, and M. M. Glazov. Vertical cavity surface emitting terahertz laser. *Phys. Rev. Lett.*, 108:197401, May 2012.

[129] Fabrice P. Laussy, Alexey V. Kavokin, and Ivan A. Shelykh. Exciton-polariton mediated superconductivity. *Phys. Rev. Lett.*, 104:106402, Mar 2010.

[130] Ovidiu Cotleţ, Sina Zeytinoğlu, Manfred Sigrist, Eugene Demler, and Ata ç Imamoğlu. Superconductivity and other collective phenomena in a hybrid bose-fermi mixture formed by a polariton condensate and an electron system in two dimensions. *Phys. Rev. B*, 93:054510, Feb 2016.

[131] Feng Li, L. Orosz, O. Kamoun, S. Bouchoule, C. Brimont, P. Disseix, T. Guillet, X. Lafosse, M. Leroux, J. Leymarie, G. Malpuech, M. Mexis, M. Mihailovic, G. Patriarche, F. Réveret, D. Solnyshkov, and J. Zuniga-Perez. Fabrication and characterization of a room-temperature zno polariton laser. *Applied Physics Letters*, 102(19):191118, 2013.

[132] Johannes D. Plumhof, Thilo Stöferle, Lijian Mai, Ullrich Scherf, and Rainer F. Mahrt. Room-temperature bose-einstein condensation of cavity exciton-polaritons in a polymer. *Nature Materials*, 13:247 EP –, Dec 2013.

[133] L. C. Flatten, Z. He, D. M. Coles, A. A. P. Trichet, A. W. Powell, R. A. Taylor, J. H. Warner, and J. M. Smith. Room-temperature exciton-polaritons with two-dimensional ws2. *Scientific Reports*, 6:33134 EP –, Sep 2016. Article.

[134] Yen-Jung Chen, Jeffrey D. Cain, Teodor K. Stanev, Vinayak P. Dravid, and Nathaniel P. Stern. Valley-polarized exciton-polaritons in a monolayer semiconductor. *Nature Photonics*, 11:431 EP –, Jun 2017. Article.

[135] I. Vurgaftman, J. R. Meyer, and L. R. Ram-Mohan. Band parameters for compound semiconductors and their alloys. *Journal of Applied Physics*, 89(11):5815–5875, 2001.

[136] J. Bloch, T. Freixanet, J. Y. Marzin, V. Thierry-Mieg, and R. Planel. Giant rabi splitting in a microcavity containing distributed quantum wells. *Applied Physics Letters*, 73(12):1694–1696, 1998.

[137] J. P. Reithmaier, M. Röhner, H. Zull, F. Schäfer, A. Forchel, P. A. Knipp, and T. L. Reinecke. Size dependence of confined optical modes in photonic quantum dots. *Phys. Rev. Lett.*, 78:378–381, Jan 1997.

[138] S Reitzenstein and A Forchel. Quantum dot micropillars. *Journal of Physics D: Applied Physics*, 43(3):033001, 2010.

[139] Gaël Nardin, Taofiq K. Paraïso, Roland Cerna, Barbara Pietka, Yoan Léger, Ounsi El Daif, François Morier-Genoud, and Benoît Deveaud-Plédran. Probability density optical tomography of confined quasiparticles in a semiconductor microcavity. *Applied Physics Letters*, 94(18):181103, 2009.

[140] A. M. Turing. The chemical basis of morphogenesis. *Phil. Trans. R. Soc. B*, 237(641):37–72, 1952.

[141] I. V. Grigorieva, W. Escoffier, J. Richardson, L. Y. Vinnikov, S. Dubonos, and V. Oboznov. Direct observation of vortex shells and magic numbers in mesoscopic superconducting disks. *Phys. Rev. Lett.*, 96:077005, Feb 2006.

[142] J. F. Nye and M. V. Berry. Dislocations in wave trains. *Proceedings of the Royal Society of London A: Mathematical, Physical and Engineering Sciences*, 336(1605):165–190, 1974.

[143] V.Yu. Bazhenov, M.S. Soskin, and M.V. Vasnetsov. Screw dislocations in light wavefronts. *Journal of Modern Optics*, 39(5):985–990, 1992.

[144] I.V. Basistiy, V.Yu. Bazhenov, M.S. Soskin, and M.V. Vasnetsov. Optics of light beams with screw dislocations. *Optics Communications*, 103(5):422 – 428, 1993.

[145] Xiaomei Zhang, Baifei Shen, Yin Shi, Xiaofeng Wang, Lingang Zhang, Wenpeng Wang, Jiancai Xu, Longqiong Yi, and Zhizhan Xu. Generation of intense high-order vortex harmonics. *Phys. Rev. Lett.*, 114:173901, Apr 2015.

[146] N. Apurv Chaitanya, M. V. Jabir, and G. K. Samanta. Efficient nonlinear generation of high power, higher order, ultrafast “perfect” vortices in green. *Opt. Lett.*, 41(7):1348–1351, Apr 2016.

[147] Gabriel Molina-Terriza, Juan P. Torres, and Lluis Torner. Twisted photons. *Nat Phys*, 3(5):305–310, May 2007.

[148] Alois Mair, Alipasha Vaziri, Gregor Weihs, and Anton Zeilinger. Entanglement of the orbital angular momentum states of photons. *Nature*, 412(6844):313–316, Jul 2001.

[149] C. E. Whittaker, B. Dzurnak, O. A. Egorov, G. Buonaiuto, P. M. Walker, E. Cancellieri, D. M. Whittaker, E. Clarke, S. S. Gavrilov, M. S. Skolnick, and D. N. Krizhanovskii. Polariton pattern formation and photon statistics of the associated emission. *Phys. Rev. X*, 7:031033, Aug 2017.

[150] G. Tosi, G. Christmann, N. G. Berloff, P. Tsotsis, T. Gao, Z. Hatzopoulos, P. G. Savvidis, and J. J. Baumberg. Geometrically locked vortex lattices in semiconductor quantum fluids. *Nature Communications*, 3:1243 EP –, Dec 2012. Article.

[151] F. Manni, K. G. Lagoudakis, T. K. Paraïso, R. Cerna, Y. Léger, T. C. H. Liew, I. A. Shelykh, A. V. Kavokin, F. Morier-Genoud, and B. Deveaud-Plédran. Spin-to-orbital angular momentum conversion in semiconductor microcavities. *Phys. Rev. B*, 83:241307, Jun 2011.

[152] Yongbao Sun, Yoseob Yoon, Saeed Khan, Li Ge, Mark Steger, Loren N. Pfeiffer, Ken West, Hakan E. Türeci, David W. Snoke, and Keith A. Nelson. Stable switching among high-order modes in polariton condensates. *Phys. Rev. B*, 97:045303, Jan 2018.

[153] L. Dominici, M. Petrov, M. Matuszewski, D. Ballarini, M. De Giorgi, D. Colas, E. Cancellieri, B. Silva Fernández, A. Bramati, G. Gigli, A. Kavokin, F. Laussy, and D. Sanvitto. Real-space collapse of a polariton condensate. 6:8993 EP –, Dec 2015. Article.

[154] J. J. Baumberg, P. G. Savvidis, R. M. Stevenson, A. I. Tartakovskii, M. S. Skolnick, D. M. Whittaker, and J. S. Roberts. Parametric oscillation in a vertical microcavity: A polariton condensate or micro-optical parametric oscillation. *Phys. Rev. B*, 62:R16247–R16250, Dec 2000.

[155] A. I. Tartakovskii, D. N. Krizhanovskii, and V. D. Kulakovskii. Polariton-polariton scattering in semiconductor microcavities: Distinctive features and similarities to the three-dimensional case. *Phys. Rev. B*, 62:R13298–R13301, Nov 2000.

[156] D. M. Whittaker. Vortices in the microcavity optical parametric oscillator. *Superlattices and Microstructures*, 41(5-6):297–300, 2007.

[157] J. O. Hamp, A. K. Balin, F. M. Marchetti, D. Sanvitto, and M. H. Szymańska. Spontaneous rotating vortex rings in a parametrically driven polariton fluid. *EPL (Europhysics Letters)*, 110(5):57006, 2015.

[158] S. Barreiro and J. W. R. Tabosa. Generation of light carrying orbital angular momentum via induced coherence grating in cold atoms. *Phys. Rev. Lett.*, 90:133001, Mar 2003.

[159] V. Pyragaite, K. Regelskis, V. Smilgevicius, and A. Stabinis. Noncollinear interaction of optical vortices in kerr nonlinear medium. *Optics Communications*, 198(4):459 – 464, 2001.

[160] D. Sanvitto, D. N. Krizhanovskii, D. M. Whittaker, S. Ceccarelli, M. S. Skolnick, and J. S. Roberts. Spatial structure and stability of the macroscopically occupied polariton state in the microcavity optical parametric oscillator. *Phys. Rev. B*, 73:241308, Jun 2006.

[161] A. Amo, M. D. Martín, D. Ballarini, L. Viña, D. Sanvitto, M. S. Skolnick, and J. S. Roberts. Angular switching of the linear polarization of the emission in ingaas microcavities. *physica status solidi (c)*, 2(11):3868–3871, 2005.

[162] Ł. Kłopotowski, M.D. Martín, A. Amo, L. Viña, I.A. Shelykh, M.M. Glazov, G. Malpuech, A.V. Kavokin, and R. André. Optical anisotropy and pinning of the linear polarization of light in semiconductor microcavities. *Solid State Communications*, 139(10):511 – 515, 2006.

[163] P. Renucci, T. Amand, X. Marie, P. Senellart, J. Bloch, B. Sermage, and K. V. Kavokin. Microcavity polariton spin quantum beats without a magnetic field: A manifestation of coulomb exchange in dense and polarized polariton systems. *Phys. Rev. B*, 72:075317, Aug 2005.

[164] D. N. Krizhanovskii, D. Sanvitto, I. A. Shelykh, M. M. Glazov, G. Malpuech, D. D. Solnyshkov, A. Kavokin, S. Ceccarelli, M. S. Skolnick, and J. S. Roberts. Rotation of the plane of polarization of light in a semiconductor microcavity. *Phys. Rev. B*, 73:073303, Feb 2006.

[165] S. S. Gavrilov. Blowup dynamics of coherently driven polariton condensates. *Phys. Rev. B*, 90:205303, 2014.

[166] Jean-Sebastian Tempel, Franziska Veit, Marc Aßmann, Lars E. Kreilkamp, Arash Rahimi-Iman, Andreas Löffler, Sven Höfling, Stephan Reitzenstein, Lukas Worschech, Alfred Forchel, and Manfred Bayer. Characterization of two-threshold behavior of the emission from a gaas microcavity. *Phys. Rev. B*, 85:075318, 2012.

[167] Hans A. Bachor and Timothy C. Ralph. *A Guide to Experiments in Quantum Optics*. 2004.

[168] S. Residori, P. L. Ramazza, E. Pampaloni, S. Boccaletti, and F. T. Arecchi. Domain coexistence in two-dimensional optical patterns. *Phys. Rev. Lett.*, 76:1063–1066, Feb 1996.

[169] D. Sanvitto and V. Timofeev. Exciton polaritons in microcavities. *Springer Verlag*, 2012.

[170] H. Flayac, D. D. Solnyshkov, and G. Malpuech. Oblique half-solitons and their generation in exciton-polariton condensates. *Phys. Rev. B*, 83:193305, May 2011.

[171] O. A. Egorov, A. Werner, T. C. H. Liew, E. A. Ostrovskaya, and F. Lederer. Motion of patterns in polariton quantum fluids with spin-orbit interaction. *Phys. Rev. B*, 89:235302, Jun 2014.

[172] N. A. Gippius, I. A. Shelykh, D. D. Solnyshkov, S. S. Gavrilov, Yuri G. Rubo, A. V. Kavokin, S. G. Tikhodeev, and G. Malpuech. Polarization multistability of cavity polaritons. *Phys. Rev. Lett.*, 98:236401, Jun 2007.

[173] John M Dudley, Frédéric Dias, Miro Erkintalo, and Goëry Genty. Instabilities, breathers and rogue waves in optics. *Nat. Photon.*, 8:755–764, 2014.

[174] T Boulier, M Bamba, a Amo, C Adrados, a Lemaitre, E Galopin, I Sagnes, J Bloch, C Ciuti, E Giacobino, and a Bramati. Polariton-generated intensity squeezing in semiconductor micropillars. *Nat. Commun.*, 5:3260, 2014.

[175] Oleksandr Kyriienko and Timothy C. H. Liew. Triggered single-photon emitters based on stimulated parametric scattering in weakly nonlinear systems. *Phys. Rev. A*, 90:063805, Dec 2014.

[176] P. G. Kevrekidis and D. J. Frantzeskakis. Pattern forming dynamical instabilities of bose-einstein condensates. *Modern Physics Letters B*, 18(05n06):173–202, 2004.

[177] P. J. Everitt, M. A. Sooriyabandara, M. Guasoni, P. B. Wigley, C. H. Wei, G. D. McDonald, K. S. Hardman, P. Manju, J. D. Close, C. C. N. Kuhn, S. S. Szigeti, Y. S. Kivshar, and N. P. Robins. Observation of a modulational instability in bose-einstein condensates. *Phys. Rev. A*, 96:041601, Oct 2017.

[178] Huan Wang, Linghua Wen, Hui Yang, Chunxiao Shi, and Jinghong Li. Vortex states and spin textures of rotating spin-orbit-coupled bose-einstein condensates in a toroidal trap. *Journal of Physics B: Atomic, Molecular and Optical Physics*, 50(15):155301, 2017.

[179] F. D. M. Haldane and S. Raghu. Possible realization of directional optical waveguides in photonic crystals with broken time-reversal symmetry. *Phys. Rev. Lett.*, 100:013904, Jan 2008.

[180] Alexander B. Khanikaev, S. Hossein Mousavi, Wang-Kong Tse, Mehdi Kargarian, Allan H. MacDonald, and Gennady Shvets. Photonic topological insulators. *Nature Materials*, 12:233 EP –, Dec 2012. Article.

[181] Ling Lu, John D. Joannopoulos, and Marin Soljacic. Topological photonics. *Nat Photon*, 8(11):821–829, Nov 2014. Review.

[182] Alexander B. Khanikaev and Gennady Shvets. Two-dimensional topological photonics. *Nature Photonics*, 11(12):763–773, 2017.

[183] Tomoki Ozawa, Hannah M. Price, Alberto Amo, Nathan Goldman, Mohammad Hafezi, Ling Lu, Mikael Rechtsman, David Schuster, Jonathan Simon, Oded Zilberberg, and Iacopo Carusotto. Topological photonics, 2018.

[184] Zheng Wang, Yidong Chong, J. D. Joannopoulos, and Marin Soljacic. Observation of unidirectional backscattering-immune topological electromagnetic states. *Nature*, 461:772 EP –, Oct 2009.

[185] M. Hafezi, S. Mittal, J. Fan, A. Migdall, and J. M. Taylor. Imaging topological edge states in silicon photonics. *Nature Photonics*, 7:1001 EP –, Oct 2013. Article.

[186] Mikael C. Rechtsman, Julia M. Zeuner, Yonatan Plotnik, Yaakov Lumer, Daniel Podolsky, Felix Dreisow, Stefan Nolte, Mordechai Segev, and Alexander Szameit. Photonic floquet topological insulators. *Nature*, 496:196 EP –, Apr 2013.

[187] P. St-Jean, V. Goblot, E. Galopin, A. Lemaître, T. Ozawa, L. Le Gratiet, I. Sagnes, J. Bloch, and A. Amo. Lasing in topological edge states of a one-dimensional lattice. *Nature Photonics*, 11(10):651–656, 2017.

[188] Sabyasachi Barik, Aziz Karasahin, Christopher Flower, Tao Cai, Hirokazu Miyake, Wade DeGottardi, Mohammad Hafezi, and Edo Waks. A topological quantum optics interface. *Science*, 359(6376):666–668, 2018.

[189] Alberto Amo and Jacqueline Bloch. Exciton-polaritons in lattices: A non-linear photonic simulator. *Comptes Rendus Physique*, 17(8):934 – 945, 2016. Polariton physics / Physique des polaritons.

[190] C Schneider, K Winkler, M D Fraser, M Kamp, Y Yamamoto, E A Ostrovskaya, and S Höfling. Exciton-polariton trapping and potential landscape engineering. *Reports on Progress in Physics*, 80(1):016503, 2017.

[191] A. V. Nalitov, D. D. Solnyshkov, and G. Malpuech. Polariton $\mathbb{Z}$ topological insulator. *Phys. Rev. Lett.*, 114:116401, Mar 2015.

[192] Charles-Edouard Bardyn, Torsten Karzig, Gil Refael, and Timothy C. H. Liew. Topological polaritons and excitons in garden-variety systems. *Phys. Rev. B*, 91:161413, Apr 2015.

[193] Torsten Karzig, Charles-Edouard Bardyn, Netanel H. Lindner, and Gil Refael. Topological polaritons. *Phys. Rev. X*, 5:031001, Jul 2015.

[194] Kexin Yi and Torsten Karzig. Topological polaritons from photonic dirac cones coupled to excitons in a magnetic field. *Phys. Rev. B*, 93:104303, Mar 2016.

[195] János K. Asbóth, László Oroszlány, and András Pályi. *The Su-Schrieffer-Heeger (SSH) Model*, pages 1–22. Springer International Publishing, Cham, 2016.

[196] C. Kittel. *Introduction to Solid State Physics*. Wiley, 2004.

[197] C. Schneider, P. Gold, S. Reitzenstein, S. Höfling, and M. Kamp. Quantum dot micropillar cavities with quality factors exceeding 250,000. *Applied Physics B*, 122(1):19, Jan 2016.

[198] Daniele Bajoni. Polariton lasers. hybrid light-matter lasers without inversion. *Journal of Physics D: Applied Physics*, 45(31):313001, 2012.

[199] S. Dufferwiel, F. Fras, A. Trichet, P. M. Walker, F. Li, L. Giriunas, M. N. Makhonin, L. R. Wilson, J. M. Smith, E. Clarke, M. S. Skolnick, and D. N. Krizhanovskii. Strong exciton-photon coupling in open semiconductor microcavities. *Applied Physics Letters*, 104(19):192107, 2014.

[200] Gaël Nardin, Yoan Léger, Barbara Pietka, Fran çois Morier-Genoud, and Benoît Deveaud-Plédran. Phase-resolved imaging of confined exciton-polariton wave functions in elliptical traps. *Phys. Rev. B*, 82:045304, Jul 2010.

[201] S. Michaelis de Vasconcellos, A. Calvar, A. Dousse, J. Suffczyński, N. Dupuis, A. Lemaître, I. Sagnes, J. Bloch, P. Voisin, and P. Senellart. Spatial, spectral, and polarization properties of coupled micropillar cavities. *Applied Physics Letters*, 99(10):101103, 2011.

[202] P. W. Atkins and R. S. Friedman. *Molecular quantum mechanics.* Oxford University Press, 5th ed edition, 2011.

[203] S. Dufferwiel, Feng Li, E. Cancellieri, L. Giriunas, A. A. P. Trichet, D. M. Whittaker, P. M. Walker, F. Fras, E. Clarke, J. M. Smith, M. S. Skolnick, and D. N. Krizhanovskii. Spin textures of exciton-polaritons in a tunable microcavity with large te-tm splitting. *Phys. Rev. Lett.*, 115:246401, Dec 2015.

[204] F. Prati, G. Tissoni, M. San Miguel, and N.B. Abraham. Vector vortices and polarization state of low-order transverse modes in a vcsel. *Optics Communications*, 143(1):133 – 146, 1997.

[205] Filippo Cardano, Ebrahim Karimi, Sergei Slussarenko, Lorenzo Marrucci, Corrado de Lisio, and Enrico Santamato. Polarization pattern of vector vortex beams generated by q-plates with different topological charges. *Appl. Opt.*, 51(10):C1–C6, Apr 2012.

[206] Lei Gong, Yuxuan Ren, Weiwei Liu, Meng Wang, Mincheng Zhong, Ziqiang Wang, and Yinmei Li. Generation of cylindrically polarized vector vortex beams with digital micromirror device. *Journal of Applied Physics*, 116(18):183105, 2014.

[207] A. V. Nalitov, G. Malpuech, H. Terças, and D. D. Solnyshkov. Spin-orbit coupling and the optical spin hall effect in photonic graphene. *Phys. Rev. Lett.*, 114:026803, Jan 2015.

[208] D. D. Solnyshkov, A. V. Nalitov, and G. Malpuech. Kibble-zurek mechanism in topologically nontrivial zigzag chains of polariton micropillars. *Phys. Rev. Lett.*, 116:046402, Jan 2016.

[209] J. Zak. Berry's phase for energy bands in solids. *Phys. Rev. Lett.*, 62:2747–2750, Jun 1989.

[210] Berihu Teklu, Dmitry Solnyshkov, and Guillaume Malpuech. Non-equilibrium condensation in periodic polariton lattices. *Superlattices and Microstructures*, 100(Supplement C):1 – 8, 2016.

[211] Elliott H. Lieb. Two theorems on the hubbard model. *Phys. Rev. Lett.*, 62:1201–1204, Mar 1989.

[212] B. Keimer, S. A. Kivelson, M. R. Norman, S. Uchida, and J. Zaanen. From quantum matter to high-temperature superconductivity in copper oxides. *Nature*, 518:179 EP –, Feb 2015. Review Article.

[213] Bill Sutherland. Localization of electronic wave functions due to local topology. *Phys. Rev. B*, 34:5208–5211, Oct 1986.

[214] Rodrigo A. Vicencio, Camilo Cantillano, Luis Morales-Inostroza, Bastián Real, Cristian Mejía-Cortés, Steffen Weimann, Alexander Szameit, and Mario I. Molina. Observation of localized states in lieb photonic lattices. *Phys. Rev. Lett.*, 114:245503, Jun 2015.

[215] Shintaro Taie, Hideki Ozawa, Tomohiro Ichinose, Takuei Nishio, Shuta Nakajima, and Yoshiro Takahashi. Coherent driving and freezing of bosonic matter wave in an optical lieb lattice. *Science Advances*, 1(10), 2015.

[216] Robert Drost, Teemu Ojanen, Ari Harju, and Peter Liljeroth. Topological states in engineered atomic lattices. *Nature Physics*, 13:668 EP –, Mar 2017.

[217] Marlou R. Slot, Thomas S. Gardenier, Peter H. Jacobse, Guido C. P. van Miert, Sander N. Kempkes, Stephan J. M. Zevenhuizen, Cristiane Morais Smith, Daniel Vanmaekelbergh, and Ingmar Swart. Experimental realization and characterization of an electronic lieb lattice. *Nature Physics*, 13:672 EP –, Apr 2017.

[218] C. E. Whittaker, E. Cancellieri, P. M. Walker, D. R. Gulevich, H. Schomerus, D. Vaitiekus, B. Royall, D. M. Whittaker, E. Clarke, I. V. Iorsh, I. A. Shelykh, M. S. Skolnick, and D. N. Krizhanovskii. Exciton polaritons in a two-dimensional lieb lattice with spin-orbit coupling. *Phys. Rev. Lett.*, 120:097401, Mar 2018.

[219] Luis Morales-Inostroza and Rodrigo A. Vicencio. Simple method to construct flat-band lattices. *Phys. Rev. A*, 94:043831, Oct 2016.

[220] D. R. Gulevich, D. Yudin, D. V. Skryabin, I. V. Iorsh, and I. A. Shelykh. Exploring nonlinear topological states of matter with exciton-polaritons: Edge solitons in kagome lattice. *Scientific Reports*, 7(1):1780, 2017.

[221] Dmitry Solnyshkov, Anton Nalitov, Berihu Teklu, Louis Franck, and Guillaume Malpuech. Spin-dependent klein tunneling in polariton graphene with photonic spin-orbit interaction. *Phys. Rev. B*, 93:085404, Feb 2016.

[222] E. A. Cerda-Méndez, D. Sarkar, D. N. Krizhanovskii, S. S. Gavrilov, K. Biermann, M. S. Skolnick, and P. V. Santos. Exciton-polariton gap solitons in two-dimensional lattices. *Phys. Rev. Lett.*, 111:146401, Oct 2013.

[223] Sebastian D. Huber and Ehud Altman. Bose condensation in flat bands. *Phys. Rev. B*, 82:184502, Nov 2010.

[224] S. R. K. Rodriguez, W. Casteels, F. Storme, N. Carlon Zambon, I. Sagnes, L. Le Gratiet, E. Galopin, A. Lemaître, A. Amo, C. Ciuti, and J. Bloch. Probing a dissipative phase transition via dynamical optical hysteresis. *Phys. Rev. Lett.*, 118:247402, Jun 2017.

[225] N. Takemura, S. Trebaol, M. Wouters, M. T. Portella-Oberli, and B. Deveaud. Polaritonic feshbach resonance. *Nature Physics*, 10:500 EP –, Jun 2014.

[226] Riccardo Rota, Wim Casteels, and Cristiano Ciuti. On the robustness of strongly correlated multi-photon states in frustrated driven-dissipative cavity lattices. *The European Physical Journal Special Topics*, 226(12):2805–2814, Jul 2017.

[227] Yaroslav V. Kartashov and Dmitry V. Skryabin. Bistable topological insulator with exciton-polaritons. *Phys. Rev. Lett.*, 119:253904, Dec 2017.

[228] A. H. Castro Neto, F. Guinea, N. M. R. Peres, K. S. Novoselov, and A. K. Geim. The electronic properties of graphene. *Rev. Mod. Phys.*, 81:109–162, Jan 2009.

[229] Grazia Salerno, Tomoki Ozawa, Hannah M. Price, and Iacopo Carusotto. Propagating edge states in strained honeycomb lattices. *Phys. Rev. B*, 95:245418, Jun 2017.

[230] Grazia Salerno, Tomoki Ozawa, Hannah M Price, and Iacopo Carusotto. How to directly observe landau levels in driven-dissipative strained honeycomb lattices. *2D Materials*, 2(3):034015, 2015.

[231] Mikael C. Rechtsman, Julia M. Zeuner, Andreas Tünnermann, Stefan Nolte, Mordechai Segev, and Alexander Szameit. Strain-induced pseudomagnetic field and photonic landau levels in dielectric structures. *Nature Photonics*, 7:153 EP –, Dec 2012. Article.

[232] O. Bleu, D. D. Solnyshkov, and G. Malpuech. Interacting quantum fluid in a polariton chern insulator. *Phys. Rev. B*, 93:085438, Feb 2016.

[233] Chunyan Li, Fangwei Ye, Xianfeng Chen, Yaroslav V. Kartashov, Albert Ferrando, Lluis Torner, and Dmitry V. Skryabin. Lieb polariton topological insulators. *Phys. Rev. B*, 97:081103, Feb 2018.

[234] Sergey V. Suchkov, Andrey A. Sukhorukov, Jiahao Huang, Sergey V. Dmitriev, Chaohong Lee, and Yuri S. Kivshar. Nonlinear switching and solitons in pt-symmetric photonic systems. *Laser & Photonics Reviews*, 10(2):177–213.

[235] Benjamin Besga, Cyril Vaneph, Jakob Reichel, Jérôme Estève, Andreas Reinhard, Javier Miguel-Sánchez, Ata ç Imamoğlu, and Thomas Volz. Polariton boxes in a tunable fiber cavity. *Phys. Rev. Applied*, 3:014008, Jan 2015.

[236] Alberto Biella, Florent Storme, José Lebreuilly, Davide Rossini, Rosario Fazio, Iacopo Carusotto, and Cristiano Ciuti. Phase diagram of incoherently driven strongly correlated photonic lattices. *Phys. Rev. A*, 96:023839, Aug 2017.

[237] Congjun Wu, Doron Bergman, Leon Balents, and S. Das Sarma. Flat bands and wigner crystallization in the honeycomb optical lattice. *Phys. Rev. Lett.*, 99:070401, Aug 2007.

Appendix A

Further sample details

A.1 Layer structure of samples used

In this section, details of the layer structures of the microcavities are provided. In the tables, cells shaded in blue represent layers in the distributed Bragg reflectors and cells shaded in red correspond to the QW layers. The green-shaded cells (combined with the QW layers) then form the cavity layer.

A.1.1 Sample 1

Repeats	Thickness (nm)	Material
23	60.6	GaAs
23	71.0	$Al_{0.85}Ga_{0.15}As$
1	69.6	GaAs
3	10.0	GaAs
3	10.0	$In_{0.04}Ga_{0.96}As$
1	79.6	GaAs
27	71.0	$Al_{0.85}Ga_{0.15}As$
27	60.6	GaAs

A.1.2 Sample 2

Repeats	Thickness (nm)	Material
23	60.94	GaAs
23	71.38	$Al_{0.85}Ga_{0.15}As$
1	3.8	GaAs
3	76.9	GaAs
3	10.0	GaAs
3	10.0	$In_{0.04}Ga_{0.96}As$
3	10.0	GaAs
3	10.0	$In_{0.04}Ga_{0.96}As$
1	90.69	GaAs
27	71.38	$Al_{0.85}Ga_{0.15}As$
27	60.94	GaAs

A.1.3 Sample 3

Repeats	Thickness (nm)	Material
23	60.94	GaAs
23	71.38	$Al_{0.85}Ga_{0.15}As$
1	70.1	GaAs
3	10.0	GaAs
3	10.0	$In_{0.04}Ga_{0.96}As$
1	80.1	GaAs
27	71.38	$Al_{0.85}Ga_{0.15}As$
27	60.94	GaAs

A.2 TE-TM splitting

The TE-TM splitting in microcavities can be controlled by engineering an offset between the cavity Fabry-Pérot frequency and the central frequency of the stopband (SB) of the Bragg mirrors, as treated theoretically in Ref. [72]. In order to demonstrate this using parameters relevant to the samples used here, Fig. A.1 shows an example of the calculated TE-TM splitting against k vector for a heterostructure with a cavity mode wavelength of 851 nm (similar to Sample 2), for three different SB centre wavelengths. The enhanced TE-TM splitting as a function of offset between cavity mode and SB centre can clearly be seen.

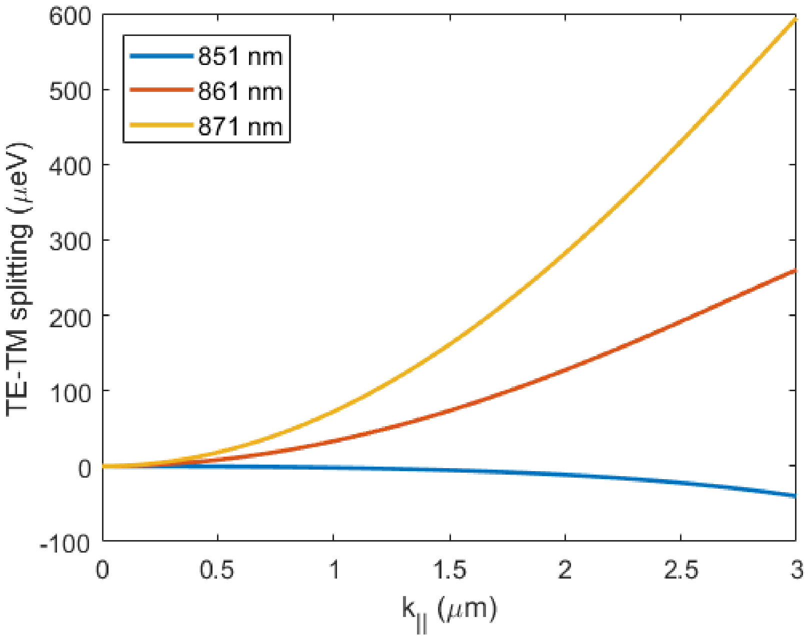

Fig. A.1 Theoretical TE-TM splitting against in-plane wave vector. The simulations use the transfer matrix method and were provided by Dr Paul Walker.

Appendix B

Lieb lattice tight-binding model

In order to explain the band structure and the polarization pattern observed in the Lieb lattice the following tight-binding (TB) model was developed, for both the s and p bands, with polarization-dependent hopping amplitudes. Only nearest-neighbor terms are considered, since the contribution from higher order terms is negligible [109]. As the p bands are formed from coupling of the first excited pillar mode, which is a four-fold degenerate orbital (doubly-degenerate due to the dipole structure and doubly-degenerate due to the polarization), orientation-dependent hopping probabilities are also included, such that the coupling depends on whether the lobes are oriented longitudinally or transversely to the tunnelling direction [237]. Once the kernel matrices for the two TB models are found, it is possible to calculate the polarization-resolved mode occupation on each pillar, and calculate the corresponding linear polarization degree.

B.0.1 s bands

By defining $a_{H,m,n}$ and $a_{V,m,n}$ as the annihilation operators in the s orbital modes of the A sublattice pillars with linear polarization along the horizontal and vertical directions respectively (and similarly for the B and C sites), the Hamiltonian for the s band can be written as:

$$\begin{aligned} H^{s}_{Lieb} &= -\sum_{m,n=-\infty}^{\infty} b^{\dagger}_{H,m,n}[\tau_{\perp}(a_{H,m,n}+a_{H,m-1,n})+\tau_{\parallel}(c_{H,m,n}+c_{H,m,n-1})]+ \\ &\qquad b^{\dagger}_{V,m,n}[\tau_{\parallel}(a_{V,m,n}+a_{V,m-1,n})+\tau_{\perp}(c_{V,m,n}+c_{V,m,n-1})]+h.c., \end{aligned}$$

where the hopping probabilities are $\tau_{\parallel}$, $\tau_{\perp}$ when the polarization is aligned along (parallel) or sideways to (perpendicular) the hopping direction. The on-site s orbital energies are all equal and set to zero. Introducing the Fourier transform of the creation and annihilation operators as:

$$a_{H,p,q} = \frac{1}{N}\sum_{m,n=-\infty}^{\infty} a_{H,m,n}e^{+i\alpha(k_p m+k_q n)}, \qquad a^{\dagger}_{H,p,q} = \frac{1}{N}\sum_{m,n=-\infty}^{\infty} a^{\dagger}_{H,m,n}e^{-i\alpha(k_p m+k_q n)},$$

where α is the unit cell size of the TB model, and k_p and k_q are the x and y component of the wave-vector, respectively. Similarly it is possible to define the Fourier transform of the operators for the B and C sites and for the V polarization, it is possible to write the above Hamiltonian in k-space. This can be written in a compact form as:

$$H^s_{Lieb} = -2 \sum_{p,q=-\infty}^{\infty} \psi^{\dagger T}_{p,q} \begin{pmatrix} M^s_{H,p,q} & 0 \\ 0 & M^s_{V,p,q} \end{pmatrix} \psi_{p,q},$$

with

$$\psi^{\dagger T}_{p,q} = (a^\dagger_{H,p,q}, b^\dagger_{H,p,q}, c^\dagger_{H,p,q}, a^\dagger_{V,p,q}, b^\dagger_{V,p,q}, c^\dagger_{V,p,q})$$

and

$$M^s_{H,p,q} = \begin{pmatrix} 0 & \tau_\perp e^{+\frac{i\alpha k_q}{2}} \cos\left(\frac{k_q\alpha}{2}\right) & 0 \\ \tau^\star_\perp e^{-\frac{i\alpha k_q}{2}} \cos\left(\frac{k_q\alpha}{2}\right) & 0 & \tau_\parallel e^{+\frac{i\alpha k_p}{2}} \cos\left(\frac{k_p\alpha}{2}\right) \\ 0 & \tau^\star_\parallel e^{-\frac{i\alpha k_p}{2}} \cos\left(\frac{k_p\alpha}{2}\right) & 0 \end{pmatrix},$$

and

$$M^s_{V,p,q} = \begin{pmatrix} 0 & \tau_\parallel e^{+\frac{i\alpha k_q}{2}} \cos\left(\frac{k_q\alpha}{2}\right) & 0 \\ \tau^\star_\parallel e^{-\frac{i\alpha k_q}{2}} \cos\left(\frac{k_q\alpha}{2}\right) & 0 & \tau_\perp e^{+\frac{i\alpha k_p}{2}} \cos\left(\frac{k_p\alpha}{2}\right) \\ 0 & \tau^\star_\perp e^{-\frac{i\alpha k_p}{2}} \cos\left(\frac{k_p\alpha}{2}\right) & 0 \end{pmatrix}.$$

The polarized eigenvector of the s band can be easily written in terms of the function $E[x,y] = -2xe^{-\frac{i\alpha y}{2}} cos\left(\frac{y\alpha}{2}\right)$, where x is the hopping probability and y the direction of propagation:

$$
\begin{aligned}
e_1 &= \frac{1}{A_1}\left\{0, -\frac{E[\tau_\perp, k_q]}{E[\tau_\parallel, k_p]}, 1, 0, 0, 0\right\} \\
e_2 &= \frac{1}{A_2}\left\{-\frac{\sqrt{|E[\tau_\parallel, k_p]|^2 + |E[\tau_\perp, k_q]|^2}}{E[\tau_\perp, k_q]^*}, \frac{E[\tau_\parallel, k_p]^*}{E[\tau_\perp, k_q]^*}, 1, 0, 0, 0\right\} \\
e_3 &= \frac{1}{A_3}\left\{+\frac{\sqrt{|E[\tau_\parallel, k_p]|^2 + |E[\tau_\perp, k_q]|^2}}{E[\tau_\perp, k_q]^*}, \frac{E[\tau_\parallel, k_p]^*}{E[\tau_\perp, k_q]^*}, 1, 0, 0, 0\right\} \\
e_4 &= \frac{1}{A_4}\left\{0, 0, 0, 0, -\frac{E[\tau_\parallel, k_q]}{E[\tau_\perp, k_p]}, 1\right\} \\
e_5 &= \frac{1}{A_5}\left\{0, 0, 0, -\frac{\sqrt{|E[\tau_\parallel, k_q]|^2 + |E[\tau_\perp, k_p]|^2}}{E[\tau_\parallel, k_q]^*}, \frac{E[\tau_\perp, k_p]^*}{E[\tau_\parallel, k_q]^*}, 1\right\} \\
e_6 &= \frac{1}{A_6}\left\{0, 0, 0, +\frac{\sqrt{|E[\tau_\parallel, k_q]|^2 + |E[\tau_\perp, k_p]|^2}}{E[\tau_\parallel, k_q]^*}, \frac{E[\tau_\perp, k_p]^*}{E[\tau_\parallel, k_q]^*}, 1\right\},
\end{aligned}
$$

where the six constants A_i are normalization constants. We see here that with these assumptions the H and V polarized modes are completely independent since the kernel matrix is a block matrix. Each block is basically the 3×3 kernel matrix for a single mode Lieb lattice. The main difference here is that the hopping probabilities change depending on the polarization and on the hopping direction.

First considering the unpolarized case (i.e. $\tau_\perp = \tau_\parallel = \tau$) and fitting the s part of the experimental band structure a value of $\tau = 0.165$ meV is estimated. Next, the degeneracy between the two tunnelling terms is lifted so that $\tau_\parallel = 0.165$ meV and $\tau_\perp = 0.145$ meV. With these new values the calculated degree of polarization (S_1) of the flat-band eigenmodes is ± 0.128, in excellent agreement with the experimental value of ± 0.13. To obtain this value the eigenvectors of H^s_{Lieb} are evaluated at each k

point, giving the distribution of the H and V populations on the three pillars forming the unit cell. This allows the evaluation, for each k point, of the relative H and V population. As a final step, the weighted averages of the H and V populations over the entire k-space are calculated for each pillar, giving the polarization on each pillar.

B.0.2 p bands

Similarly to the treatment of the s bands a_{Hx}, a_{Hy}, a_{Vx}, and a_{Vy} are the annihilation operators for the p orbital modes of the pillar with H and V polarization and with the lobes aligned along the x or y directions. The notation follows the same convention for the creation operators and for the modes on the B and C sites. With these definitions, the Hamiltonian for the p band in real space can be written as:

$$\begin{aligned}
H^{p}_{Lieb} \;=\; & -\sum_{m,n=-\infty}^{\infty} b^{\dagger}_{Hx_{m,n}}[\tau^{t}_{\perp}(a_{Hx_{m,n}} + a_{Hx_{m-1,n}}) - \tau^{a}_{\parallel}(c_{Hx_{m,n}} + c_{Hx_{m,n-1}})] \\
& -\sum_{m,n=-\infty}^{\infty} b^{\dagger}_{Hy_{m,n}}[\tau^{a}_{\perp}(a_{Hy_{m,n}} + a_{Hy_{m-1,n}}) - \tau^{t}_{\parallel}(c_{Hy_{m,n}} + c_{Hy_{m,n-1}})] \\
& -\sum_{m,n=-\infty}^{\infty} b^{\dagger}_{Vx_{m,n}}[\tau^{t}_{\parallel}(a_{Vx_{m,n}} + a_{Vx_{m-1,n}}) - \tau^{a}_{\perp}(c_{Vx_{m,n}} + c_{Vx_{m,n-1}})] \\
& -\sum_{m,n=-\infty}^{\infty} b^{\dagger}_{Vy_{m,n}}[\tau^{a}_{\parallel}(a_{Vy_{m,n}} + a_{Vy_{m-1,n}}) - \tau^{t}_{\perp}(c_{Vy_{m,n}} + c_{Vy_{m,n-1}})] + h.c.,
\end{aligned}$$

where the hopping probabilities $\tau^{a}_{\parallel}$, $\tau^{t}_{\parallel}$, $\tau^{a}_{\perp}$, and $\tau^{t}_{\perp}$ correspond to modes hopping from one site to another having the polarization parallel ($\parallel$) or perpendicular ($\perp$) to the hopping direction and the lobes of the p orbital aligned (a) or transverse (t) to the hopping direction. As before one can introduce the Fourier transform of the creation and annihilation operators and diagonalize the Hamiltonian in k-space. This time the kernel matrix will be 12×12 since there are 2 modes with 2 possible polarizations on each of the 3 pillars. In this case the Hamiltonian can be written in a compact form as:

$$H^{p}_{Lieb} = -2 \sum_{p,q=-\infty}^{\infty} \psi^{p\dagger^{T}}_{p,q} \begin{pmatrix} M^{p}_{Hx,p,q} & 0 & 0 & 0 \\ 0 & M^{p}_{Hy,p,q} & 0 & 0 \\ 0 & 0 & M^{p}_{Vx,p,q} & 0 \\ 0 & 0 & 0 & M^{p}_{Vy,p,q} \end{pmatrix} \psi^{p}_{p,q} \ ,$$

with

$$\psi^{p\dagger^{T}}_{p,q} = (a^{\dagger}_{Hx,p,q}, a^{\dagger}_{Hy,p,q}, b^{\dagger}_{Hx,p,q}, b^{\dagger}_{Hy,p,q}, c^{\dagger}_{Hx,p,q}, c^{\dagger}_{Hy,p,q}, a^{\dagger}_{Vx,p,q}, a^{\dagger}_{Vy,p,q}, b^{\dagger}_{Vx,p,q}, b^{\dagger}_{Vy,p,q}, c^{\dagger}_{Vx,p,q}, c^{\dagger}_{Vy,p,q}),$$

and

$$M^{p}_{Hx,p,q} = \begin{pmatrix} 0 & \tau^{t}_{\perp} e^{+\frac{i\alpha k_q}{2}} \cos\left(\frac{k_q \alpha}{2}\right) & 0 \\ \tau^{t\star}_{\perp} e^{-\frac{i\alpha k_q}{2}} \cos\left(\frac{k_q \alpha}{2}\right) & 0 & \tau^{a}_{\parallel} e^{+\frac{i\alpha k_p}{2}} \cos\left(\frac{k_p \alpha}{2}\right) \\ 0 & \tau^{a\star}_{\parallel} e^{-\frac{i\alpha k_p}{2}} \cos\left(\frac{k_p \alpha}{2}\right) & 0 \end{pmatrix},$$

$$M^{p}_{Hy,p,q} = \begin{pmatrix} 0 & \tau^{a}_{\perp} e^{+\frac{i\alpha k_q}{2}} \cos\left(\frac{k_q\alpha}{2}\right) & 0 \\ \tau^{a\star}_{\perp} e^{-\frac{i\alpha k_q}{2}} \cos\left(\frac{k_q\alpha}{2}\right) & 0 & \tau^{t}_{\parallel} e^{+\frac{i\alpha k_p}{2}} \cos\left(\frac{k_p\alpha}{2}\right) \\ 0 & \tau^{t\star}_{\parallel} e^{-\frac{i\alpha k_p}{2}} \cos\left(\frac{k_p\alpha}{2}\right) & 0 \end{pmatrix},$$

$$M^{p}_{Vx,p,q} = \begin{pmatrix} 0 & \tau^{t}_{\parallel} e^{+\frac{i\alpha k_q}{2}} \cos\left(\frac{k_q\alpha}{2}\right) & 0 \\ \tau^{t\star}_{\parallel} e^{-\frac{i\alpha k_q}{2}} \cos\left(\frac{k_q\alpha}{2}\right) & 0 & \tau^{a}_{\perp} e^{+\frac{i\alpha k_p}{2}} \cos\left(\frac{k_p\alpha}{2}\right) \\ 0 & \tau^{a\star}_{\perp} e^{-\frac{i\alpha k_p}{2}} \cos\left(\frac{k_p\alpha}{2}\right) & 0 \end{pmatrix},$$

$$M^{p}_{Vx,p,q} = \begin{pmatrix} 0 & \tau^{a}_{\parallel} e^{+\frac{i\alpha k_q}{2}} \cos\left(\frac{k_q\alpha}{2}\right) & 0 \\ \tau^{a\star}_{\parallel} e^{-\frac{i\alpha k_q}{2}} \cos\left(\frac{k_q\alpha}{2}\right) & 0 & \tau^{t}_{\perp} e^{+\frac{i\alpha k_p}{2}} \cos\left(\frac{k_p\alpha}{2}\right) \\ 0 & \tau^{t\star}_{\perp} e^{-\frac{i\alpha k_p}{2}} \cos\left(\frac{k_p\alpha}{2}\right) & 0 \end{pmatrix}.$$

As before, the polarized eigenvectors of the p band can be easily written in terms of the function $E[x,y] = -2xe^{-\frac{i\alpha y}{2}} cos\left(\frac{y\alpha}{2}\right)$, where x is the hopping probability and y the direction of propagation:

$$
\begin{aligned}
e_1 &= \frac{1}{A_1}\left\{0, -\frac{E[\tau^t_\perp, k_q]}{E[\tau^a_\parallel, k_p]}, 1, 0, 0, 0, 0, 0, 0, 0, 0, 0\right\} \\
e_2 &= \frac{1}{A_2}\left\{-\frac{\sqrt{|E[\tau^a_\parallel, k_p]|^2 + |E[\tau^t_\perp, k_q]|^2}}{E[\tau^t_\perp, k_q]^*}, \frac{E[\tau^a_\parallel, k_p]^*}{E[\tau^t_\perp, k_q]^*}, 1, 0, 0, 0, 0, 0, 0, 0, 0, 0\right\} \\
e_3 &= \frac{1}{A_3}\left\{+\frac{\sqrt{|E[\tau^a_\parallel, k_p]|^2 + |E[\tau^t_\perp, k_q]|^2}}{E[\tau^t_\perp, k_q]^*}, \frac{E[\tau^a_\parallel, k_p]^*}{E[\tau^t_\perp, k_q]^*}, 1, 0, 0, 0, 0, 0, 0, 0, 0, 0\right\} \\
e_4 &= \frac{1}{A_4}\left\{0, 0, 0, 0, -\frac{E[\tau^a_\perp, k_q]}{E[\tau^t_\parallel, k_p]}, 1, 0, 0, 0, 0, 0, 0\right\} \\
e_5 &= \frac{1}{A_5}\left\{0, 0, 0, -\frac{\sqrt{|E[\tau^t_\parallel, k_p]|^2 + |E[\tau^a_\perp, k_q]|^2}}{E[\tau^a_\perp, k_q]^*}, \frac{E[\tau^t_\parallel, k_p]^*}{E[\tau^a_\perp, k_q]^*}, 1, 0, 0, 0, 0, 0, 0\right\} \\
e_6 &= \frac{1}{A_6}\left\{0, 0, 0, +\frac{\sqrt{|E[\tau^t_\parallel, k_p]|^2 + |E[\tau^a_\perp, k_q]|^2}}{E[\tau^a_\perp, k_q]^*}, \frac{E[\tau^t_\parallel, k_p]^*}{E[\tau^a_\perp, k_q]^*}, 1, 0, 0, 0, 0, 0, 0\right\} \\
e_7 &= \frac{1}{A_7}\left\{0, 0, 0, 0, 0, 0, 0, -\frac{E[\tau^t_\parallel, k_q]}{E[\tau^a_\perp, k_p]}, 1, 0, 0, 0\right\} \\
e_8 &= \frac{1}{A_8}\left\{0, 0, 0, 0, 0, 0, -\frac{\sqrt{|E[\tau^t_\parallel, k_q]|^2 + |E[\tau^a_\perp, k_p]|^2}}{E[\tau^t_\parallel, k_q]^*}, \frac{E[\tau^a_\perp, k_p]^*}{E[\tau^t_\parallel, k_q]^*}, 1, 0, 0, 0\right\} \\
e_9 &= \frac{1}{A_9}\left\{0, 0, 0, 0, 0, 0, +\frac{\sqrt{|E[\tau^t_\parallel, k_q]|^2 + |E[\tau^a_\perp, k_p]|^2}}{E[\tau^t_\parallel, k_q]^*}, \frac{E[\tau^a_\perp, k_p]^*}{E[\tau^t_\parallel, k_q]^*}, 1, 0, 0, 0\right\} \\
e_{10} &= \frac{1}{A_{10}}\left\{0, 0, 0, 0, 0, 0, 0, 0, 0, 0, -\frac{E[\tau^a_\parallel, k_q]}{E[\tau^t_\perp, k_p]}, 1\right\} \\
e_{11} &= \frac{1}{A_{11}}\left\{0, 0, 0, 0, 0, 0, 0, 0, 0, -\frac{\sqrt{|E[\tau^a_\parallel, k_q]|^2 + |E[\tau^t_\perp, k_p]|^2}}{E[\tau^a_\parallel, k_q]^*}, \frac{E[\tau^t_\perp, k_p]^*}{E[\tau^a_\parallel, k_q]^*}, 1\right\} \\
e_{12} &= \frac{1}{A_{12}}\left\{0, 0, 0, 0, 0, 0, 0, 0, 0, +\frac{\sqrt{|E[\tau^a_\parallel, k_q]|^2 + |E[\tau^t_\perp, k_p]|^2}}{E[\tau^a_\parallel, k_q]^*}, \frac{E[\tau^t_\perp, k_p]^*}{E[\tau^a_\parallel, k_q]^*}, 1\right\}
\end{aligned}
$$

where the twelve constants A_i are normalization constants. As for the s band, first the unpolarized case is considered (i.e. $\tau^a_\parallel = \tau^a_\perp = \tau^a$ and $\tau^t_\parallel = \tau^t_\perp = \tau^t$) and values of $\tau^a = 0.375$ meV and $\tau^t = 0.100$ meV are estimated from experimental data. Next the polarization dependence is introduced: $\tau_{\parallel}^{a} = 0.375$, $\tau_{\perp}^{a} = 0.125$, $\tau_{\parallel}^{t} = 0.100$ and $\tau_{\perp}^{t} = 0.033$ meV. With these values the calculated degree of polarization (S_1) and the ratio between p_x and p_y orbitals of the p flat-band eigenmodes are ± 0.4 and 3.7 (the inverse applies to C sites) respectively, in good agreement with the experimental results. To obtain these values the same procedure used for H_{Lieb}^{s} was employed.